University of Alberta

Magnetic Resonance Imaging based Radiotherapy Treatment Planning: problems, solutions, and applications

by

Lesley Nicole Baldwin

A thesis submitted to the Faculty of Graduate Studies and Research
in partial fulfillment of the requirements for the degree of

Doctor of Philosophy
in
Medical Physics

Department of Physics

Fall 2010
Edmonton, Alberta

Examining Committee

Dr. B. Gino Fallone, Oncology

Dr. Ron Sloboda, Oncology

Dr. Satyapal Rathee, Oncology

Dr. Don Robinson, Oncology

Dr. Alan Wilman, Biomedical Engineering

Dr. Randall Ten Haken, Radiation Oncology, University of Michigan

Abstract

Despite their unmatched soft-tissue contrast, Magnetic Resonance (MR) images suffer from wide-ranging image distortions; this has raised questions about their suitability as an imaging modality upon which to base conformal radiation therapy treatment plans. This thesis addresses image distortion as it relates to the implementation of MR-based radiation therapy treatment planning (MR-RTP). A grid phantom was imaged at 3T to determine the 3D distortion field using in-house software. Using multiple images, both machine- and object-related sources of distortion were separated such that individual evaluation of distortion sources is possible. Over the imaging volume, nonlinearities in the gradients led to peak-to-peak image distortions of up to 11 mm. For in-vivo distortion quantification, the method was augmented with a modified gradient echo sequence which measures the phase evolution due to underlying field inhomogeneities. The amount of distortion measured using this technique is dependent upon both patient anatomy and sequence parameters, but was found to contribute 5.7 mm at maximum. The methods presented can be combined to provide comprehensive distortion rectification such that mean residual image distortion is reduced to well below the pixel resolution. Finally, distortion quantification and correction methods were applied to a clinical MR-RTP study of prostate patients. The dosimetric consequences of distortion correction were investigated by comparing 3D conformal and intensity modulated radiation therapy plans developed based on both uncorrected and corrected MRI data sets. Total image distortions and those directly affecting the prostate and organs at risk (OARs) were assessed and target doses, OAR doses, and dose volume histograms were compared. Maximum distortion (from all sources) was 7.8 mm. With the exception of two patients, changes in plan dosimetry were insignificant (<2% / <1Gy). Two patients who were poorly position suffered larger distortions in the target region which led to dosimetric differences of up to 4.2%.

Acknowledgements

It gives me great pleasure to think of the vast and intricate tangle of people who have helped me to arrive at this point. One accomplishes very little on one's own and I am so grateful for the many mentors, colleagues, friends and family who have all made this work possible.

A debt is certainly owed to my knowledgeable supervisors Drs. Keith Wachowicz and Gino Fallone. Keith always had time to both listen and help and saw me through from the very genesis of this work (a one line idea) to its very completion. Dr. Fallone provided the one line idea and helped me to obtain not only the much appreciated financial resources but also all the material resources required along the way. Thank-you both. My supervisory committee – Drs. Rathee, Sloboda and Robinson, and my examining committee – Drs. Wilman, Marchand, and Ten Haken, have also provided insight, suggestions, and encouragement throughout the years. Thank-you also to Sherry Connors who has been an invaluable mentor and resource in the last year of my studies – your support in navigating the post-graduate working world has meant so much.

I have had the great pleasure of undertaking my graduate studies in the company of wonderful colleagues whom I'm now so happy to call friends. Thank-you to: Thalat who sets the bar in so many ways and who both shares and listens to the important things; Atiyah who is wise and principled and all other good things; Donata, whose story makes me so proud; Steven, the ideas man, who can always make me laugh; Amr who broadened my musical taste; Alasdair, who is a good person to look up – and not just because he is tall; Jay who, thankfully, reminds me that I have learned something after all; Artur who brings chocolate and navigates all my IT needs; Yingli whose quiet earnestness reminds me of the understory; Sandra who keeps us all young; and Dave, who, by calling me a kindred spirit, gave me one of the best compliments of all.

I have to thank not only my colleagues in Medical Physics but also my friends beyond the department who, together, have provided me with the richest social network I have ever known. I owe you in ways I don't yet know; you humble me and you inspire me. You kept me sane through the most difficult task I've ever accomplished. Thank-you to: Claire who lets me natter on about nothing and makes me laugh at myself through anything; Emily, my favourite hidden gem; Becky, the finest juggler of academics, sports, and service who brought me into the triathlon club (best ever!); Jessie who, above all, remains calm; Eric and Julia who will always host the best parties; Simon who is inquisitive in every possible way; James and Suz who introduced me to cross-country skiing and who validated my love of KFC; Rob, a great chearer-upper (remember when, while wearing pink shoes and a skirt, I built a roof with you?); Aisling, my first real

friend in Edmonton; Josh, Pat, Dave and Bridget, Stefan and Sanja: you helped me do things I didn't know were possible. You are strong and determined and you make me want to be the same. Most of all, you are ridiculous amounts of fun; Gavin and Nickie, Suz and Trav, Rahul and Erin, Robin and Erin, and Sarah, who make winter something to look forward to; Charmaine and Sim, Jules, Mike, Andy, Rita, Meg, Ali, Julia, Carlotta - how I wish I could have you all here with me. Your phone calls, your letters, your postcards, your visits: I savour them all and always look forward to the next ones; and, of course, Travis, who listens, makes me laugh in the morning, and bakes a loaf of brioche like it's no big deal. You saw me through the worst and now I hope to show you the best.

To Edmonton who won me over with its snow, its river valley, but most of all, with its people. Andy said it would be so and he spoke the truth.

Finally, thank-you to my family. To Lauren who is capable of endless generosity, to Christina, who really means it when she asks how you're doing, and to my parents who would have let me choose any career I wanted and would have been proud of me nonetheless.

To all those I've listed and for all those I might have missed - better people I cannot imagine. I am so lucky to have you and I will keep you with me always.

Table of Contents

List of Tables

List of Figures

List of Abbreviations

1D	One dimensional
2D	Two dimensional
3D	Three dimensional
ART	Adaptive radiotherapy
BFFE	Balanced fast field echo
BW	Bandwidth
CCI	Cross Cancer Institute
CNS	Central nervous system
CRT	Conformal radiotherapy
CS	Chemical shift
CT	Computed Tomography
CTV	Clinical target volume
DRR	Digitally reconstructed radiograph
DVH	Dose volume histogram
EPI	Echo planar imaging
EPID	Electronic portal imaging device
FE	Frequency encoding
FID	Free induction decay
FLASH	Fast low angle shot
FOV	Field of view
FT	Fourier transform
GE	Gradient echo

GTV	Gross tumour volume
HU	Hounsfield units
ICRU	International Commission on Radiation Units and Measurements
IGRT	Image guided radiation therapy
IMRT	Intensity modulated radiation therapy
kVCT	Kilovoltage computed tomography
LTO	Linearity test object
MLC	Multi-leaf collimator
MR	Magnetic resonance
MRI	Magnetic resonance imaging
MRS	Magnetic resonance spectroscopy
MRSI	Magnetic resonance spectroscopic imaging
MVCT	Megavoltage computed tomography
NMR	Nuclear magnetic resonance
NTCP	Normal tissue complication probability
OAR	Organ at risk
PE	Phase encoding
PET	Positron emission tomography
PTV	Planning target volume
RF	Radiofrequency
RTP	Radiotherapy treatment planning
SE	Spin echo
SPECT	Single photon emission computed tomography

SNR	Signal to noise ratio
TCP	Tumour control probability
TE	Echo time
TR	Repetition time
US	Ultrasound

List of Symbols

A	Area
B	Magnetic field or, more generally, magnetic flux density
B_0	Main polarizing magnetic field
B_1, $B_1(t)$	Rotating radiofrequency magnetic field
c_x, c_y	Centroid coordinates along the x and y axes
D	Absorbed dose
D_{50}, D_{30}, D_{20}	Dose received by 50% / 30% / 20% of the structure volume
E	Energy
f	Frequency
dG_x, dG_y, dG_z	Gradient non-linearities along the x, y, and z axes
G_{FE}	Magnetic field gradient strength, frequency encoding direction
$\widetilde{G}_{PE}$	Effective field gradient strength, phase encode direction
G_x, G_y, G_z	Magnetic field gradients along the x, y, and z axes
G'_x, G'_y, G'_z	Non-linear magnetic field gradients along the x, y, and z axes
${}^1H$	Hydrogen nuclei
H	Applied magnetic field strength
i	Image intensity
J	Jacobian
k	Maxwell-Boltzman constant
k	Generalized frequency space coordinate
M, M_0	Total magnetization

M_O	Overlap mask
M_F	Fat mask
M_{xy}	Transverse magnetization
M_z	Longitudinal magnetization
$n\uparrow, n\downarrow$	Number of spins the "spin-up" and "spin-down" states
N_x	Image matrix size in the *x* direction
N_y	Image matrix size in the *y* direction
N_z	Number of image slices
p	Pixels
S	Signal
t	Time
T	Temperature
$\vec{T}$	Torque
T_1	Longitudinal (spin-lattice) relaxation time constant
T_2	Transverse (spin-spin) relaxation time constant (non-reversible)
T'_2	Transverse relaxation time constant (reversible)
T_2^*	Total transverse relaxation time (reversible and non-reversible)
V_{95}	Volume percentage receiving 95% of the prescription dose
$\hat{x}, \hat{y}, \hat{z}$	Unit vectors along *x, y*, and *z* axes
$\hat{x}_\rho, \hat{y}_\rho, \hat{z}_\rho$	Unit vectors along the main axes in the rotating frame
x, y, z	Cartesian coordinates
x', y', z'	Distorted coordinates
Z	Atomic number

α	Tip angle
χ	Magnetic susceptibility
ΔB	Total magnetic field inhomogeneities
ΔB_0	Inhomogeneities in the main magnetic field
ΔB_{CS}	Inhomogeneities due to chemical shift
ΔB_{χ}	Inhomogeneities due to susceptibility differences
ΔG	Phase encode gradient increment
Δx, Δy, Δz	Distortion values along the *x, y*, and *z* axes
σ	Chemical shift
Δt	Sampling Interval
γ	Gyromagnetic ratio
φ	Phase
μ	Linear attenuation coefficient
μ	Nuclear magnetic moment
ρ	Spin density
τ	Phase encode gradient duration
ω	Frequency
ω_0	Larmor frequency
Ψ	Photon energy fluence

1. Chapter 1: Introduction

1.1. Overview of the Thesis

Magnetic Resonance Imaging based Radiotherapy Treatment Planning (MRI-RTP) has evolved naturally both from the increased availability and quality of medical imaging and from an ever-expanding ability to refine radiation delivery procedures. Indeed, modern day cancer therapy relies heavily on a variety of imaging modalities through all stages of diagnosis, planning, delivery and evaluation, and Magnetic Resonance Imaging (MRI) finds itself playing an increasingly important support role to these processes. This thesis seeks to investigate one of the fundamental problems associated with incorporating MRI into the practice of radiotherapy - namely, image distortion. The sources and characteristics of the distortion problem are identified, solutions are introduced, and finally, distortion rectified images are applied to the practice of MRI-RTP.

The structure of the thesis is as follows: Chapter 1 reviews modern radiotherapy techniques and the role of medical imaging at various stages of the radiotherapy process; in doing so, it provides important context for the remainder of the thesis. Chapter 2 introduces the concepts relevant to nuclear magnetic resonance, image formation, and image distortion. The development of the materials and methods for characterising machine-related sources of MR distortion are covered in Chapter 3 and have been published, in somewhat modified form, in *Medical*

Physics.[2] The materials and techniques introduced in Chapter 3 were adapted and extended to evaluate machine related distortions over a larger, more clinically relevant field of view. As well, methods were added to measure and correct for patient-related image distortions. These topics are covered in Chapter 4 and form the basis of a second *Medical Physics* publication.[3] Chapter 5 describes work carried out on phantoms to refine one particular aspect of the distortion correction scheme, namely the residual chemical shift artifact. The contents of Chapter 5 have been published as part of the 2010 ISMRM conference proceedings.[4] Chapter 6 includes the result of a clinical investigation which applied the distortion measurement and correction methods developed in earlier chapters to a prostate radiotherapy treatment planning study. An abbreviated version of Chapter 6 is currently under review with the *International Journal of Radiation Oncology Biology and Physics*. Finally, Chapter 7 is a brief concluding chapter to the thesis.

1.2. External Beam Radiation Therapy

The treatment of cancer is generally achieved through three methods: surgery, chemotherapy and radiation therapy. These treatments may be delivered individually or in combination in order to achieve the optimum result. Radiation therapy is used in approximately half of all treatments[5] and can be delivered using unsealed sources, sealed sources (brachytherapy), or with external beam therapy. External beam radiotherapy is the most widely used delivery method and is the focus of the following sections.

The overarching objective of radiation therapy, including external beam radiotherapy, is to deliver a lethal dose to the tumour volume in order to eradicate the cancerous tissue, while simultaneously limiting the dose to surrounding normal tissues and critical structures in order to prevent unnecessary treatment side effects. In practice, some dose is always delivered to normal structures. For clinical purposes, the gross tumour volume (GTV)[6] is defined as the visible tumour extent. To this volume a margin is added to account for microscopic disease invasion and the resultant region is known as the clinical tumour volume (CTV). It is assumed that no tumour cells exist beyond the CTV. Finally, the planning target volume (PTV) is identified as the CTV plus a suitable margin to account for potential inter- and intra-fraction motion of both the patient and the tumour. These concepts are illustrated in Figure 1-1. The PTV inevitably includes some amount of normal tissue, but it is this volume to which the dose is prescribed and radiation is delivered.[6,7] The treated and irradiated volumes indicate regions receiving the minimum target dose and a "significant" dose (i.e. $\geq$ 50% of the target dose), respectively; these volumes are both dependent on the particular treatment technique.

The therapeutic success of a radiation treatment is governed by the balance between tumour control probability (TCP) and normal tissue complication probability (NTCP). Indeed, much of radiation research is focussed towards improving the TCP-NTCP balance. By decreasing the margins added to the GTV,

the amount of normal tissue - and hence restrictions on the NTCP - can be reduced. Similarly, without the same constraints on the NTCP, the dose to the tumour can, in theory, be elevated and TCP improved. The techniques of modern external beam radiotherapy are discussed in the following sections.

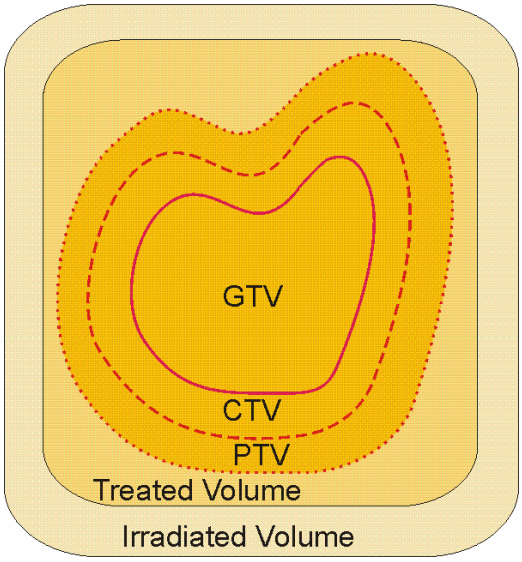

Figure 1-1

A schematic illustration of ICRU volumes. Note: the GTV may appear differently on images from different modalities.

1.2.1. Conformal Radiotherapy

Three dimensional conformal radiotherapy (3D-CRT) refers to treatments that are based on 3D anatomical information and generate dose distributions that tightly

conform to the target volume whilst depositing minimal dose to normal tissue.[8] The major obstacle to achieving this objective is accurate knowledge of the tumour extent. If the GTV cannot be fully discerned - as is often the case - the concept of conformality holds little meaning. Moreover, in terms of optimizing local control, the correct placement of the target volumes becomes more critical than for techniques which use wide beams and simple beam arrangements. As discussed above, margins are added to account for uncertainties in tumour extent, patient motion, etc.

1.2.2. Intensity Modulated Radiotherapy

The primary difference between conventional radiation therapy (including 3D-CRT) and Intensity Modulated Radiotherpy (IMRT) is that IMRT provides an extra degree of freedom - that of intensity modulation - towards achieving dose conformality. Intensity modulation has been widely adopted for clinical use over the last decade and is defined for beams that deliver "more than two intensity levels for a single beam direction and a single position in space".[9] The definition of IMRT does not take into account whether treatments are forward- or inverse-planned, or how the intensity modulation is performed (i.e. multi-leaf collimators (MLCs) vs. compensators; or step-and-shoot vs. dynamic delivery). IMRT is capable of generating concave dose distributions and sharp dose gradients; it is ideally suited to treating head and neck cancers, which can be found in close proximity to many organs at risk (OARs) and to prostate cancer, which requires conformal avoidance of structures such as the rectum and small bowel. In fact,

barring slight radiobiological differences, IMRT can create dose distributions that compete well with the much more costly treatments produced by proton beam therapy.[10]

It must be recognized, however, that the nearly unlimited control of dose shaping provided by techniques such as 3D-CRT and IMRT can be a double-edged sword: an increase in dose conformality brings with it an increase in the risk for target miss. Technical prowess in planning does not necessarily translate to improved clinical outcomes. To ensure the effective use of the tightly sculpted dose distributions offered by techniques such as 3D-CRT and IMRT, high quality 3D images of the irradiated anatomy are required at all stages throughout radiotherapy planning and delivery.

1.3. The role of imaging in radiotherapy

The ability to painlessly and non-invasively visualize the internal structure of the living body transformed the practice of medicine in the 20th century more than any other innovation. Unsurprisingly, medical imaging has revolutionized the practice of radiation therapy into the 21st century and now guides many of the future directions of the field. The inclusion of imaging at all stages of radiation therapy - from planning to delivering to verifying treatments - has been an important factor in improving both the clinical TCP-NTCP balance and patient survival and quality of life. Advances in imaging allow the gross tumour to be more accurately defined, can add valuable information about the margins required for microscopic

disease spread, and can eliminate some of the guess-work inherent in establishing limits of tumour motion. Reducing margins can have drastic effects: for example, a spherical tumour with a 5 cm diameter and an additional 2 cm margin represents an irradiated volume of 382 cm^3. Halving the margins from 2 cm to 1 cm, reduces the irradiated volume to 179 cm^3 - less than half the original volume. Indeed, advances in imaging have led to safer, more effective delivery of radiation therapy, improved local control[11,12] and better quality of life due to a reduction in normal tissue irradiation.[13,14] A variety of imaging modalities are available, including ultrasound (US), positron emission tomography (PET), single photon emission computed tomography (SPECT), computed tomography (CT), and magnetic resonance imaging (MRI). Each modality has unique advantages and limitations with regard to their application in (1) target localisation and treatment planning, (2) patient set-up verification, and (3) dose calculation and treatment adaptation.

1.3.1. Target Localization and Treatment Planning

Target localization is the first of many important steps in the radiotherapy process. As mentioned, highly conformal delivery techniques require accurate and precise determination of the tumour volume. If the tumour extent cannot be clearly identified, no amount of beam shaping, modulation, or dose conformality can produce a superior clinical outcome. Indeed, outcomes can be damaged by shaping the dose to an incorrect volume. Tumour volumes are typically outlined on CT because CT images provide excellent geometric fidelity, can resolve boney anatomy clearly (useful for verifying treatment set-up – see §1.3.2), and provide

electron density information necessary for the dose calculations carried out by computerized treatment planning systems.

Unfortunately, the soft-tissue contrast of CT imaging is limited by the similarity of linear attenuation coefficients in the kilovoltage range for tissues of interest. For this reason, it has become increasingly commonplace to use multimodality imaging (i.e. CT + PET/SPECT/MRI etc.) which can enable more precise delineation of the CTV.[15-18] Imaging modalities such as PET, SPECT and MRS can provide important spatial information about biologically relevant tumour characteristics, e.g. regions of hypoxia, or high cell proliferation or density.[19,20] This information can be combined with CT to reduce uncertainties associated with establishing margins for biological tumour infiltration[18] or can be used to evaluate treatment response and recurrence at later stages in the radiotherapy process. Images are typically fused via rigid or deformable registration of either boney anatomy or user-defined control points.

Because of the primary importance of soft-tissue contrast for accurate localisation, MRI stands out as the preferred imaging modality for a wide range of cancer sites, including prostate, head and neck, central nervous system (CNS) and sarcomas. One area of particular promise for both improved anatomical and biological target definition is combined MRI and magnetic resonance spectroscopy (MRS). MRI provides high contrast soft-tissue images that reflect tumour physiology, while MRS Imaging (MRSI) provides information about metabolic changes that may

precede physiological indicators of disease. The two imaging modalities have been used together to provide complimentary treatment planning information without the need for inter-modality image fusion.[21,22]

Of the aforementioned imaging modalities, CT and MRI represent the principle modalities used in a radiation therapy setting. A very brief discussion of each of the techniques is therefore included in the subsections that follow.

1.3.1.1. Computed Tomography

Computed Tomography images are widely used in the field of radiation oncology for treatment planning, patient positioning and dose monitoring . In its simplest form, the x-ray source and detector are scanned across the object; at each position, the detector measures the transmitted beam intensity which can be converted to the integral attenuation of the beam by the structures in its path. Following a single scan, a 1D attenuation profile of the image is created. The source-detector combination is then rotated around the patient in order to collect many 1D projections at many different angles. The collected projections can then be used to reconstruct a single 2D image of the object where each pixel represents the relative linear attenuation coefficient at that point. Attenuation values, μ, are expressed in a shifted, normalized fashion as a CT number, in Hounsfield Units:

$$HU = \frac{\mu_{tissue} - \mu_{water}}{\mu_{water}} \times 1000 \quad \text{Eq. 1-1}$$

Thus, water = 0 HU. By calibrating the CT scanner using phantoms with various tissue substitutes, a relationship between pixel value (in Hounsfield units) and

tissue density can be established. This is a particularly useful feature since it allows the CT image to be used for pixel-by-pixel tissue inhomogeneity corrections within the treatment planning system. Although inhomogeneity corrections are not always carried out (alternatively, the assumption can be made that all tissue = water), they are useful for improving the accuracy of dose calculations. Linear attenuation, μ, is directly related to absorbed dose, D, through the following equation:

$$D = \Psi \cdot \left(\frac{\mu}{\rho} \right)_{E,Z} \qquad \text{Eq. 1-2}$$

where Ψ is the energy fluence for photons of energy E, and μ/ρ is the mass energy-absorption coefficient for photons of energy E in material of atomic number Z.

Figure 1-2 illustrates the variety of materials that can be imaged with CT along with their corresponding CT numbers. Although CT is widely used in radiation therapy treatment planning (RTTP), its major drawback is that many relevant soft-tissues have very similar CT numbers. In other words, the soft tissue discrimination of CT is limited.

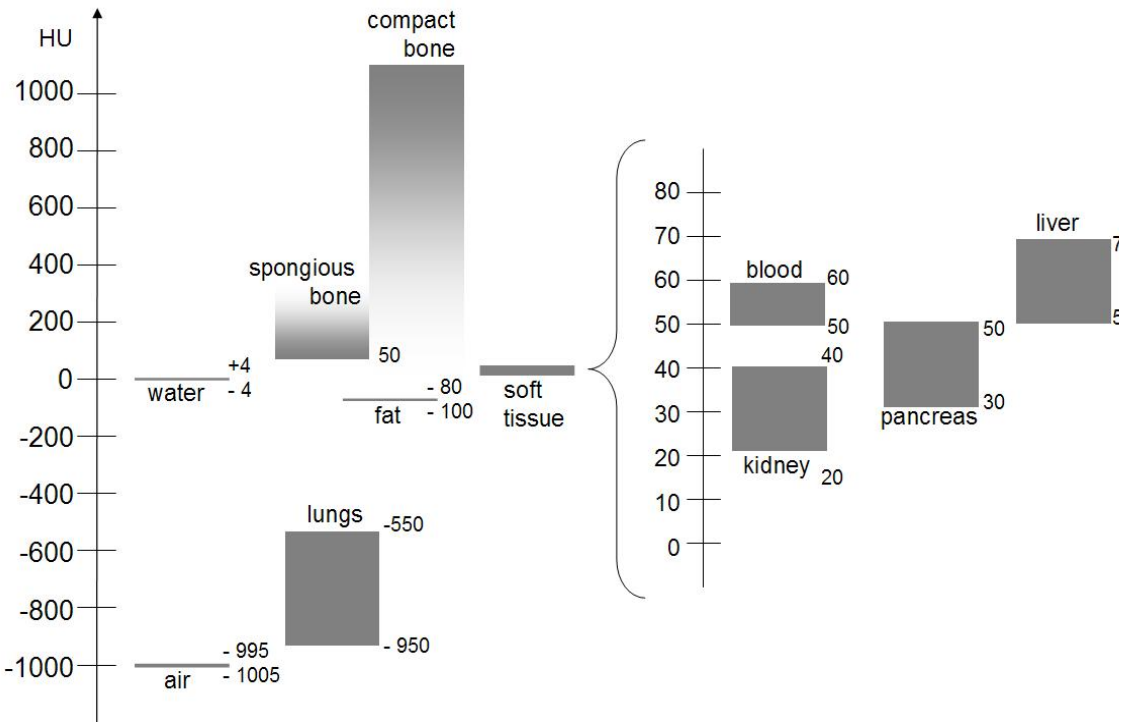

Figure 1-2

CT values, given in Hounsfield Units (H), characterize the linear attenuation coefficient, μ, of the tissue in each image voxel relative to the μ-value of water. The CT values of different tissues are therefore defined to be independent of the particular CT scanner. The range of soft tissue CT values is very narrow. Figure adapted from Kalendar.[1]

CT imaging can also be useful in later stages of the radiotherapy process, such as during patient positioning (1.3.2). Provided the CT image is acquired using the same conditions as used during treatment (i.e. flat bed, laser alignment, identical patient positioning), the planning CT image can be used to create a 2D projection

image called a digitally reconstructed radiograph (DRR). The DRR can be compared against a quick daily image of the patient made using megavoltage CT (MVCT) or an on-board imager such as an electronic portal imaging device (EPID) to guide patient positioning.

1.3.1.2. Magnetic Resonance Imaging

This section serves as a very general introduction to MRI. More details, including the principles and specifics of MRI are discussed in Chapter 2.

While CT image contrast depends on the attenuation of x-rays by tissue – a function of both atomic number and electron density, MRI image intensity is primarily a function of proton density and tissue relaxation constants. Tissues can be characterized by two fundamental parameters, which describe the response of the MR signal: the spin-lattice relaxation (T_1) and the spin-spin relaxation (T_2) (see § 2.1.3). Differences in these two tissue-specific parameters are the major source of image contrast for most MRIs. The MR image is generated by applying a series of one or more radiofrequency (RF) pulses along with magnetic field gradients, and the nature of the signal created depends on the particular timing of the pulses and gradients. Because the arrangement of the pulses and various other parameters can be infinitely varied, so too can the spin response and the resulting image contrast. This allows many different aspects of the tissue properties to be analysed through a single imaging modality. A common scanning protocol includes both a T_1-weighted spin echo sequence for good anatomical delineation and a T_2-weighted spin echo image to differentiate pathological and normal

tissues.[23] Image contrast is not, however, limited to differences in tissue relaxation; sequences can be designed to reveal information about vasculature (MR angiography), tissue perfusion, blood vessel permeability and local diffusion.

The vast array of potential contrast mechanisms available in MRI make it a uniquely flexible imaging modality. Its superb soft-tissue contrast, which can be varied by changing a number of sequence parameters, make it useful for evaluating the extent and margins of malignancies – particularly for tumours that permeate surrounding muscle. While CT reigns superior for imaging boney anatomy and for its sensitivity to calcifications, MRI may prove advantageous for imaging tumours located very near to boney structures: whereas areas surrounded by thick bone can suffer from poor contrast in CT because of the elevated absorption of x-rays by bone, the contrast in such areas is unaffected in MR. Therefore tumours located near boney prominences or enclosures, or near the base of the brainstem are more clearly imaged with MRI.[24] Furthermore, the diversity of contrast mechanisms in MRI makes it particularly well-suited for imaging CNS tumours,[25] brain abnormalities and head and neck cancers,[26] and for staging soft-tissue,[27] endometrial,[28] and pelvic tumours.[29,30] Both CT and MR are entirely non-invasive imaging modalities; however, MRI is safer for repeated use (e.g. in longitudinal studies) because it does not rely on the use of ionizing radiation.

Despite MR's superior soft-tissue contrast and other useful features, its use in the realm of oncology is still limited. The reasons for this are two-fold: 1) the geometric accuracy of MR is uncertain; and 2) there is no direct link between MRI pixel intensity and electron density which is necessary for inhomogeneity correction. The issue of MR geometric uncertainty is explored in greater length in the following chapters and will not, therefore, be discussed in this section. The absence of electron density information in MR images has been explored by a number of groups and appears to be a surmountable problem.[31-35] One way to circumvent this issue is to register MR and CT images such that the MR image can be used for structure delineation while the CT data can be used for dose calculations and isodose distributions.[31,32,34,36] Alternatively, MR images can be manually[33] or automatically[37] segmented such that bulk electron densities can be assigned, or if inhomogeneity corrections are not needed, all tissues can be assigned an electron density equal to that of water.[34]

1.3.2. Image Guided Radiation Therapy

Improved tumour imaging capabilities have opened the door for advanced treatment techniques, including CRT and IMRT. The dose distributions created with CRT and IMRT can include sharp dose gradients between targeted and surrounding tissues and are therefore unforgiving of patient misalignment and/or motion. In a circular fashion, improved target delineation has led to margin reductions and increasingly conformal dose deliveries; these developments have, in turn, led to stiffer requirements regarding tumour localisation and therefore

require the inclusion of further image guidance at later stages in the treatment process. The use of frequent imaging in the treatment room to guide the radiotherapy process is known as image guided radiation therapy, or IGRT.

It is well-known that there are unavoidable uncertainties involved in delivering radiotherapy treatments. Indeed, patient motion - both inter- and intra-fraction, positioning errors, and internal motion are taken into account when designing suitable PTV margins. However, it is important to understand and minimize the magnitude of these uncertainties and their effects on the treatment outcome. Traditionally, patient set-up was carried out by marking the patient's skin during treatment simulation and aligning the skin markings with the treatment beam during delivery. Patient immobilization was employed but conservative margins were still used to ensure tumour coverage in the event of residual set-up errors or internal motion. More recently, a variety of technologies have been introduced to image the patient during set-up in order to evaluate systematic errors, reduce them and therefore minimize the margins required to ensure appropriate dosage to the target volume.

In-room diagnostic x-ray imaging has long since been used for set-up verification[38-40] while EPIDs represent a more recent development for the acquisition of daily 2D images using the linac treatment beam.[41,42] Such images can be used to evaluate set-up errors through comparison of daily images to the simulation image (DRR) and adjust patient positioning accordingly. EPID images

can also be used for dose measurements which can provide useful comparisons between planned and delivered doses. In-suite ultrasound imaging has also been similarly used;[43-47] however, the US probe may cause displacement of the imaged volume due to applied pressure.[48,49] Helical megavoltage (MV) CT scans are routinely used to evaluate and adjust patient set-up on the Tomotherapy system.[50-52] MVCT-based daily imaging also falls short in its soft-tissue imaging capabilities; since the tumour volume can rarely be discriminated, surrogate structures (bony landmarks or implanted radio-opaque markers) must be relied upon to infer target positioning. Integrated kilovoltage CT / linac systems provide better soft-tissue contrast,[53,54] however, all x-ray and CT-based imaging techniques for patient positioning expose the patient to additional ionising radiation. The potential side effects of daily imaging combined with radiation therapy may be difficult to accurately assess, but remain important considerations.

Free of ionising radiation, the gold standard for soft-tissue discrimination remains MRI. [55,56] With this consideration in mind, there has been recent interest in integrating MR imaging capabilities with radiotherapy units.[57-61] No imaging modality is perfect, however, and MR-based IGRT offers its own set of complications, including 1) the interference of the RF transmission signal with the RF fields required for electron acceleration within the linac head,[62] and 2) alterations in dose deposition due to the presence of a magnetic field.[60,63]

1.3.3. Adaptive Radiotherapy

Adaptive radiotherapy, or ART, refers to treatments which are altered and adapted one or more times based on images acquired over the course of delivery. Adaptation can range from a single re-plan based on a second set of images after significant weight loss or alteration in tumour shape/position to real-time tumour tracking[64-66] and automatic gating[67-70] during treatment delivery. Each of these methods can effect reductions in tumour margins and may therefore contribute to decreased normal tissue toxicity. Many of the technologies discussed above as part of IGRT can be used in ART. For example, EPID transmission images can be used to evaluate differences between planned and delivered doses so that, if necessary, changes may be made to the treatment plan.[71,72] MVCT images acquired on Tomotherapy may be used to similar effect. Moreover, daily 3D MVCT Tomotherapy images can be used to monitor patient position and/or changes in tumour shape/size to adapt the treatment plan accordingly. Additionally, real-time tumour tracking is available with technologies such as Cyberknife; x-ray images are continuously acquired and used to guide the placement of the linac's treatment beam which is mounted on a robotic arm with 6 degrees of freedom.[65] Tumour motion can be tracked with implanted fiducials or miniature RF transponders,[73,74] with infrared reflective markers attached to the patient's body,[67,75,76] or via motion of a surrogate organ (e.g. diaphragm).[77] A persistent concern, however, is that tumour motion may not be well-correlated with the motion of surrogates, external markers, or fiducials placed near, but not within the tumour itself.

As with the development of image-based treatment planning and IGRT as discussed in Sections 1.3.1 and 1.3.2, the techniques of ART have evolved towards the inclusion of MRI because of its unprecedented capacity for multi-planar and soft-tissue contrast. Surrogates are not needed for tumour-tracking; however, fast imaging techniques - which may be prone to increased geometrical error - are required to generate time-resolved MR image series. Recent work has been carried out to develop tumour tracking capabilities on integrated MR/Linac systems that would allow real-time beam modification through control of the on-board multi-leaf collimator (MLC).[78]

1.4. The future of radiation therapy

The integration of a variety of imaging modalities at all steps in the radiation therapy process - from planning to treatment to evaluation and adaptation - has permitted a new level of refinement to the treatment of cancer with radiotherapy. The precise location and extent of targets can be more accurately determined, margins can be reduced, more normal tissue can be spared, and treatments can be verified and adapted, if necessary. Furthermore, dose verification allows more accurate evaluation of radiation therapy protocols such as CRT, IMRT and dose escalation which can be used to refine knowledge about population-based dose tolerances. The end result is improved local control and reduced normal tissue complications.[12-14]

The increased precision and accuracy of radiotherapy, made possible through image guidance, has also opened the door to new fractionation schemes. Hypofractionation involves the delivery of higher doses (>2.0 Gy) over fewer fractions than the 1.8-2.0 Gy over 25-35 fraction standard. Hypofractionation was previously deemed impractical because the large doses and accelerated schedule didn't allow for sufficient repair of sublethal damage on the part of normal tissue and inhibited reoxygenation and reassortment of tumour cells; such schemes were found to be detrimental to the TCP-NTCP balance.[79,80] However, with improved imaging, tumour localisation, and delivery methods, hypofractionation schemes have reported greater local control in lung cancer and liver metastasis without concomitant increases in toxicity.[81-83]

Interest in expanding the role of MRI at various stages of the radiation therapy process abounds. Although MRI cannot provide density information required for treatment planning and, further, suffers from geometric distortions, it remains highly regarded for its soft tissue imaging, multi-planar image reconstruction, and its ability to probe various aspects of tissue pathology. Provided its limitations can be overcome, the advantages of MRI permit more accurate tumour delineation during treatment planning, as well as more relevant monitoring of target and OAR positioning during both set-up and treatment. The following chapter will explore in greater detail the fundamentals of MRI formation as well as the limitations pertaining to geometric accuracy.

1.5. References

[1] W. A. Kalender, *Computed Tomography: Fundamentals, System Technology, Image Quality, Applications*, 2 ed. (Publicis Corporate Publishing, Erlangen, 2005).

[2] L. N. Baldwin, K. Wachowicz, S. D. Thomas, R. Rivest, and B. G. Fallone, "Characterization, predication, and correction of geometric distortion in 3T MR images," Med Phys **34,** 388-399 (2007).

[3] L. N. Baldwin, K. Wachowicz, and B. G. Fallone, "A two-step scheme for distortion rectification of magnetic resonance images," Med Phys **36,** 3917-26 (2009).

[4] L. N. Baldwin, K. Wachowicz, and B. G. Fallone, "Discontinuities in the distortion field: correction of the fat-shift artifact," in *Proc Intl Soc Magn Reson Med*, Stockholm, 2010, p. 3091.

[5] National Cancer Institute fact sheet 7.1: radiation therapy for cancer. http://www.cancer.gov/cancertopics/factsheet/Therapy/radiation (2010)

[6] ICRU, "Prescribing, Recording and Reporting Photon Beam Therapy, Report 62," (1999).

[7] ICRU, "Prescribing, Recording and Reporting Photon Beam Therapy, Report 50," (1993).

[8] F. M. Khan, *The Physics of Radiation Therapy*, 3 ed. (Lippincott Williams & Wilkins, 2003).

[9] L. Veldeman, I. Madani, F. Hulstaert, G. De Meerleer, M. Mareel, and W. De Neve, "Evidence behind use of intensity-modulated radiotherapy: a systematic review of comparative clinical studies," Lancet Oncol **9,** 367-75 (2008).

[10] P. L. Nguyen, A. Trofimov, and A. L. Zietman, "Proton-beam vs intensity modulated radiation therapy - Which is best for treating prostate cancer?," Oncology **22,** 748-754 (2008).

[11] A. Pollack, A. L. Hanlon, E. M. Horwitz, S. J. Feigenberg, A. A. Konski, B. Movsas, R. E. Greenberg, R. G. Uzzo, C. M. Ma, S. W. McNeeley, M. K. Buyyounouski, and R. A. Price, Jr., "Dosimetry and preliminary acute toxicity in the first 100 men treated for prostate cancer on a randomized hypofractionation dose escalation trial," Int J Radiat Oncol Biol Phys **64,** 518-26 (2006).

[12] S. T. Peeters, W. D. Heemsbergen, P. C. Koper, W. L. van Putten, A. Slot, M. F. Dielwart, J. M. Bonfrer, L. Incrocci, and J. V. Lebesque, "Dose-response in radiotherapy for localized prostate cancer: results of the Dutch multicenter randomized phase III trial comparing 68 Gy of radiotherapy with 78 Gy," J Clin Oncol **24,** 1990-6 (2006).

[13] E. H. Pow, D. L. Kwong, A. S. McMillan, M. C. Wong, J. S. Sham, L. H. Leung, and W. K. Leung, "Xerostomia and quality of life after intensity-modulated radiotherapy vs. conventional radiotherapy for early-stage nasopharyngeal carcinoma: initial report on a randomized controlled clinical trial," Int J Radiat Oncol Biol Phys **66,** 981-91 (2006).

[14] M. de Ridder, K. Tournel, Y. Van Nieuwenhove, B. Engels, and A. Hoorens, "Phase II study of preoperative helical tomotherapy for rectal cancer," Int J Radiat Oncol Biol Phys **70,** 728-734 (2008).

[15] J. M. Balter and M. L. Kessler, "Imaging and alignment for image-guided radiation therapy," J Clin Oncol **25,** 931-7 (2007).

[16] V. Gregoire, "Is there any future in radiotherapy planning without the use of PET: unraveling the myth," Radiother Oncol **73,** 261-3 (2004).

[17] S. L. Sailer, J. G. Rosenman, M. Soltys, T. J. Cullip, and J. Chen, "Improving treatment planning accuracy through multimodality imaging," Int J Radiat Oncol Biol Phys **35,** 117-24 (1996).

[18] D. Wang, C. J. Schultz, P. A. Jursinic, M. Bialkowski, X. R. Zhu, and W. D. Brown, "Initial experience of FDG-PET/CT guided IMRT of head-and-neck carcinoma," Int J Radiat Oncol Biol Phys **65,** 143-151 (2006).

[19] S. S. Gambhir, "Molecular imaging of cancer with positron emission tomography," Nat Rev Cancer **2,** 683-93 (2002).

[20] G. S. Payne and M. O. Leach, "Applications of magnetic resonance spectroscopy in radiotherapy treatment planning," Br J Radiol **79 Spec No 1,** S16-26 (2006).

[21] B. Pickett, E. Vigneault, J. Kurhanewicz, L. Verhey, and M. Roach, "Static field intensity modulation to treat a dominant intra-prostatic lesion to 90 Gy compared to seven field 3-dimensional radiotherapy," Int J Radiat Oncol Biol Phys **44,** 921-9 (1999).

[22] J. Pouliot, Y. Kim, E. Lessard, I. C. Hsu, D. B. Vigneron, and J. Kurhanewicz, "Inverse planning for HDR prostate brachytherapy used to boost dominant intraprostatic lesions defined by magnetic resonance spectroscopy imaging," Int J Radiat Oncol Biol Phys **59,** 1196-207 (2004).

[23] R. E. Hendrick and U. Raff, "Image contrast and noise," in *Magnetic Resonance Imaging*, edited by D. D. Stark and W. G. Bradley (Mosby Year Book, St. Louis, 1992).

[24] D. G. Bragg and A. G. Osborn, "CNS imaging of neoplasms," Int J Radiat Oncol Biol Phys **21,** 841-845 (1991).

[25] L. S. De Vries and G. M. Bydder, "Tumors of the central nervous system," in *Magnetic Resonance Imaging (MRI)*, edited by C. C. Partain, R. R. Price, J. A. Patton, and W. B. Saunders (Philadelphia, 1988), p. 144-168.

[26] G. Sze, "Gadolinium-DPTA in spinal disease," Radiol. Clin. North Am. **26,** 1009-1024 (1988).

[27] K. Herrlin, L. Bi Ling, H. Pettersson, H. Willen, and A. Rydholm, "Gadolinium-DPTA enhancement of soft tissue tumors in magnetic resonance imaging," Acta Radiologica **31,** 233-236 (1990).

[28] S. Peungjesada, P. R. Bhosale, A. Balachandran, and R. B. Iyer, "Magnetic resonance imaging of endometrial carcinoma," J Comp Assist Tomogr **33,** 601-608 (2009).

[29] H. Hricak, in *Important Advances in Oncology*, edited by V. T. DeVita, S. Hellman, and S. A. Rosenberg (J B Lippincott, Philadelphia, 1991), p. 103-133.

[30] V. S. Khoo, A. R. Padhani, S. F. Tanner, D. J. Finnigan, M. O. Leach, and D. P. Dearnaley, "Comparison of MRI with CT for the radiotherapy planning of prostate cancer: a feasibility study," Br J Radiol **72,** 590-7 (1999).

[31] L. Chen, R. A. Price, Jr., T. B. Nguyen, L. Wang, J. S. Li, L. Qin, M. Ding, E. Palacio, C. M. Ma, and A. Pollack, "Dosimetric evaluation of MRI-based treatment planning for prostate cancer," Phys Med Biol **49,** 5157-5170 (2004).

[32] L. Chen, R. A. Price, Jr., L. Wang, J. Li, L. Qin, S. McNeeley, C. M. Ma, G. M. Freedman, and A. Pollack, "MRI-based treatment planning for radiotherapy: dosimetric verification for prostate IMRT," Int J Radiat Oncol Biol Phys **60,** 636-647 (2004).

[33] Y. K. Lee, M. Bollet, G. Charles-Edwards, M. A. Flower, M. O. Leach, H. McNair, E. Moore, C. Rowbottom, and S. Webb, "Radiotherapy treatment planning of prostate cancer using magnetic resonance imaging alone," Radiotherapy and Oncology **66,** 203-216 (2003).

[34] R. Prabhakar, P. K. Julka, T. Ganesh, A. Munshi, R. C. Joshi, and G. K. Rath, "Feasibility of using MRI alone for 3D radiation treatment planning in brain tumors," Jpn J Clin Oncol **37,** 405-411 (2007).

[35] T. Stanescu, H.-S. Jans, N. Pervez, P. Stavrev, and B. Fallone, "A study on the magnetic resonance imaging (MRI)-based radiation treatment planning of intracranial lesions," Physics in Medicine and Biology **53,** 3579-3593 (2008).

[36] A. S. Jackson, S. A. Reinsberg, S. A. Sohaib, E. M. Charles-Edwards, S. A. Mangar, C. P. South, M. O. Leach, and D. P. Dearnaley, "Distortion-corrected T2 weighted MRI: a novel approach to prostate radiotherapy planning," Br J Radiol **80,** 926-933 (2007).

[37] D. Pasquier, T. Lacornerie, M. Vermandel, J. Rousseau, E. Lartigau, and N. Betrouni, "Automatic segmentation of pelvic structures from magnetic resonance images for prostate cancer radiotherapy," Int J Radiat Oncol Biol Phys **68,** 592-600 (2007).

[38] A. F. Holloway, "A localising device for a rotating cobalt therapy unit," Br J Radiol **31,** 227 (1958).

[39] H. E. Johns and J. R. Cunningham, "A precision cobalt 60 unit for fixed field and rotation therapy," Am J Roentgenol Radium Ther Nucl Med **81,** 4-12 (1959).

[40] M. Weissbluth, C. J. Karzmark, R. E. Steele, and A. H. Selby, "The Stanford medical linear accelerator. II. Installation and physical measurements," Radiology **72,** 242-53 (1959).

[41] A. Ezz, P. Munro, A. T. Porter, J. Battista, D. A. Jaffray, A. Fenster, and S. Osborne, "Daily monitoring and correction of radiation field placement using a video-based portal imaging system: a pilot study," Int J Radiat Oncol Biol Phys **22,** 159-65 (1992).

[42] W. J. De Neve, M. Van den Heuval, M. Coghe, L. Thon, and P. De Roover, "Routine clinical on-line portal imaging followed by immediate field adjustment using a tele-controlled patient couch," Radiother Oncol **24,** 45-54 (1992).

[43] E. J. Holupka, I. D. Kaplan, E. C. Burdette, and G. K. Svensson, "Ultrasound image fusion for external beam radiotherapy for prostate cancer," Int J Radiat Oncol Biol Phys **35,** 975-84 (1996).

[44] D. S. Mohan, P. A. Kupelian, and T. R. Willoughby, "Short-course intensity-modulated radiotherapy for localized prostate cancer with daily transabdominal ultrasound localization of the prostate gland," Int J Radiat Oncol Biol Phys **46,** 575-80 (2000).

[45] D. A. Kuban, L. Dong, R. Cheung, E. Strom, and R. De Crevoisier, "Ultrasound-based localization," Semin Radiat Oncol **15,** 180-91 (2005).

[46] J. Lattanzi, S. McNeeley, W. Pinover, E. Horwitz, I. Das, T. E. Schultheiss, and G. E. Hanks, "A comparison of daily CT localization to a daily ultrasound-based system in prostate cancer," Int J Radiat Oncol Biol Phys **43,** 719-25 (1999).

[47] M. Van den Heuval, T. Powell, E. Seppi, P. Littrupp, M. Khan, Y. Wang, and J. Forman, "Independent verification of ultrasound based image-guided radiation treatment, using electronic portal imaging and implanted gold markers," Med Phys **30,** 2878-2887 (2003).

[48] K. M. Langen, J. Pouliot, C. Anezinos, M. Aubin, A. R. Gottschalk, I. C. Hsu, D. Lowther, Y. M. Liu, K. Shinohara, L. J. Verhey, V. Weinberg, and M. Roach, 3rd, "Evaluation of ultrasound-based prostate localization for image-guided radiotherapy," Int J Radiat Oncol Biol Phys **57,** 635-44 (2003).

[49] X. Artignan, M. H. Smitsmans, J. V. Lebesque, D. A. Jaffray, M. van Herk, and H. Bartelink, "Online ultrasound image guidance for radiotherapy of prostate cancer: impact of image acquisition on prostate displacement," Int J Radiat Oncol Biol Phys **59,** 595-601 (2004).

[50] K. M. Langen, S. L. Meeks, D. O. Poole, T. H. Wagner, T. R. Willoughby, P. A. Kupelian, K. J. Ruchala, J. Haimerl, and G. H. Olivera, "The use of megavoltage CT (MVCT) images for dose recomputations," Phys Med Biol **50,** 4259-76 (2005).

[51] T. R. Mackie, J. Kapatoes, K. Ruchala, W. Lu, C. Wu, G. Olivera, L. Forrest, W. Tome, J. Welsh, R. Jeraj, P. Harari, P. Reckwerdt, B. Paliwal, M. Ritter, H. Keller, J. Fowler, and M. Mehta, "Image guidance for precise conformal radiotherapy," Int J Radiat Oncol Biol Phys **56,** 89-105 (2003).

[52] K. M. Langen, Y. Zhang, R. D. Andrews, M. E. Hurley, S. L. Meeks, D. O. Poole, T. R. Willoughby, and P. A. Kupelian, "Initial experience with megavoltage (MV) CT guidance for daily prostate alignments," Int J Radiat Oncol Biol Phys **62,** 1517-24 (2005).

[53] L. Court, I. Rosen, R. Mohan, and L. Dong, "Evaluation of mechanical precision and alignment uncertainties for an integrated CT/LINAC system," Med Phys **30,** 1198-210 (2003).

[54] K. Kuriyama, H. Onishi, N. Sano, T. Komiyama, Y. Aikawa, Y. Tateda, T. Araki, and M. Uematsu, "A new irradiation unit constructed of self-moving gantry-CT and linac," Int J Radiat Oncol Biol Phys **55,** 428-35 (2003).

[55] P. C. Johnson, S. J. Hunt, and B. P. Drayer, "Human cerebral gliomas: correlation of postmortem MR imaging and neuropathologic findings," Radiology **170,** 211-7 (1989).

[56] M. Brant-Zawadzki, "MR imaging of the brain," Radiology **166,** 1-10 (1988).

[57] A. J. Raaijmakers, B. W. Raaymakers, S. van der Meer, and J. J. Lagendijk, "Integrating a MRI scanner with a 6 MV radiotherapy accelerator: impact of the surface orientation on the entrance and exit dose due to the transverse magnetic field," Phys Med Biol **52,** 929-39 (2007).

[58] B. W. Raaymakers, A. J. Raaijmakers, A. N. Kotte, D. Jette, and J. J. Lagendijk, "Integrating a MRI scanner with a 6 MV radiotherapy accelerator: dose deposition in a transverse magnetic field," Phys Med Biol **49,** 4109-18 (2004).

[59] B. G. Fallone, B. Murray, S. Rathee, T. Stanescu, S. Steciw, S. Vidakovic, E. Blosser, and D. Tymofichuk, "First MR images obtained during megavoltage photon irradiation from a prototype integrated linac-MR system," Med Phys **36,** 2084-8 (2009).

[60] C. Kirkby, T. Stanescu, and B. G. Fallone, "Magnetic field effects on the energy deposition spectra of MV photon radiation," Phys Med Biol **54,** 243-57 (2009).

[61] C. Kirkby, T. Stanescu, S. Rathee, M. Carlone, B. Murray, and B. G. Fallone, "Patient dosimetry for hybrid MRI-radiotherapy systems," Med Phys **35,** 1019-27 (2008).

[62] B. Burke, M. Lamey, S. Rathee, B. Murray, and B. G. Fallone, "Radio frequency noise from clinical linear accelerators," Phys Med Biol **54,** 2483-92 (2009).

[63] A. J. Raaijmakers, B. W. Raaymakers, and J. J. Lagendijk, "Experimental verification of magnetic field dose effects for the MRI-accelerator," Phys Med Biol **52,** 4283-91 (2007).

[64] M. J. Murphy, J. R. Adler, Jr., M. Bodduluri, J. Dooley, K. Forster, J. Hai, Q. Le, G. Luxton, D. Martin, and J. Poen, "Image-guided radiosurgery for the spine and pancreas," Comput Aided Surg **5,** 278-88 (2000).

[65] M. J. Murphy, "An automatic six-degree-of-freedom image registration algorithm for image-guided frameless stereotaxic radiosurgery," Med Phys **24,** 857-66 (1997).

[66] P. J. Keall, V. R. Kini, S. S. Vedam, and R. Mohan, "Motion adaptive x-ray therapy: a feasibility study," Phys Med Biol **46,** 1-10 (2001).

[67] H. Shirato, S. Shimizu, K. Kitamura, T. Nishioka, K. Kagei, S. Hashimoto, H. Aoyama, T. Kunieda, N. Shinohara, H. Dosaka-Akita, and K. Miyasaka, "Four-dimensional treatment planning and fluoroscopic real-time tumor tracking radiotherapy for moving tumor," Int J Radiat Oncol Biol Phys **48,** 435-42 (2000).

[68] H. Shirato, S. Shimizu, T. Kunieda, K. Kitamura, M. van Herk, K. Kagei, T. Nishioka, S. Hashimoto, K. Fujita, H. Aoyama, K. Tsuchiya, K. Kudo, and K. Miyasaka, "Physical aspects of a real-time tumor-tracking system for gated radiotherapy," Int J Radiat Oncol Biol Phys **48,** 1187-95 (2000).

[69] D. Verellen, K. Tournel, N. Linthout, G. Soete, T. Wauters, and G. Storme, "Importing measured field fluences into the treatment planning system to validate a breathing synchronized DMLC-IMRT irradiation technique," Radiother Oncol **78,** 332-8 (2006).

[70] K. Ohara, T. Okumura, M. Akisada, T. Inada, T. Mori, H. Yokota, and M. J. Calaguas, "Irradiation synchronized with respiration gate," Int J Radiat Oncol Biol Phys **17,** 853-7 (1989).

[71] V. N. Hansen, P. M. Evans, and W. Swindell, "The application of transit dosimetry to precision radiotherapy," Med Phys **23,** 713-21 (1996).

[72] K. L. Pasma, B. J. Heijmen, M. Kroonwijk, and A. G. Visser, "Portal dose image (PDI) prediction for dosimetric treatment verification in radiotherapy. I. An algorithm for open beams," Med Phys **25,** 830-40 (1998).

[73] C. Noel, P. J. Parikh, M. Roy, P. Kupelian, A. Mahadevan, G. Weinstein, C. Enke, N. Flores, D. Beyer, and L. Levine, "Prediction of intrafraction prostate motion: accuracy of pre- and post-treatment imaging and intermittent imaging," Int J Radiat Oncol Biol Phys **73,** 692-8 (2009).

[74] L. Santanam, K. Malinowski, J. Hubenshmidt, S. Dimmer, M. L. Mayse, J. Bradley, A. Chaudhari, K. Lechleiter, S. K. Goddu, J. Esthappan, S. Mutic, D. A. Low, and P. Parikh, "Fiducial-based translational localization accuracy of electromagnetic tracking system and on-board kilovoltage imaging system," Int J Radiat Oncol Biol Phys **70,** 892-9 (2008).

[75] A. Schweikard, G. Glosser, M. Bodduluri, M. J. Murphy, and J. R. Adler, "Robotic motion compensation for respiratory movement during radiosurgery," Comput Aided Surg **5,** 263-77 (2000).

[76] J. de Mey, J. Van de Steene, F. Vandenbroucke, D. Verellen, and L. Trappeniers, "Percutaneous placement of marking coils before stereotactic radiation therapy of malignant lung lesions," Journal of Vascular and Interventional Radiology **16,** 51-56 (2005).

[77] G. S. Mageras, E. Yorke, K. Rosenzweig, L. Braban, E. Keatley, E. Ford, S. A. Leibel, and C. C. Ling, "Fluoroscopic evaluation of diaphragmatic motion reduction with a respiratory gated radiotherapy system," J Appl Clin Med Phys **2,** 191-200 (2001).

[78] J. Yun, D. Robinson, M. MacKenzie, S. Rathee, B. Murray, and B. G. Fallone, "Real-time MR tumour tracking and dose adaptation," Med Phys **36,** 4301 (2009).

[79] G. H. Fletcher, "Hypofractionation: lessons from complications," Radiother Oncol **20,** 10-5 (1991).

[80] D. Harrison, E. Crennan, D. Cruickshank, P. Hughes, and D. Ball, "Hypofractionation reduces the therapeutic ratio in early glottic carcinoma," Int J Radiat Oncol Biol Phys **15,** 365-72 (1988).

[81] K. K. Herfarth, J. Debus, F. Lohr, M. L. Bahner, B. Rhein, P. Fritz, A. Hoss, W. Schlegel, and M. F. Wannenmacher, "Stereotactic single-dose radiation therapy of liver tumors: results of a phase I/II trial," J Clin Oncol **19,** 164-70 (2001).

[82] Y. Nagata, K. Takayama, Y. Matsuo, Y. Norihisa, T. Mizowaki, T. Sakamoto, M. Sakamoto, M. Mitsumori, K. Shibuya, N. Araki, S. Yano, and M. Hiraoka, "Clinical outcomes of a phase I/II study of 48 Gy of stereotactic body radiotherapy in 4 fractions for primary lung cancer using a stereotactic body frame," Int J Radiat Oncol Biol Phys **63,** 1427-31 (2005).

[83] T. Xia, H. Li, Q. Sun, Y. Wang, N. Fan, Y. Yu, P. Li, and J. Y. Chang, "Promising clinical outcome of stereotactic body radiation therapy for patients with inoperable Stage I/II non-small-cell lung cancer," Int J Radiat Oncol Biol Phys **66,** 117-25 (2006).

2. Chapter 2: MRI basics and the distortion problem

As described in Chapter 1, MR images have the potential for great impact within the realm of image guided radiation therapy. This potential stems from the array of tissue parameters, which contribute to the unique soft-tissue imaging capabilities of MRI. Information provided by MR can be used to guide accurate placement of the GTV, to indicate metabolic and functional changes in tissues (useful for determining biological target volume), to assist in patient set-up and positioning, and to assess treatment response. The following chapter is concerned with the basics of MR image formation, and explores in greater detail the limitations of using MR in treatment planning procedures; namely, the issue of image distortion is investigated and potential distortion rectification schemes are reviewed.

2.1. MRI: the background

Magnetic Resonance Imaging is a powerful, non-invasive imaging technique based on the principle of nuclear magnetic resonance (NMR). NMR was independently described in 1946 by Bloch[1] and Purcell[2] and marked a discovery for which they were jointly awarded the 1952 Nobel Prize in Physics. Bloembergen *et al* soon carried out studies regarding the T_1 and T_2 relaxation characteristics of various substances[3], and in the decades that followed NMR was

primarily used to study the chemical structure of various molecules and substances through NMR spectroscopy. In the early 1970s, two discoveries helped to open wide the door for applications of NMR to the study of cancers: first, Damadian showed that T_1 and T_2 relaxation times could be used to distinguish between malignant and normal tissues[4], then, two years later, Lauterbur described the method by which he was able to harness the NMR signal from two water-filled test tubes to create an image[5] based on projection reconstruction. The latter development was the first of many proposed imaging schemes that were investigated in the following decades.[6-10]

2.1.1. General Description of NMR

2.1.1.1. The nuclear magnetic moment in a static magnetic field

Any atomic nucleus with an odd number of protons and/or neutrons has a magnetic moment and can interact with a magnetic field. The NMR phenomenon arises from the interaction of such a nuclei with two fields: 1) a static magnetic field, B_0, and 2) a rotating magnetic field $B_1(t)$. In the absence of any external fields, the nuclear magnetic moments or "spins" – represented as μ – are randomly oriented (Figure 2-1A). With the introduction of the B_0 field, two energy states are created, one in which spins are parallel to B_0 and one in which they are anti-parallel (Figure 2-1B). The energy difference between the two states is the so-called Zeeman splitting energy, E_z, and is given as

$$E_z = -\mu \cdot B_0 \qquad \text{Eq. 2-1}$$

As suggested by the minus sign, the spins are aligned parallel to the field in the lower energy state (Figure 2-1C). At finite temperature, *T*, both parallel and anti-parallel states are populated and the ratio of their population is given by the Boltzman factor:

$$\frac{n_{\downarrow}}{n_{\uparrow}} = e^{-E_z/kT} \qquad \text{Eq. 2-2}$$

where *k* is the Maxwell-Boltzman constant and $n\downarrow$ and $n\uparrow$ represent the number of spins in the anti-parallel and parallel states, respectively. At room temperature (300K), Eq. 2-2 shows there is only a very, very small excess of spins in the lower energy state parallel to B_0, even at field strengths on the order of several Tesla. Fortunately, the human body is composed largely of water; as such, it contains millions of such spins in the form of the hydrogen nuclei, ${}^{1}H$, on the water molecule, H_20. Macroscopically, the quantity of importance becomes the net magnetization, *M*, where $M = \sum_i \mu_i$. M points along the direction of B_0 as illustrated in Figure 2-2A.

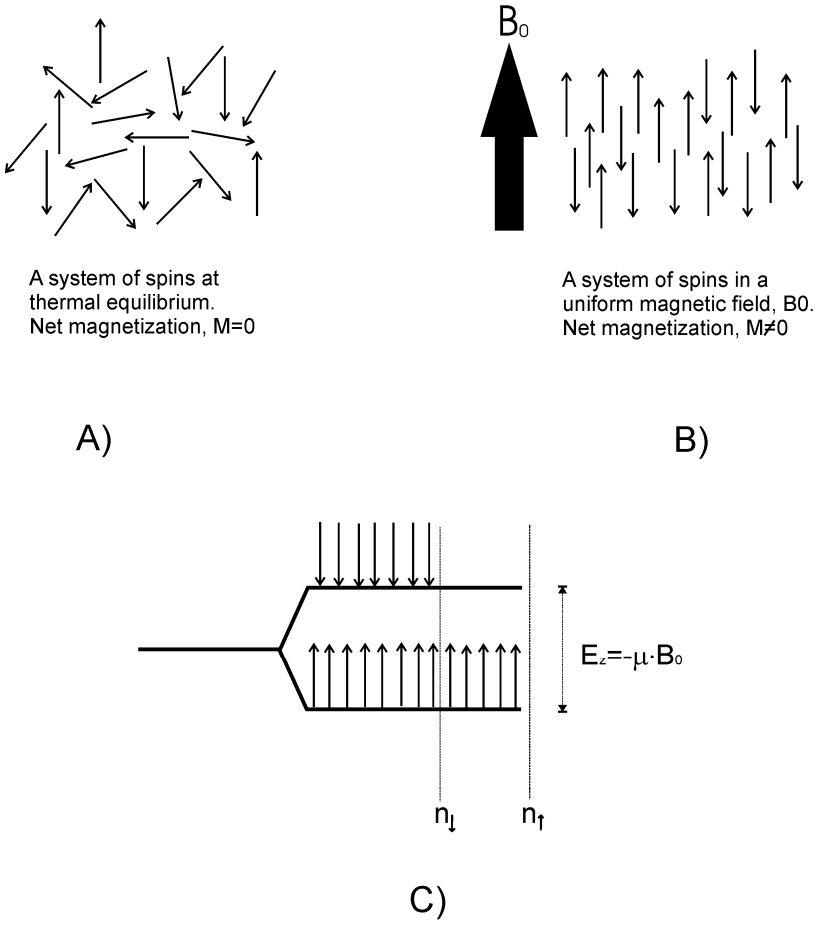

Figure 2-1

A) In the absence of an external magnetic field, the nuclear spins are randomly oriented and net magnetization, *M*, is zero. B) When a magnetic field is present, nuclear spins align themselves both parallel and anti-parallel to the external field. At non-zero temperatures, the net magnetization of the sample is small but finite, *M≠0*. C) The external field creates two distinct energy states; at room temperature, a small majority of the spins are found in the lower energy state. The ratio $n\downarrow$: $n\uparrow$ increases as the temperature decreases and as the background field strength increases.

Not only does the external field serve to polarize the spins, resulting in net magnetization, *M*, it also defines the frequency at which the spins exhibit resonance. The resonance or Larmor frequency is defined as:

$$\omega_0 = \gamma \cdot B_0 \qquad \text{Eq. 2-3}$$

where γ is the gyromagnetic ratio and is a constant, unique for each type of atom. For ^1H, γ is 42.58 MHz/T; at 3 T, ^1H therefore exhibits resonance in the radiofrequency (RF) range at 127.8 MHz.

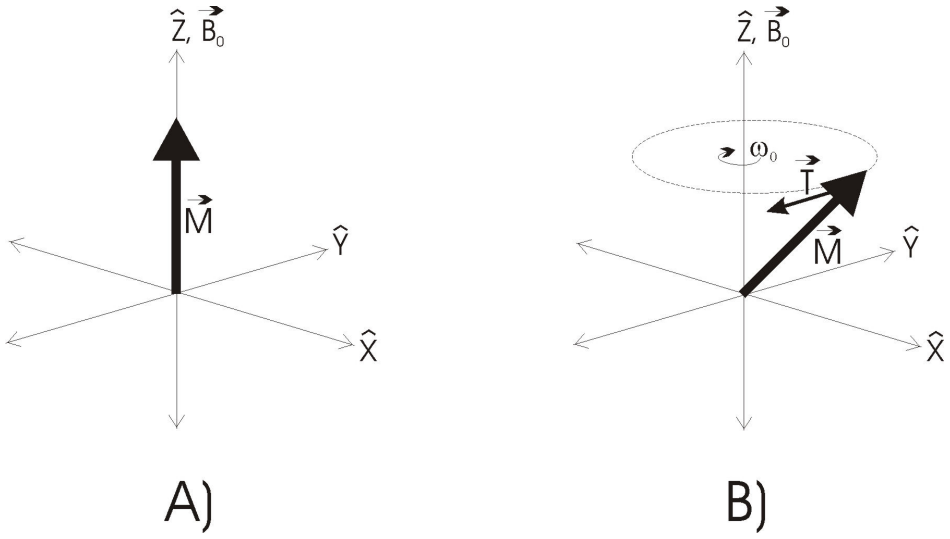

Figure 2-2

A) The magnetization vector, *M*, is aligned with the external field B_0. B) *M* is tipped away from B_0 and experiences a torque which causes it to precess about B_0 at the Larmor frequency given by Eq. 2-3.

2.1.1.2.Excitation of the magnetization vector

The net magnetisation vector may be tipped away from its thermal equilibrium position based on the principle of magnetic resonance. A weak, circularly-polarised, radiofrequency magnetic field, $B_1(t)$, can be applied in a direction orthogonal to the strong magnetic field and used to tip the magnetization vector to an angle, α, away from the B_0 direction. The amplitude of the circularly polarized field is considerably smaller than that of the main field and is ineffective unless operated near the resonance frequency, ω_0. Once the magnetization vector has been tipped away from equilibrium, it will experience a torque, *T,* which governs its motion in the static field:

$$\vec{T} = \frac{d\vec{M}}{dt} = \vec{M} \times \vec{B}_0 \qquad \text{Eq. 2-4}$$

This torque will cause M to rotate around B_0 at the Larmor frequency as illustrated in Figure 2-2B.

2.1.1.3. Signal acquisition

So far we have 1) prepared the system by creating a spin excess with net magnetization aligned with B_0 along the z-axis, and 2) excited the system by perturbing the spins away from their equilibrium position and into the transverse plane. To complete the NMR experiment, we must detect the signal created by the spins as they precess about B_0 at the Larmor frequency, ω_0. This can be done by surrounding the system with a receiving coil. Provided the spins rotate

coherently, then as they return to their equilibrium position, their oscillation about B_0 at frequency ω_0 will create a sinusoidally varying signal that can be detected and recorded. Due to both longitudinal and transverse relaxation (see §2.1.3), the signal will decay with an exponential time constant as the spins gradually relax back to their equilibrium position (parallel to B_0). The resulting signal is a sinusoid typically modulated by exponential decay and is known as free induction decay, or FID. It is shown in both the time and frequency domains in Figure 2-3 below.

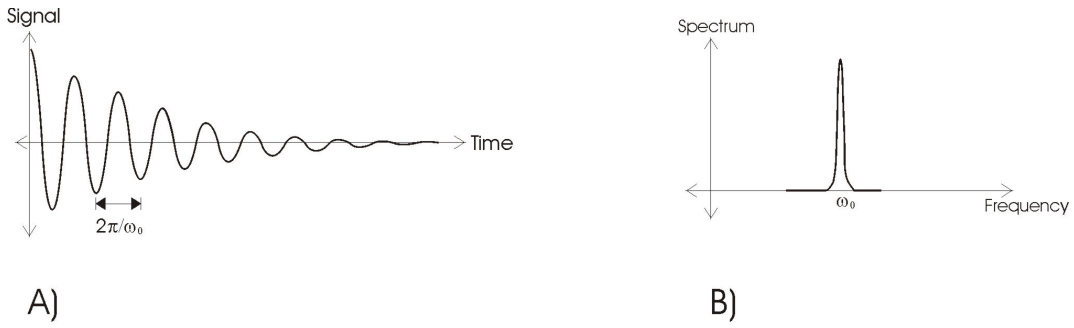

Figure 2-3

A) The time domain signal generated as the magnetization vector precesses about the B_0 field at frequency ω_0. B) the corresponding frequency-domain signal with a peak at ω_0.

2.1.2. The Rotating Frame and the Bloch Equation

In the presence of both the static and circularly polarized fields, B_0 and $B_1(t)$, the description of the motion for the magnetization vector is greatly simplified by invoking the concept of a rotating reference frame. The transverse plane of the rotating reference frame rotates with the frequency of the $B_1(t)$ field, ω_0. The coordinates of the rotating frame, $\hat{x}_\rho, \hat{y}_\rho, \hat{z}_\rho$ are given in terms of the stationary frame coordinates, $\hat{x}, \hat{y}, \hat{z}$ as:

$$\begin{aligned} \hat{x}_\rho &= \cos(\omega t)\hat{x} - \sin(\omega t)\hat{y} \\ \hat{y}_\rho &= \sin(\omega t)\hat{x} + \cos(\omega t)\hat{y} \\ \hat{z}_\rho &= \hat{z} \end{aligned} \qquad \text{Eq. 2-5}$$

In the rotating frame, the B_0 and $B_1(t)$ fields combine to create B_{eff} where

$$\vec{B}_{eff} = B_1\hat{x}_\rho + (B_0 + \omega/\gamma)\hat{z}_\rho \qquad \text{Eq. 2-6}$$

The original equation of motion, Eq. 2-4, can thus can be rewritten as

$$\frac{d\vec{M}_\rho}{dt} = \gamma\vec{M}_\rho \times \vec{B}_{eff} \qquad \text{Eq. 2-7}$$

In the rotating reference frame, the magnetization vector will precess at frequency ω_{eff} along the surface of a cone centered about the direction of $\vec{B}_{eff}$. This is illustrated in Figure 2-4.

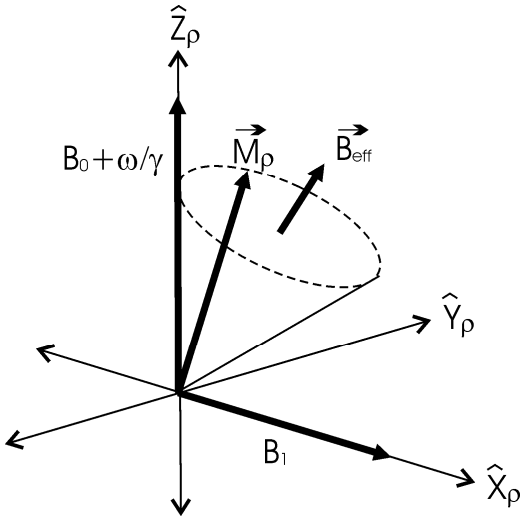

Figure 2-4

The motion of the magnetization vector, $\vec{M}_\rho$, around $\vec{B}_{eff}$ in the rotating frame.

If $B_1(t)$ is made to rotate in the negative sense at a frequency matched to the Larmor frequency of the spins, then Eq. 2-6 indicates that $\vec{B}_{eff}$ points along x_ρ and the cone of precession flattens to a circle in the $y_\rho z_\rho$ plane. The motion of $\vec{M}_\rho$ under such conditions is illustrated in both the laboratory frame and the rotating frame in Figure 2-5. The motion of the magnetization vector is clearly simplified by using the rotating frame.

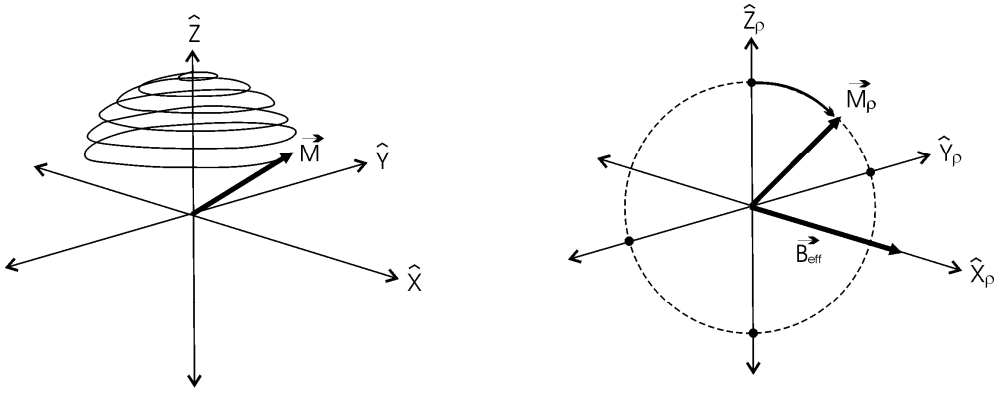

Figure 2-5

Motion of the magnetization vector following RF excitation in the A) lab frame, and B) rotating frame.

The angle between the magnetization vector before and immediately after excitation is called the tip angle and is determined by the length of time for which $B_1(t)$ is applied. The tip angle is defined as

$$\alpha(t) = \gamma \int B_1(t) \cdot dt \qquad \text{Eq. 2-8}$$

For α=90°, the final $\vec{M}_\rho$ lies along the y_ρ axis in the rotating frame, while for α=180°, the final $\vec{M}_\rho$ lies along the $-z_\rho$ axis.

2.1.3. Relaxation and Contrast Mechanisms

Although the description of the magnetization vector and its motion has thus far implied that precession about B_0 will continue without end following RF

excitation, this is not true. Instead, the magnetization vector which has been perturbed from its position along the z-axis will gradually return to its equilibrium state over time. This occurs due to relaxation and results in both recovery of the *z*-component, M_z, and decay of the transverse component, M_{xy}. The related mechanisms of longitudinal and transverse relaxation are responsible for the richness of the soft-tissue contrast found in MRI and are discussed in the following sections.

2.1.3.1. Longitudinal Relaxation

After the magnetization vector has been tipped away from the B_0 axis and the longitudinal magnetization M_z=0, the system will relax back to its thermal equilibrium state with M_z=M_0. The recovery of M_z is governed – to a first approximation – by the first order rate equation:

$$\frac{dM_z(t)}{dt} = -\frac{1}{T_1}(M_0 - M_z(t)) \qquad \text{Eq. 2-9}$$

where T_1 is the longitudinal (or spin-lattice) time constant.. Following 90° excitation, the solution to Eq. 2-9 is:

$$M_z(t) = M_0(1 - e^{-t/T1}) \qquad \text{Eq. 2-10}$$

while following 180° excitation, the solution is:

$$M_z(t) = M_0(1 - 2e^{-t/T1}) \qquad \text{Eq. 2-11}$$

Physically, T_1 is governed by the exchange of energy between the nuclear spins and the surrounding lattice. Each of the protons is a magnetic dipole; as such, each one is surrounded by millions of other magnetic fields produced by the neighbouring dipoles. These result in randomly fluctuating magnetic fields due to the thermal motion of the parent molecules. The magnetic field fluctuations occur at all frequencies, but only those occurring at certain frequencies (ω_0 and $2\omega_0$) can induce transitions between $n\downarrow$ and $n\uparrow$ populations. Because the resonance frequency increases with increasing B_0 (Eq. 2-3), the energy needed to induce transitions also increases with increasing B_0. Hence, T_1 is field strength dependent and lengthens at larger B_0.

The effect of T_1 relaxation on image contrast can be demonstrated by considering an initial 180° excitation, i.e. M_z=-M_0. Figure 2-6 illustrates the case when a sample consists of two species with different T_1 values, T_{1a}>T_{1b}. Both species will relax back to their thermal equilibrium states, but at different rates as determined by their intrinsic T_1 values. If a second 90° excitation is applied just as one of the species passes through the null point (M_z=0), signal from that tissue will be suppressed. This type of sequence is known as inversion recovery.

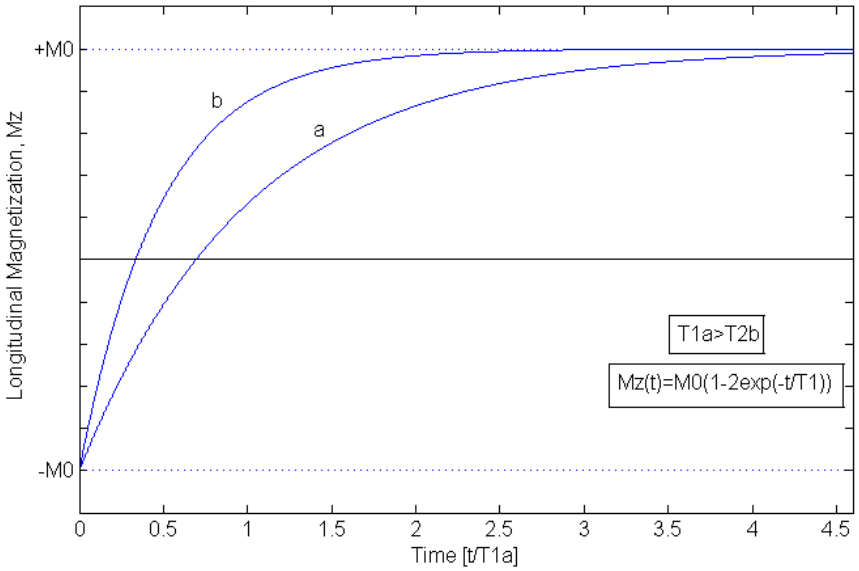

Figure 2-6

T_1 relaxation and loingitudinal magnetization decay. Two tissues – *a* and *b* – have different spin-lattice relaxation constants where $T_{1a}>T_{1b}$. The recovery of the longitudinal magnetization for tissues *a* and *b* following spin inversion is illustrated. If a second RF excitation pulse is applied when either $(M_z)_a = 0$ or $(M_z)_b=0$, signal from tissue *a* or *b*, respectively, will be nulled.

2.1.3.2.Transverse Relaxation

The same fluctuations in neighbouring dipole fields due to thermal motion that cause T_1 relaxation also contribute to irreversible dephasing of the transverse magnetization by causing the field at the nucleus to be time dependent. In the presence of field fluctuations caused by dipole motion, the total local field can be written as

$$B = B_0 + b(x, y, z, t) \qquad \text{Eq. 2-12}$$

Thus, the Larmor frequencies of the individual spins are spread amongst the range

$$\omega_{precess}(x, y, z, t) = \omega_0 + \Omega(x, y, z, t) \qquad \text{Eq. 2-13}$$

where $\Omega(x,y,z,t)$ can increase or decrease the resonance frequency, ω_0. The end result of these local, microscopic, time-dependent field fluctuations, is dephasing of the formerly coherent magnetization vector, M_{xy}, as shown in Figure 2-7. The decay of the transverse magnetization is similarly described by a first order rate equation:

$$\frac{dM_{xy}(t)}{dt} = -\frac{M_{xy}}{T_2} \qquad \text{Eq. 2-14}$$

with solution (after 90° excitation and $M_{xy} = M_0$):

$$M_{xy}(t) = M_0 e^{-t/T2} \qquad \text{Eq. 2-15}$$

T_2 characterizes the decay of M_{xy} and is known as the spin-spin or transverse relaxation time.

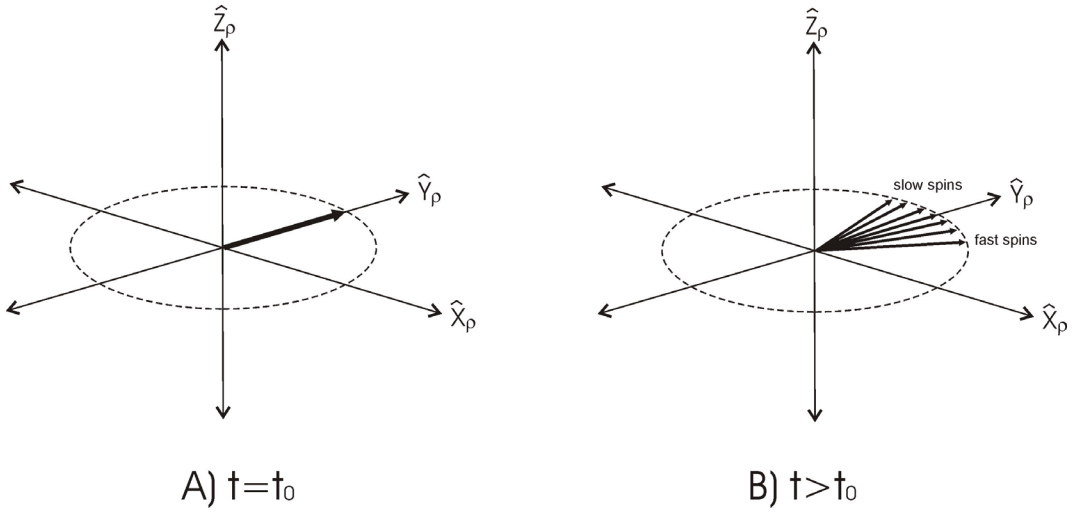

Figure 2-7

A) Immediately following 90° excitation, the magnetization vector lies along the y_ρ axis in the rotating frame and $M_{xy}=M_0$. B) Because of imperfections in the local field, some spins precess with either $\omega > \omega_0$ or $\omega < \omega_0$. Over time, this results in spin dephasing, net reduction in the value of M_{xy}, and signal decay.

The local magnetic field fluctuations which contribute to transverse relaxation have both time-dependent and static contributions. Variations in local tissue susceptibility as well as biological accumulations of paramagnetic centers (e.g. iron) may cause static field inhomogeneities. These static contributions to local field inhomogeneities can be represented by $\phi(x,y,z)$. Adding this term to Eq. 2-12 yields a total local magnetic field, $B(x,y,z,t)$ expressed as

$$B(x,y,z,t) = B_0 + b(x,y,z,t) + \varphi(x,y,z) \qquad \text{Eq. 2-16}$$

If the spins are mobile (i.e. through diffusion), these static inhomogeneities may be manifest as time-dependent field variations. Truly static contributions to dephasing can be recovered by the application of a 180° refocusing pulse; from Figure 2-7, it can be seen that a 180° rotation about either the x_ρ or y_ρ axis, will result in reversal of the phase dispersion. In contrast, time-dependent microscopic field inhomogeneities lead to irreversible signal loss. In practice, only the irreversible decay of M_{xy} is indicated by T_2 ; reversible decay is indicated by T_2' and all mechanisms of decay – both reversible and irreversible – are indicated by the relaxation time constant, T_2^* where

$$\frac{1}{T_2^*} = \frac{1}{T_2} + \frac{1}{T_2'} \qquad \text{Eq. 2-17}$$

Because T_2 relaxation is governed not only by the same time-dependent dipole fluctuations responsible for T_1 relaxation but also static variations in the local field strength, T_2 relaxation typically occurs more quickly than does T_1 relaxation. That is, $T_2 < T_1$.

The potential for image contrast inherent in tissue T_2 values comes from the fact that the signal amplitude will decay more quickly for some species than for others. This is illustrated in Figure 2-8 for two tissues with different T_2 values (where $T_{2a}<T_{2b}$). The oscillating transverse magnetization vector, M_{xy}, is shown for tissue *a* (solid blue line) along with its decay envelope (dashed blue line). Tissue *b*, with its shorter T_2 value decays more slowly and, hence, would appear more brightly on an image.

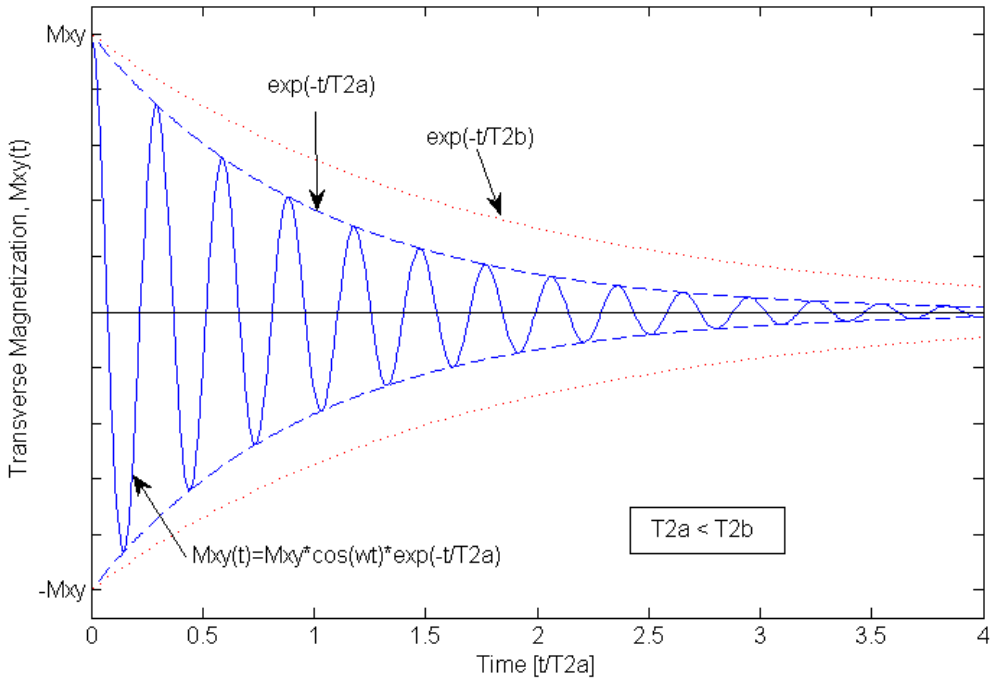

Figure 2-8

T_2 relaxation and transverse magnetization decay. Two tissues – *a* and *b* – have different spin-spin relaxation constants where $T_{2a}<T_{2b}$. The oscillating transverse magnetization signal is given for tissue *a* (solid blue line) along with its decay envelope (dashed blue line) as determined by its inherent T_2 value. For tissue *b*, only the decay envelope is illustrated (red dotted line).

2.1.3.3.Exogenous contrast agents

In addition to the vast potential for image contrast stemming from intrinsic differences in T_1 and T_2 relaxation, there are a number of exogenous agents which

can be used to further enhance image contrast. Exogenous contrast agents, such as gadolinium, manganese, and superparamagnetic iron oxide (SPIO), can be intravenously injected and introduced to specific targeted tissues where they act to modify the T_1, T_2 and T_2* characteristics and improve tissue contrast.

2.1.4. Basics of Imaging: from NMR to MRI

In §2.1.1, the NMR phenomenon was described as arising from the interaction of nuclear spins with two magnetic fields - B_0 and $B_1(t)$. NMR, a spatially indiscriminate technique, can be extended to provide powerful spatial information by allowing the spins to interact with a third type of magnetic field – one whose strength varies linearly with position. We shall discuss the 3D localization of the signal in 3 steps: slice selection, frequency encoding, and phase encoding.

2.1.4.1.Slice Selection

As previously discussed, excitation of the sample is achieved by introducing the spins to a tuned RF pulse which tips the spins into the transverse plane. If, before applying the RF excitation, a linearly varying magnetic field is applied, the resonant frequency of the spins becomes dependent upon their position within the gradient field and only those spins whose resonance frequency matches that of the RF pulse will be affected. The linearly varying magnetic field and frequency spread are given in Eq. 2-18 below.

$$B = B_0 + B_z = B_0 + G_z \cdot z$$
$$\omega(z) = \gamma \cdot (B_0 + G_z \cdot z) \qquad \text{Eq. 2-18}$$

A slice of spins at position z_0 with slice width Δz can be excited by applying a modulated RF pulse with a bandwidth of $\Delta\omega = \gamma G_z \Delta z$ and a central frequency matched to that of the spins at z_0. This is known as selective excitation and is illustrated in Figure 2-9.

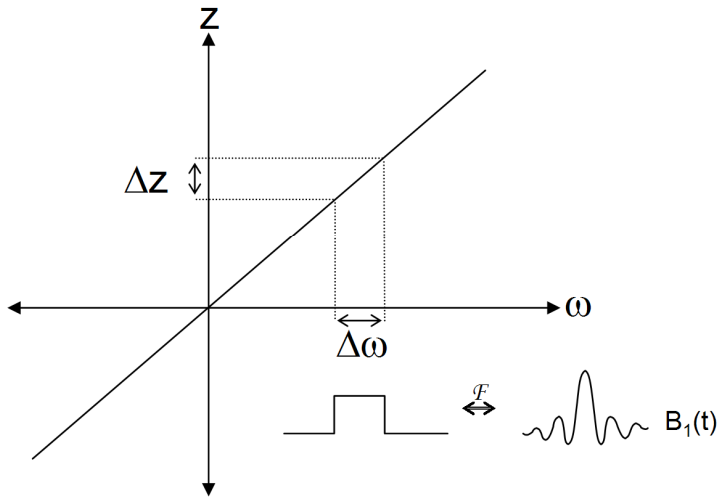

Figure 2-9

A slice of width Δz can be selectively excited in the presence of a linearly varying magnetic field gradient, G_z. The bandwidth of the pulse is $\Delta\omega = \gamma G_z \Delta z$. To select a rectangular slice profile, a sinc pulse is ideally required.

By exciting only spins within a slice of finite width, Δz, the remaining problem of spatial localization is reduced to a 2D problem. The second and third dimensions of spatial localization are discussed next.

2.1.4.2.Frequency Encoding

Once a collection of spins within a finite slice of the object have been rotated into the transverse plane and the slice selection gradient has been turned off, the spins will precess about the main magnetic field according to Eq. 2-3. By introducing a second linearly varying magnetic field, i.e. one that is aligned with B_0 but varies in strength along the x direction, the precise frequency at which the spins precess about B_0 will vary according to their position along the x axis as in Eq. 2-19 below:

$$\omega(x) = \gamma(B_0 + G_x x) \qquad \text{Eq. 2-19}$$

The detected signal is then composed of many frequencies which can be separated and linked back to position of origin through Fourier analysis. This is schematically illustrated in Figure 2-10.

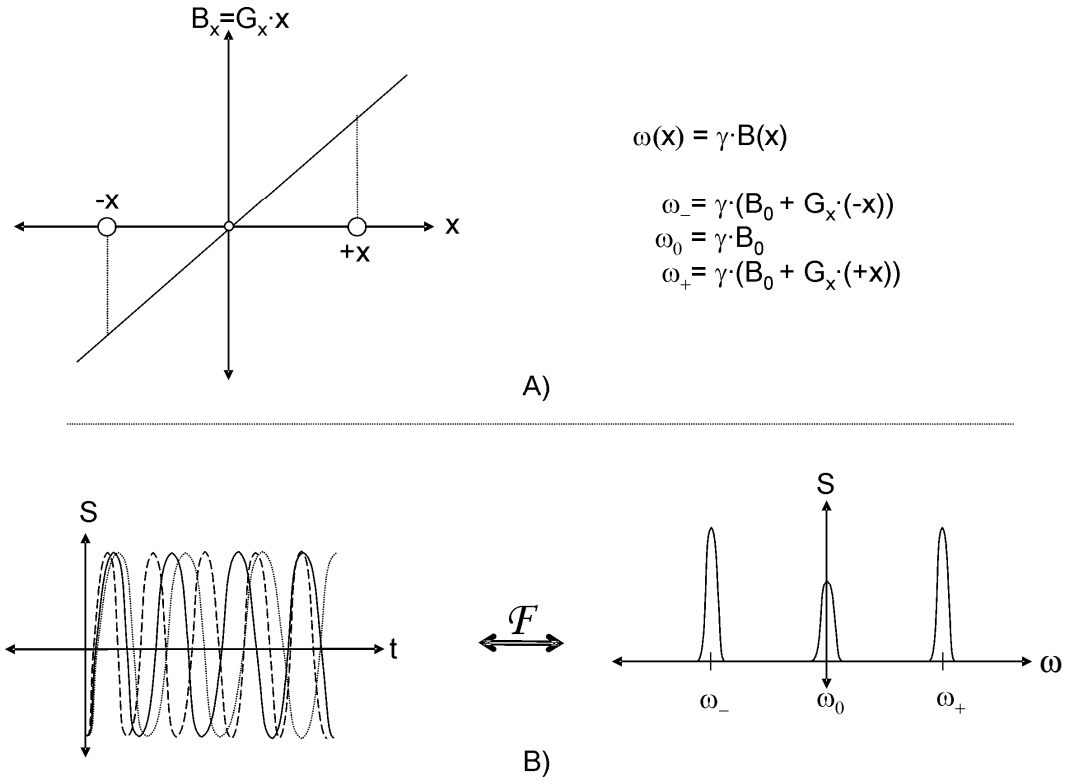

Figure 2-10

A) Three objects at positions *–x, 0, +x* are subject to a linearly-varying magnetic field gradient, G_x. Their position-dependent precessional frequencies are given by the equations at right. B) Sinusoidally varying signals from all three objects are simultaneously recorded in the time domain. Through Fourier analysis and knowledge of the function *ω(x),* the individual frequency components can be separated and linked back to their positions or origin. The amplitude, *S*, of the peaks indicates the relative intensities of the imaged objects – i.e. two objects of equal intensity at ± *x*, and one of lesser intensity at *x=0*.

Under the influence of the frequency encoding gradient, G_x, the analog time domain signal is composed of many frequencies which must be digitized during the data acquisition. If the extent of the object being imaged is the field of view, *FOV*, then the maximum range of frequencies in the object signal in the presence of the frequency encoding gradient is

$$\Delta\omega = \gamma G_x FOV \qquad \text{Eq. 2-20}$$

Thus, the maximum frequency is $\Delta\omega/2$. Since the signal must be digitized at a rate of twice the maximum frequency in order to avoid aliasing, the sampling bandwidth, BW_{sam}, must satisfy the following condition:

$$BW_{sam} \geq \gamma G_x FOV \qquad \text{Eq. 2-21}$$

If a matrix size N_x is desired in the *x* direction, then the size of each pixel will be $\Delta x = FOV/N_x$. Thus Eq. 2-21 can be rewritten as

$$BW_{sam} \geq \gamma G_x N_x \Delta x \qquad \text{Eq. 2-22}$$

2.1.4.3.Phase Encoding

Phase encoding is used to embed information about the second orthogonal direction within the selectively excited slice. The idea is similar to that of both slice selection and frequency encoding, except this time a linearly varying magnetic field is applied (i.e. along the *y*-axis) for a fixed length of time *after* the slice selection gradient but *before* the frequency encoding gradient and the signal acquisition. Thus, a fixed amount of phase is accumulated by the spins – based

upon their position along the *y*-axis – before their frequency is altered based on their position along the *x*-axis. After the application of a phase encoding gradient for time τ in the *y*-direction, the position-dependent phase can be written as

$$\phi(y) = \gamma \cdot (B_0 + G_y \cdot y) \cdot \tau \qquad \text{Eq. 2-23}$$

Figure 2-11 illustrates how the magnetic field gradient provides spins with different amounts of phase according to their position along the *y*-axis.

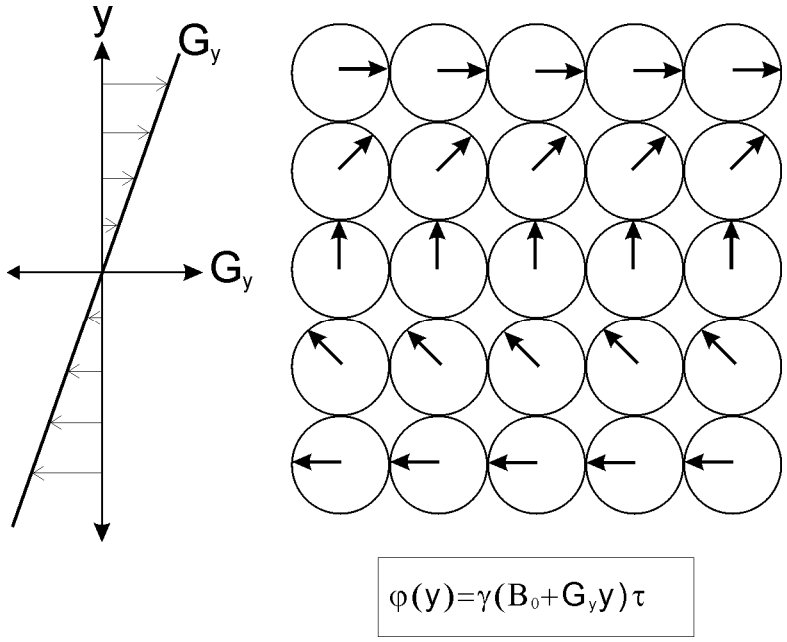

Figure 2-11

Phase Encoding: a magnetic field aligned with B_0 (*z* direction), whose strength varies with position, *y*, is applied for a fixed amount of time, τ. The phase of the transverse magnetization thus encodes for spatial position along the *y*-axis.

In the phase encoding direction, only a single phase encode can be performed before each signal acquisition. Thus, if a matrix size $N_x \times N_y$ is desired, the sequence of RF excitation, phase encode, and signal acquisition must be repeated N_y times with the phase encode gradient strength incremented each time, in linear steps of size ΔG_y. Just as Eq. 2-21 describes the conditions required to avoid aliasing in the frequency encode direction, a similar constraint must be imposed in order to avoid aliasing in the phase encode direction. Again, adjacent samples must have a phase difference of less than π - however, unlike in frequency encoding where the samples are taken at time intervals $\Delta t = 1/BW_{sam}$, adjacent samples in the phase encoding direction are separated by the repetition time and with gradient intervals, ΔG_y. Increments in the phase encode gradient, ΔG_y, are thus given as:

$$\Delta G_y = \frac{1}{\gamma FOV \tau} \qquad \text{Eq. 2-24}$$

2.1.4.4. 3D Imaging

A 3D object can be imaged using either '3D imaging' or 'multi-slice 2D imaging'. The preceding discussion dealt with spatial localization techniques used for multi-slice 2D Fourier Transform (FT) imaging, i.e. slice selection followed by phase and frequency encoding in the 2 orthogonal directions within the slice. The two approaches differ in the way in which RF excitation is carried out. In 2D or multi-slice imaging, a series of RF pulses in conjunction with a

slice select gradient are used to define a series of 2D slices along the third dimension. In 3D imaging, an RF pulse is typically used to excite a much thicker slice which is then partitioned into smaller slices using phase encoding (routinely referred to as 'partition encoding' for this application). In multi-slice 2D imaging, it is often possible to interleave acquisitions (i.e. excite several slices within a single *TR*) in order to speed up the imaging time. This is not possible in 3DFT imaging since the entire volume is excited at once and N_z (number of slices) phase encodes must be carried out for partition encoding. 3DFT imaging is thus slower than multi-slice imaging, especially when long *TR*s are used. Nevertheless, it may be an attractive option when thin, high signal to noise ratio (SNR) slices are desired and/or when it is desirable to avoid distortions due to field inhomogeneities in the slice select direction (see § 2.2.3.2). Finally, if compared to multi-slice 2DFT imaging with short *TR* (i.e. when slice interleaving is not possible), 3DFT imaging may offer no penalties in terms of increased acquisition time.

2.1.5. Imaging Sequences

As discussed, the MR image is formed from an RF signal emitted by the object; through application of appropriate gradient fields, the signal can be made to contain information about the spatial distribution of the nuclear magnetization within the object. Moreover, by choosing the particular times at which the spins are excited and their FID signals are subsequently digitized, the signal can be made to contain information about the spin density, or their T_1 , T_2, or combined

relaxation constants. Two important sequence timing parameters to consider are the repetition time, *TR*, and the echo time, *TE*. In terms of encoding the resultant signal there are an infinite number of ways to do so. Each encoding scheme has both advantages and disadvantages in terms of the quality and characteristics of the image formed, the time required to play out the encoding scheme, the procedures used to sample and decode the signal, and as we will later explore, the types of geometric distortions that may result. A few of the most common information encoding schemes will be explored next.

2.1.5.1. k-*space and the signal equation*

As the magnetization vector rotates in the transverse plane following excitation, it creates a time domain FID signal in the receiver coil via Faraday's Law of Induction. This signal can be expressed as

$$S(t) = \int_V e^{-t/T_2^*} \cdot \rho(\vec{r}) \cdot e^{-i2\pi\gamma \int_0^t B(\vec{r},t')dt'} d\vec{r} \qquad \text{Eq. 2-25}$$

where $\rho(\vec{r})$ is the spin density and $B(\vec{r},t) = B_0 + G(\vec{r},t) \cdot \vec{r}$. Considering the equation in the rotating frame, then $B(\vec{r},t) = G(\vec{r},t) \cdot \vec{r}$, which represents only the spatial encoding magnetic gradient fields.

Collecting this signal, *S(t)*, can be thought of as sampling the object distribution in the Fourier spatial frequency domain. The application of the gradient fields is controlled by the sequence parameters and the way in which they are played out

determines the points in the spatial frequency domain that are sampled. With this in mind, Eq. 2-25 can be re-written as

$$S(t) = \int_V e^{-t/T_2^*} \cdot \rho(\vec{r}) e^{-i2\pi\gamma \cdot \vec{k}(t) \cdot \vec{r}} d\vec{r} \qquad \text{Eq. 2-26}$$

where

$$\vec{k}(t) = \gamma \int_0^t G(t')dt' \qquad \text{Eq. 2-27}$$

$\vec{k}(t)$ can be thought of both as the integral of the gradients (the gradient 'history') and as the vector of the spatial frequency coordinate, and the term "*k* -space" will refer to the conjugate of "*r*-space". Thus Eq. 2-25 can be rewritten once again, this time as

$$S(t) = e^{-t/T_2^*} \ \Im(\vec{k}(t)) \qquad \text{Eq. 2-28}$$

where $\Im(\vec{k}(t))$ is the Fourier Transform of the spin density spatial distribution, $\rho(\vec{r})$. The FID signal can be encoded by sampling across the *k*-space, where the particular trajectory through *k*-space is determined based on how the time-varying gradient fields are applied. When we consider how an image is acquired, we are mainly concerned with the way in which *k*-space is sampled. The following discussion will focus on three ways to create the time-domain signal, *S(t),* and sample it in *k*-space.

2.1.5.2.Gradient Echo Imaging

A Gradient Echo (GE) image is generated by using a magnetic field gradient to first dephase the transverse magnetization vector and then to rephrase the vector into a "gradient echo" by reversing the gradient field polarity. The maximum signal amplitude (or "echo") occurs when the net gradient area is nulled; this is taken to be the echo time, *TE*. In its simplest form, a gradient echo image is produced by using a single RF excitation for each line of *k*-space traversed; a typical pulse sequence diagram is shown in Figure 2-12. A slice selection gradient is applied along with an RF pulse to tip the spins into the transverse plane; further spatial localization is achieved by first encoding for phase and then for frequency. Maximum signal amplitude coincides with the center of the positive FE gradient. After the repetition time, *TR*, the entire pulse sequence is repeated, but this time with the PE gradient strength incremented. Although the signal dephasing induced by the gradients is reversed when the gradient polarity is reversed, loss of signal coherence due to local field inhomogeneities is not reversed; thus GE images show a rapid decrease in signal amplitude as the echo time is increased. As a result, GE images are sensitive to differences in T_2* as opposed to differences in T_2. Lastly, in order to avoid acquiring signal from stimulated echoes, some form of spoiling is also typically employed to destroy any leftover transverse signal that may otherwise build up over successive RF excitations.

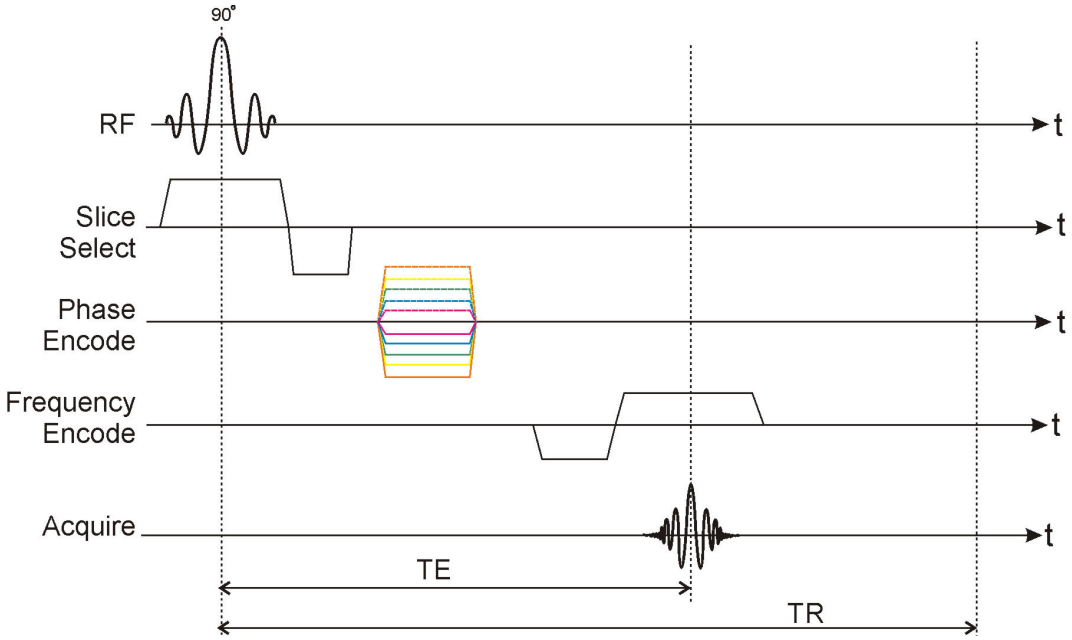

Figure 2-12

Gradient timing for a standard gradient echo image acquisition

The corresponding *k*-space diagram for the GE sequence is shown in Figure 2-13. The initial point in *k*-space is determined by the strength and duration of the phase and frequency encode gradients according to Eq. 2-27. Assuming that frequency and phase encoding take place in the *x* and *y* directions, respectively, the value of k_y is determined by the size of the PE lobe (the coloured lobes in Figure 2-12), and a single line along the k_x–axis is filled during the application of the frequency encode gradient; the point at which k_x=0 during the readout is taken to be t=TE. At a fixed time, TR, the slice is re-excited, the phase encode gradient is incremented and the process is repeated as a second line of *k*-space is filled.

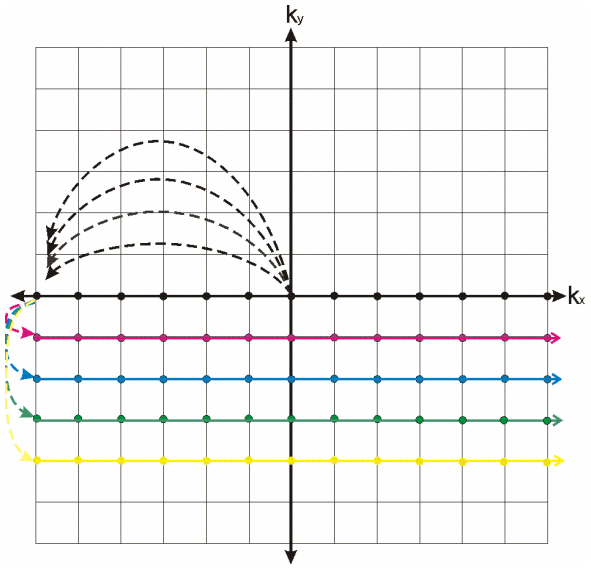

Figure 2-13

k-space traversal for a GE image acquisition. Assuming FE and PE occur in the *x* and *y* directions respectively, the value of $G_y\tau$ determines the position along the k_y axis and one line of *k*-space (along k_x) is acquired after each RF excitation.

2.1.5.3. Spin Echo Imaging

A spin echo (SE) image is acquired in much the same way as a GE image, with the exception that following the initial RF excitation pulse, a second 180° RF pulse is applied. The 180° pulse effectively reverses the positions of the "fast" and "slow" spins in the transverse plane, refocusing the spins into a so-called "spin echo" at the echo time, *TE* (see Figure 2-7). As with the GE sequence, loss of phase coherence begins after the initial RF pulse due to intrinsic and extrinsic inhomogeneities; however, the refocusing pulse at $t = TE/2$ allows one to recover the portion of the signal lost to static inhomogeneities (i.e. T_2' effects) at $t = TE$.

Thus, SE sequences are insensitive to static field inhomogeneities, but take longer to acquire than GE sequences due to the additional time required for the second RF pulse. A simple SE pulse sequence diagram is shown below in Figure 2-14; the traversal of *k*-space for a standard SE image is identical to that shown in Figure 2-13 for the GE image.

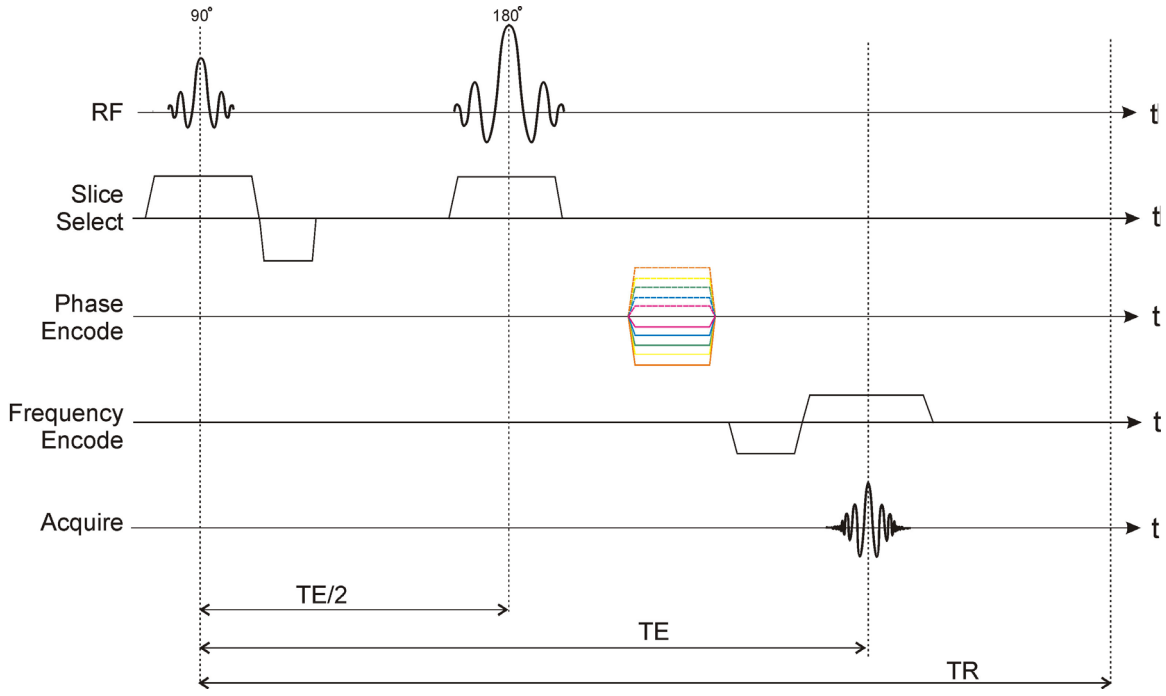

Figure 2-14

Pulse sequence timing for a typical spin echo image acquisition

2.1.5.4. Echo Planar Imaging

Echo Planar Imaging (EPI) provides a fast alternative to the imaging sequences previously presented. Such images are rapidly acquired following a single RF

excitation by alternating the polarity of the FE gradient, and incrementing the PE gradient using "blips" as shown in Figure 2-15. The corresponding *k*-space trajectory is illustrated in Figure 2-16; the direction of filling along k_x depends upon the polarity of the FE gradient and the steps between adjacent k_y values are accomplished with the triangular PE "blips". A 2D image slice can be acquired in as little as 40-100 ms, which reduces the effects of motion artefacts and allows monitoring of dynamic processes through rapid acquisition of successive images. EPI was first introduced by Mansfield in 1977[9], but could not be practically implemented until much more recently for a variety of hardware-related reasons. The EPI signal intensity will eventually decay to zero due to T_2* effects; thus effective acquisition of all points in *k*-space requires large field gradients that are very rapidly switched. It should be noted that a similar technique can be implemented using a train of spin echoes. In this case, the initial RF excitation is followed by a series of 180° refocusing pulses with a single signal acquisition centered at each successive spin echo. In the time between each 180° pulse and the signal acquisition, the phase encode gradient is applied.

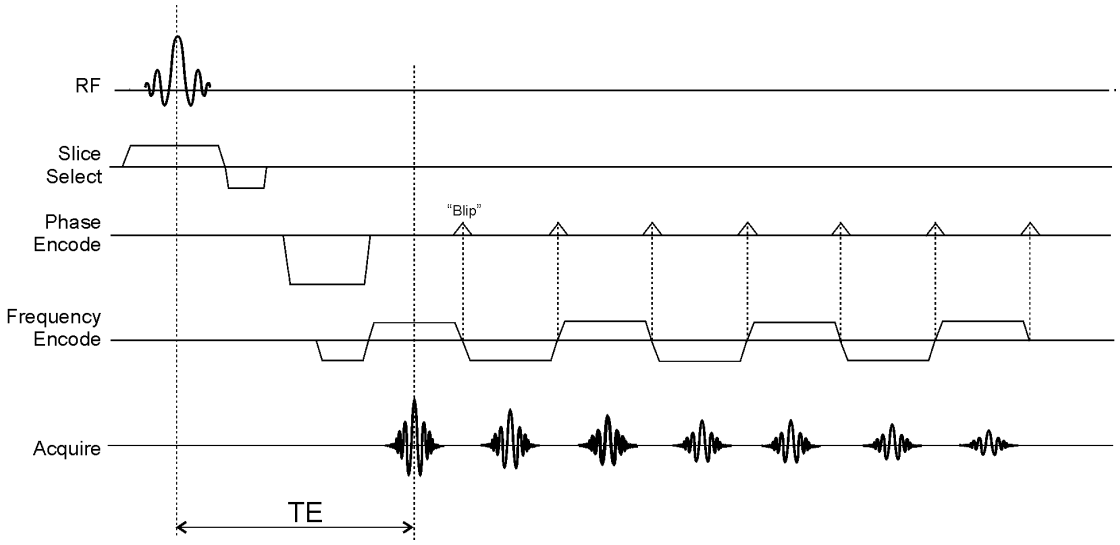

Figure 2-15

Pulse sequence diagram for single shot echo planar imaging

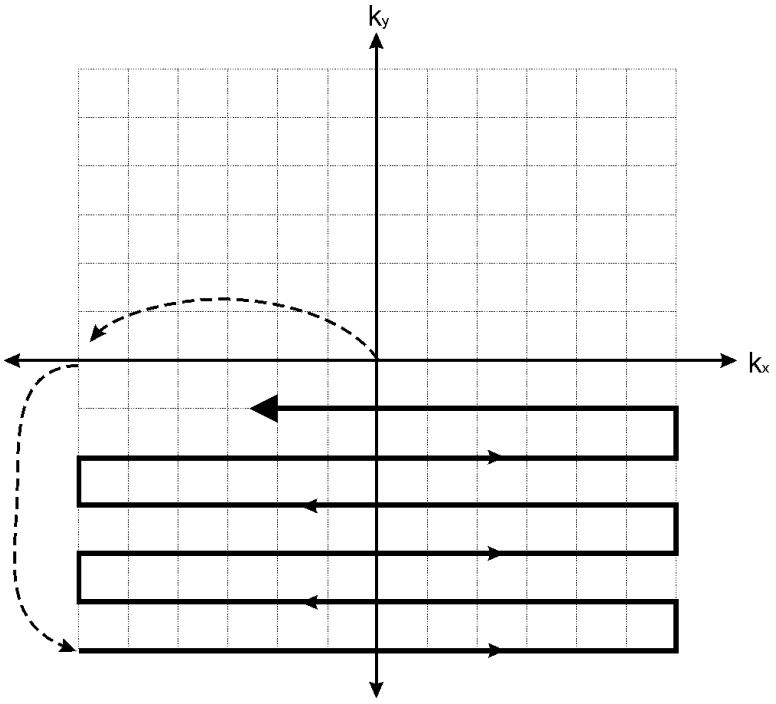

Figure 2-16

k-space trajectory for single-shot EPI

2.2. The distortion problem

At the heart of all NMR experiments is the Larmor equation, Eq. 2-3, which relates precessional frequency, ω_0, to magnetic field strength, B_0. As discussed in §2.1.4, the NMR signal can be spatially encoded by introducing a magnetic field gradient such that the precessional frequency of the spins is linearly related to their position along a certain axis. During image reconstruction, the known relationship between field strength and position is used to link the phase and frequency of the sampled FID signal to its position of origin. A problem arises,

however, when the assumed relationship between position, x, and frequency, ω, does not hold true; this results in misplaced signal and, hence, image distortion.

2.2.1. System distortions: gradient non-linearity and B_0 inhomogeneity

Gradient coils, inserted within the magnet's bore, generate linearly varying magnetic fields. Depending upon the precise patterning and orientation of the windings, the field can be made to vary in any of the three orthogonal directions. Unfortunately, it is not possible to construct a coil such that a single component of the field varies strictly linearly; there are always higher order field terms, which contribute to non-linearity.[11] In the presence of an ideal and linear gradient, G_x, a spin at position x_1 precesses at frequency ω_1, as shown in Figure 2-17. In the presence of a non-linear gradient, G_x', however, the actual precessional frequency is ω_1' which is associated with position x_1'. A difference exists in the assumed and actual relationship between position and frequency; thus the signal is misplaced from x_1 to x_1'.

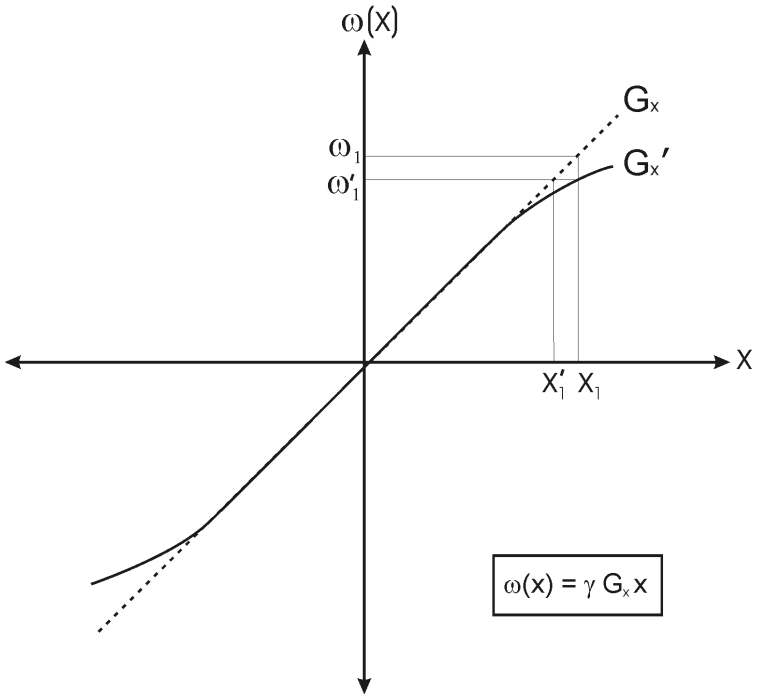

Figure 2-17

MR image formation is based on an assumed relationship between position and precessional frequency (or phase), i.e. $\omega = \omega(x)$, which is established through the presence of a magnetic field gradient G_x. Any deviations from the assumed relationship will result in signal being misplaced from x_1 to x_1'.

In addition to highly linear gradient fields, the presence of a homogeneous static magnetic field, B_0, is fundamentally important to the formation of geometrically accurate images. Unfortunately, the background polarizing field, B_0, cannot be made perfectly uniform over the volume of the bore due to design constraints, but it can be improved through both active and passive shimming. Passive shimming involves the insertion of small pieces of ferromagnetic metal around the magnet's bore, while active shimming is performed with shim coils inserted into the

magnet, which generate fields to oppose and cancel out residual magnetic field aberrations. The resultant field homogeneity, ΔB_0, is expressed in parts per million, or ppm, indicating the deviations in magnetic field strength relative to the mean value over a certain volume of interest. Just as a non-linear gradient results in spatial mispositioning due to deviations from the assumed relationship between position and precessional frequency, so too do inhomogeneities in the main field. A 10 ppm inhomogeneity translates to a 30 μT offset in field strength which (from Eq. 2-3) results in a frequency offset of 128 Hz. The resultant spatial offset, Δx, is given as

$$\Delta x = \frac{\Delta B}{G_{fe}} \qquad \text{Eq. 2-29}$$

where G_{fe} is the frequency encoding gradient strength. In the presence of such an inhomogeneity, signal would be misplaced by *3 mm*.

2.2.2. Object distortions: chemical shift

Just as imperfections in the equipment design can cause aberrations in the magnetic field uniformity (or linearity), so too can the object being imaged. Object related distortions include both chemical shift and magnetic susceptibility effects. The chemical shift effect arises because protons, depending on their local environment, experience small but measurable differences in magnetic shielding.

The chemical shift, σ, describes the response of the electronic environment to the external field and is defined as

$$B_{shifted}(i) = (1 - \sigma_i)B_0 \qquad \text{Eq. 2-30}$$

where *i* refers to the specific chemical compound. For example, protons bound in C-H chains (i.e. in adipose tissue) experience slightly different local magnetic fields than do protons originating in water-based tissues; they experience a chemical shift of 3.35 ppm,[11] which corresponds to a shift in Larmor frequency of 430 Hz at 3.0 T. Such a shift in Larmor frequency means that the assumed relationship between frequency and space, which is relied upon during image construction, does not hold true for signal originating in adipose tissue. This results in a constant offset of the fat-based signal with respect to the water-based signal along the frequency encoding direction as illustrated in Figure 2-18. Just as the resultant spatial mispositioning caused by inhomogeneities in the B_0 field is dependent upon the strength of the frequency encoding gradient strength (Eq. 2-29), so too is the spatial mispositioning caused by chemical shift. The localized field inhomogeneities due to chemical shift can be represented as ΔB_{CS}. Through appropriate selection of the gradient strength (i.e. by using high field gradients), the extent of the spatial distortion caused by chemical shift effects can be minimized.

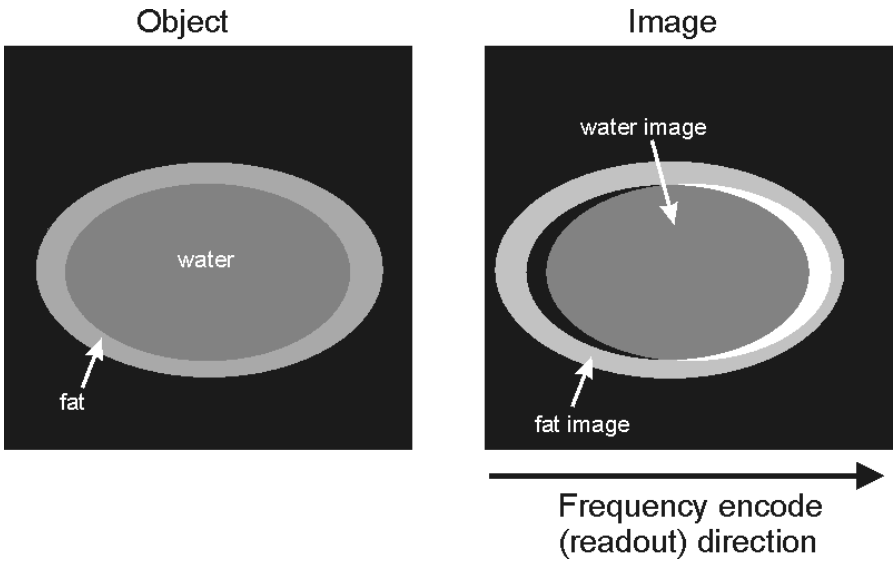

Figure 2-18

The signal from fat in adipose tissue is displaced along the frequency encode direction in an MR image due to chemical shift. At 3 T, the fat-water chemical shift results in a difference in resonance frequencies of 430 Hz. The spatial displacement caused by the chemical shift effect is dependent upon the strength of the frequency encoding gradient, (Eq. 2-29).

2.2.3. Object distortion: magnetic susceptibility

In a similar fashion, differences in tissue magnetic susceptibility can alter the local magnetic field and lead to distortions. The magnetic susceptibility, χ, of a material quantifies the strength of the magnetization, which results from an external magnetic field. While B is the symbol usually used to represent the magnetic field strength in MRI, it more precisely represents the so-called

magnetic flux density, while H and M represent the applied field strength and the material magnetization respectively. That is

$$B = \mu_0 (H + M) \qquad \text{Eq. 2-31}$$

where μ_0 is the permeability of free space. For materials whose magnetization depends linearly on the applied field, M is expressed as

$$M = \chi H \qquad \text{Eq. 2-32}$$

Although most MR-compatible substances have very small magnetic susceptibilities (i.e. $|\chi| \approx 10^{-5}$), the magnetic flux density, B, is altered by the presence and distribution of weakly magnetic tissues and materials. Paramagnetic substances increase the magnetic field while diamagnetic substances decrease the magnetic field. Most tissue in the body is primarily water and therefore has a magnetic susceptibility value close to $\chi_{water} = -9.04$ ppm, while air (i.e. in the nasal cavities) has $\chi_{air} = 0.36$ ppm. Table 2-1 lists the susceptibility values for a variety of MR-relevant materials.

Material	Susceptibility ($\times 10^6$)
Water (37 °C)	-9.05
Human tissues	~(-11.0 to -7.0)
Whole blood (deoxygenated)	-7.90
Red blood cell (deoxygenated)	-6.52
Air (NTP)	0.36
Titanium	182
Stainless steel	3520-6700
Iron	200,000

Table 2-1

Susceptibility values for common materials relevant to MRI.[12] All values are given as dimensionless SI volume susceptibilities.

Differences in material susceptibility lead to field inhomogeneities which can be represented as ΔB_χ. Unfortunately, such field inhomogeneities cannot easily be measured or predicted as they depend upon the position, size, shape, orientation and susceptibility of each component in the imaged object.[12] For an arbitrary distribution of magnetic material, numerical methods are generally required to determine the solution to a partial differential equation,[13,14] while analytic solutions can be calculated for very simple geometries. For example, Schenk gives the solution for the inhomogeneous magnetic field generated by a simple circular cylinder oriented in two different ways.[12] For a circular cylinder (radius a) whose axis is transverse to the background field, B_0, (i.e. cylindrical axis aligned along the y-direction), the field is given as

$$\Delta B_z = \frac{\Delta\chi B_0}{2} \quad (\textit{inside cylinder})$$
$$\Delta B_z = \frac{\Delta\chi B_0}{2}\frac{a^2(z^2-x^2)}{(x^2+z^2)^2} \quad (\textit{outside cylinder})$$
Eq. 2-33

where $\Delta\chi$ represents the susceptibility difference between the cylinder and the surrounding material and it is assumed that $|\chi|<<1$. For a cylinder parallel to B_0 (i.e. cylindrical axis aligned along the z-direction), the field is given as

$$\Delta B_z = \Delta\chi B_0 \quad (\textit{inside cylinder})$$
$$\Delta B_z = 0 \quad (\textit{outside cylinder})$$
Eq. 2-34

More complex susceptibility geometries require numerical solutions in order to determine the magnetic field inhomogeneities.[13,14] The magnetic field perturbations created by the presence of a water/air sample reminiscent of a body with an air-filled cavity (i.e. the rectum) were simulated according to the numerical methods outlined by Bhagwandien *et al.*[13,14] The results obtained when the body and cylindrical air cavity axis are parallel to B_0 are illustrated in Figure 2-19.

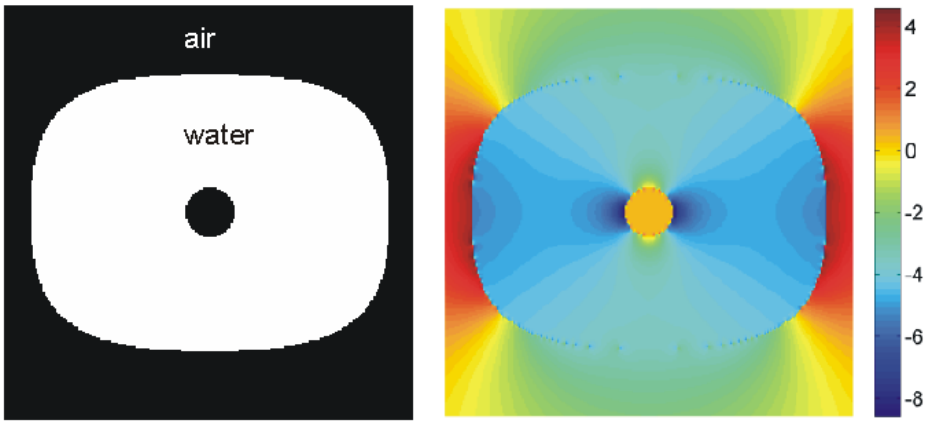

Figure 2-19

The air/water susceptibility distribution in A) results in a non-uniform magnetic field shown in B). Magnetic field inhomogeneities, ΔB_χ, are shown in parts per million. *Images courtesy of K. Wachowicz*.

As introduced in § 2.2.1, inhomogeneities in the polarizing field, ΔB_0, are machine-related field distortions which result in spatial distortions in the reconstructed image. Chemical shift and susceptibility effects are object-related sources of localized field inhomogeneities. The total field inhomogeneity at a given point in space, ΔB, is therefore made up of both machine- and object-related sources; it can therefore be expressed as

$$\Delta B = \Delta B_0 + \Delta B_{CS} + \Delta B_\chi \qquad \text{Eq. 2-35}$$

Geometric image distortion generated by hardware sources – gradient non-linearities and/or main field inhomogeneities – can be adequately investigated

using phantom methods. This type of study is detailed in Chapter 3. In contrast, however, distortions arising from the imaged object must be determined for each and every individual; phantom methods are therefore insufficient. Because object-specific sources of distortion, ΔB_{χ} and ΔB_{CS}, affect image distortion in the same way as does machine-related field inhomogeneity, ΔB_0, they can be easily measured together; thus image distortion due to gradient non-linearity can be derived from phantom experiments while the combination of machine and object related field distortions can be measured together using alternative methods. This type of study is the subject of Chapter 4.

2.2.4. The effect of magnetic field distortions on imaging

2.2.4.1. General Formulation of the Distortion Problem

In the absence of relaxation and inhomogeneities, the time domain signal given in Eq. 2-25 can be re-written for a 1D object in the rotating frame as:

$$\begin{aligned} S(t) &= \int \rho(x) e^{-i2\pi\gamma G_x x t} dx \\ S(k) &= \int \rho(x) e^{-i2\pi k_x x} dx \end{aligned} \qquad \text{Eq. 2-36}$$

where k, the spatial frequency, is the conjugate variable of x and is defined as

$$k = \gamma \int_0^t G(t) \cdot dt \,. \qquad \text{Eq. 2-37}$$

Considering the presence of both local magnetic field inhomogeneities, ΔB (due to static field inhomogeneities, as well as susceptibility and chemical shift effects) in addition to gradient non-linearities, dG_x, Eq. 2-36 becomes:

$$S(t) = \int \rho(x) e^{-i2\pi\gamma[(G_x + dG_x)x + \Delta B(x)]t} dx$$
$$S(k) = \int \rho(x) e^{-i2\pi k_x x'} dx \qquad \text{Eq. 2-38}$$

where

$$x' = x + \frac{x \cdot dG_x}{G_x} + \frac{\Delta B(x)}{G_x} \qquad \text{Eq. 2-39}$$

This implies that in the presence of field distortions, the signal will be incorrectly assigned to the location x'. From Eq. 2-39, it is evident that distortions due to ΔB are dependent upon gradient strength while distortions due to gradient errors have been shown to be independent of gradient strength because dG_x scales with G_x.[15,16] Furthermore, the way in which the different types of distortion are manifest in MR images can be dependent upon the particular imaging sequence employed; this is discussed in the following subsection, § 2.2.3.2.

In general, in an MR image suffering from geometric distortion, the location of a given feature, r', is shifted from its true position, r, by an amount, Δr:

$$r' = r + \Delta r \qquad \text{Eq. 2-40}$$

and the amount of distortion is equal to the ratio of the magnetic field perturbation, ΔB, to the gradient strength, G. That is:

$$\Delta r = \frac{\Delta B}{G}. \qquad \text{Eq. 2-41}$$

2.2.4.2. The effect of imaging parameters on distortion

Gradient non-linearities will result in image distortion along the gradient direction while ΔB distortions may affect one or all directions depending on the way in which the image is collected. For example, in a slice selected image with frequency and phase encoding gradients, G_x and G_y, and field inhomogeneities, ΔB, the received signal for a voxel can be expressed as

$$S(t) = \int \rho(x,y,z) \exp\left\{ i2\pi\gamma \left[\int_0^t G_x(t)xdt + \int_0^t G_y(t)ydt + \int_0^t \Delta B(x,y,z)dt \right] \right\} dxdydz$$

Eq. 2-42

As above, this expression implies that the phase of the detected signal is determined both by the gradient history and by the local field inhomogeneities. In a simple gradient echo experiment (see § 2.1.5.2), a line of *k*-space is traversed after each excitation as shown in Figure 2-13. Thus, the phase evolution between two adjacent points in *k*-space is given as

$$\begin{aligned} \Delta\phi_{kx} &= 2\pi\gamma\left[G_x \cdot x \cdot \Delta t + \Delta B(x,y,z) \cdot \Delta t\right] \\ \Delta\phi_{ky} &= 2\pi\gamma\left[\Delta G_y \cdot y \cdot \tau\right] \end{aligned} \qquad \text{Eq. 2-43}$$

where Δt is the sampling time interval, ΔG_y is the phase encode gradient step and τ is the duration of the phase encode gradient. Thus, phase evolution in the read encode direction is influenced by magnetic field inhomogeneities. Because

phase encoding in the *y*-direction is always performed at the same time following the excitation pulse, phase evolution in the *y*-direction is not affected by inhomogeneities.

Alternatively, in an EPI experiment (§ 2.1.5.4) where all of *k*-space is traversed after a single excitation (Figure 2-16), adjacent points in the k_y direction become separated in time by the length of time required to complete one full scan along the k_x direction. The phase evolution between adjacent points in k_y-space is given as

$$\Delta\phi_{ky} = 2\pi\gamma\left[G_y\, y\, \tau + \Delta B(x,y,z)\cdot(2t_{ramp} + N\Delta t)\right] \qquad \text{Eq. 2-44}$$

where t_{ramp} is the ramp time of the switched gradients, and N is the number of sampled points in the frequency encode direction.[17] For an EPI image, the distortion in the phase encode direction can be quite substantial due to the time over which ΔB distortions may evolve. The phase evolution in the frequency encode or k_x direction remains as it was in the gradient echo example. Thus both image directions are affected by ΔB distortions; however, distortion is significantly greater in the phase encode direction.

2.3. Correcting image distortions

The advantages and disadvantages of using MR in RTP were introduced in §1.3.1.2 and the sources of errors regarding MR geometric accuracy were explored in greater depth in §2.2. Image distortion has long been an issue in MRI

and has therefore been an active area of research for several decades. Most methods of distortion correction fall into one of three categories: (1) distortion avoidance (through phase encode imaging); and (2) indirect or (3) direct field mapping, followed by image correction. A summary of the variety of methods for coping with MR image distortion follows.

As discussed above in §2.2.3.2, and as shown by Chang and Fitzpatrick[18] and by Jezzard and Balaban[17], field inhomogeneities (i.e. B_0 inhomogeneities, χ and chemical shift effects) cause image distortions in the FE direction in standard spin-warp imaging, but not in the PE direction. Therefore, imaging methods which rely only on phase encoding have been proposed as a way to avoid the problem of inhomogeneity-related image distortion. Unfortunately, such methods must sacrifice the rapid data collection inherent in frequency encoding in favour of distortion-insensitive phase encoding; they are therefore prohibitively slow for clinical implementation. Along these lines, Bendel *et al* suggested echo projection imaging which uses an EPI-like sequence in conjunction with a series of 180° refocusing pulses[19]. However, instead of acquiring signal throughout the duration of the readout gradient, only a single data point is collected each time the phase dispersion due to extrinsic inhomogeneities is refocused and a spin echo is formed. By repeatedly switching the readout gradient in between successive 180° pulses, many spin echoes are generated and many points in *k*-space can be collected. The direction of the readout gradient is then varied and the process is repeated in order to create a projection image free of field inhomogeneity related

distortions. Similar techniques, which rely on a series of 180° refocusing pulses played out in conjunction with alternating gradients, were proposed by Miller and Garroway[18] and by Wong and Rosenfeld[20,21]; these methods are termed refocused gradient imaging and spin inversion imaging, respectively. Unfortunately, these techniques are slow, are limited by high levels of RF energy deposition to the patient, and the resulting images still require correction for distortions due to gradient non-linearities.

In 1985, O'Donnell and Edelstein[22] demonstrated the relative insensitivity of spin-warp (i.e. SE) imaging to field inhomogeneities as compared to projection imaging[22]. Although they did not explore methods for determining the underlying distortion field, they demonstrated the mathematics necessary for correcting both geometric and intensity distortions caused by inhomogeneous fields. Building on the work of O'Donnell and Edelstein[22], Schad[23,24] investigated ways to indirectly measure the field maps through distorted phantom images and to implement the previously presented distortion corrections. For example, by using a phantom containing a regular grid of water-filled, signal-producing tubes, the positions of the tubes can be measured in the distorted image and compared to their *a-priori* known locations. By evaluating the distribution of grid points at a certain slice position, a correction polynomial can be calculated which may be used to correct images for geometric distortion. The calculation of high order (usually third or fourth order) polynomial expressions for field distortion based on grid images has been shown to provide excellent correction of phantom images by several

groups.[23-27] Such methods account for all types of distortion – gradient non-linearity as well as field inhomogeneities.

A second method of indirectly measuring field inhomogeneities involves the acquisition of two images which differ due to either the exchange of the FE and PE directions[28] or the strength of the FE gradient.[29] Because field inhomogeneities cause distortions only in the FE encode direction, and because such distortions are apparent in opposite directions under FE gradient reversal, these methods allow distortions due to inhomogeneities to be determined by comparing the locations of discrete image points (i.e. phantom grid points) in the two images. Provided the true locations of the phantom points are also known, both the gradient non-linearities and the field inhomogeneities can be calculated. Kawanaka *et al* measured the 2D displacement of phantom grid points in order to establish third order polynomial expressions for the distortions due to inhomogeneities and gradient non-linearities. Yamamoto and Kohno used a similar approach in which they acquired two images with the same FE and PE directions, but altered the strength of the FE gradient in the two images.[29] A variation of this method is to use the same FE gradient strength for both images, but reverse the polarity. The so-called reverse gradient method has been used by several groups to measure and correct distortions caused by both gradient non-linearities and field inhomogeneities in phantom images.[16,30,31] This method is discussed in greater detail in Chapter 3.

Unfortunately, the previously discussed methods for indirectly measuring the field distortion map are based on phantom images and require identification of discrete points in both images. Corrections for gradient non-linearities can be applied to any image acquired on the system, but since field inhomogeneity maps include object-dependent susceptibility (and chemical shift) contributions, they cannot, in general, be applied to images of other objects. Furthermore, the calculated field maps cannot be used to correct in-vivo images since any two objects will generate distinctly different patterns of field inhomogeneities. In 1992, Chang and Fitzpatrick[18] extensively investigated the reverse gradient method and proposed a solution to the previous limitation of the method that required the use of phantom images. In order to implement the technique on continuous images (i.e. those without multiple obvious corresponding image grid points), it is necessary to find a set of boundary points on each image and then solve a differential equation relating the intensity profiles of each of the two images. Chang and Fitzpatrick illustrated the technique on phantom images, but did not rely on identifying matching grid points. More recently, the technique has been implemented on in-vivo images by other groups;[30,32,33] nevertheless, the method is limited by the assumption that the combined effects of gradient non-linearities and field inhomogeneities result in a one-to-one distortion field.

A third way to cope with field inhomogeneities is to directly measure the field distortions. In 1985, Sekihara[34] created a field map using a modified spin echo sequence. By offsetting the acquisition of the spin echo relative to the time delay

between the 90° and 180° RF pulses, the phase of the acquired image was made sensitive to underlying field inhomogeneities. Wendt[35] and Willcott[36] proposed sequences using two and three 90° excitation pulses, respectively, such that prior to image encoding, the spin phases are distributed according to their resonant frequencies. Accordingly, the signal amplitude in each voxel of the resulting image is modulated by the local value of the magnetic field inhomogeneities. Each of these techniques was used to generate field maps based on images of uniform phantoms. In 1991, Schneider and Glover[37] introduced an interleaved gradient echo technique which acquired two gradient echoes per phase encode in order to calculate field maps from the difference in phase evolution in the two images. The method was used to provide rapid feedback and guide adjustment of autoshimming procedures and was later adopted by Jezzard and Balaban[17] to correct image distortion due to B_0 and susceptibility effects in echo planar images.

Of the wide variety of methods proposed for measuring MR image distortion, most focus on measurement of the field inhomogeneities as opposed to gradient non-linearities. Nevertheless, full correction for image distortion must take into account both sources of geometric inaccuracy. It is therefore necessary to combine methods for measuring the specific field distortions caused by the imaged object (based on in-vivo images) through either direct or indirect field mapping with methods for measuring gradient non-linearity (based on images of grid phantoms).

Several phantom designs have been proposed for evaluating image distortion; the most basic design involves an array of parallel, water-filled tubes.[16,23,24,30] Unfortunately, such a design only allows distortion measurement in 2 dimensions since the control points are continuous along the *z*-axis; an additional phantom is therefore required to assess slice warping effects[24]. A 3D refinement to this design was introduced by Schubert *et al* in which a Perspex cube is precision-drilled with a system of orthogonal, intersecting, water-filled holes[26]. The intersection of the drillings defines a 3D array of points, but the resulting phantom is extremely heavy and the true positions of the grid points are difficult to determine (i.e. using CT) due to photon starvation caused by the large volume of attenuating Perspex. Other variations of grid phantoms include water-filled spheroids located along parallel Perspex tubes[25,38] or 3D rectangular plastic grids immersed in a water- or oil-filled phantom.[39-42] In each case, the position of the control points can be determined by calculating the object's center of gravity. Grid points must be kept as small as possible in order to achieve the best precision in grid localization.

Although gradient linearity is sometimes sacrificed for higher switching speeds and stronger gradient strengths, other improvements in hardware design have led to better static field homogeneity. This has limited the occurrence of gross image degradation due to field inhomogeneities and has, perhaps, reduced current interest in MR image distortion and correction. However, with the development of image guided radiotherapy and its stringent requirements for accurate and

precise imaging, geometric fidelity in MR imaging remains a pressing issue. In the radiotherapy-related literature, geometric distortion is most commonly cited as the primary limitation of MRI. Image distortion due to gradient non-linearity and field inhomogeneities must be investigated on a site-by-site basis and knowledge of the extent of image distortion must be quantified. Furthermore, the effect of MR image distortion on treatment planning outcomes must be evaluated in order to determine whether or not distortion is truly a limiting factor. If so, distortion measurement and correction methods may be developed and standard MR-based treatment planning protocols may then be created with confidence. The purpose of this thesis is to undertake a comprehensive study of MR image distortion on a 3T clinical scanner. Previous distortion characterization schemes are augmented with an improved phantom design (more and smaller control points for more detailed evaluation of the distortion field) and two distortion measurement techniques are combined in order to easily separate and individually quantify the various types of image distortion. In the event that multiple images are required for a given patient, the demonstrated distortion correction process is more streamlined and efficient than previous methods. Finally, the clinical impact of distortion correction was evaluated for an MR treatment planning study. Provided that dosimetric changes are insignificant, the somewhat labour intensive process of distortion evaluation and correction may be avoided. On the other hand, detailed knowledge of the way in which distortions affect clinical treatment planning images will enable either rapid distortion correction and/or tailoring of the PTV margins in order to account for systematic distortions.

2.4. References

[1] F. Bloch, "Nuclear Induction," Phys. Rev. **70,** 460-473 (1946).

[2] E. Purcell, "Resonance Absorption by Nuclear Magnetic Moments in a Solid," Phys Rev **69,** 37-38 (1946).

[3] N. Bloembergen, E. M. Purcell, and R. V. Pound, "Relaxation Effects in Nuclear Magnetic Resonance Absorption," Physical Review **73,** 679-712 (1948).

[4] R. Damadian, "Tumor detection by nuclear magnetic resonance," Science **171,** 1151-3 (1971).

[5] P. C. Lauterbur, "Image Formation by Induced Local Interactions: Examples Employing Nuclear Magnetic Resonance," Nature **242,** 190-191 (1973).

[6] R. Damadian, L. Minkoff, M. Goldsmith, M. Stanford, and J. Koutcher, "Tumor imaging in a live animal by field focusing NMR (FONAR)," Physiol. Chem. and Phys. **8,** 61-5 (1976).

[7] A. Kumar, D. Welti, and R. R. Ernst, "NMR Fourier Zeugmatography," J. Magn. Reson. **18,** 69-83 (1975).

[8] W. S. Hinshaw, "Image-formation by nuclear magnetic resonance - sensitive point method," J. Appl. Phys. **47,** 3709-3721 (1976).

[9] P. Mansfield, "Multi-planar image formation using NMR spin echoes," J. Phys. C: Solid State Phys. **10,** L55-L58 (1977).

[10] W. A. Edelstein, J. M. S. Hutchison, G. Johnson, and T. Redpath, "Spin warp NMR imaging and applications to human whole-body imaging," Phys Med Biol **25,** 751-756 (1980).

[11] E. M. Haacke, R. W. Brown, M. R. Thompson, and R. Venkatesan, *Magnetic resonance imaging: physical principles and sequence design* (Wiley-Liss, New York, 1999).

[12] J. F. Schenck, "The role of magnetic susceptibility in magnetic resonance imaging: MRI magnetic compatibility of the first and second kinds," Med Phys **23,** 815-850 (1996).

[13] R. Bhagwandien, M. A. Moerland, C. J. Bakker, R. Beersma, and J. J. Lagendijk, "Numerical analysis of the magnetic field for arbitrary magnetic susceptibility distributions in 3D," Magn Reson Imaging **12,** 101-7 (1994).

[14] R. Bhagwandien, R. van Ee, R. Beersma, and C. J. G. Bakker, "Numerical Analysis of the Magnetic Field for Arbitrary Magnetic Susceptibility Distributions in 2D," Magnetic Resonance Imaging **10,** 299-313 (1992).

[15] S. F. Tanner, D. J. Finnigan, V. S. Khoos, P. Mayles, D. P. Dearnaley, and M. O. Leach, "Radiotherapy planning of the pelvis using distortion corrected MR images: the removal of system distortions," Phys. Med. Biol **45,** 2117-2132 (2000).

[16] C. J. G. Bakker, M. A. Moerland, R. Bhagwandien, and R. Beersma, "Analysis of Machine-Dependent and Object-Induced Geometric Distortion in 2DFT MR Imaging," Magnetic Resonance Imaging **10,** 597-608 (1992).

[17] P. Jezzard and R. S. Balaban, "Correction for geometric distortion in echo planar images from B0 field variations," Magn Reson Med **34,** 65-73 (1995).

[18] H. Chang and J. M. Fitzpatrick, "A technique for accurate magnetic resonance imaging in the presence of field inhomogeneities," IEEE Trans Med Imaging **11,** 319-329 (1992).

[19] P. Bendel, "Echo projection imaging - A method to obtain NMR images undistorted by mangetic field inhomogeneities," IEEE Trans Med Imaging **MI-4,** 114-119 (1985).

[20] J. B. Miller and A. N. Garroway, "Removal of static field inhomogeneity and chemical-shift effects in NMR imaging," J. Magn. Reson. **67,** 575-579 (1986).

[21] T. S. Wong and D. Rosenfeld, "Spin-inversion imaging: A technique for NMR imaging under magnetic fields with high field nonuniformities," IEEE Trans Med Imaging **MI-6,** 148-156 (1987).

[22] M. O'Donnell and W. A. Edelstein, "NMR in the presence of magnetic field inhomogeneities and gradient field nonlinearities," Med Phys **12,** 20-26 (1985).

[23] L. Schad, S. Lott, F. Schmitt, V. Sturm, and W. J. Lorenz, "Geometrical distortions in MR-images and consequences for MR-stereotaxy," Proc. 5th SMRM, Montreal, P.Q., Canada**,** 1550-1551 (1986).

[24] L. Schad, S. Lott, F. Schmitt, V. Sturm, and W. J. Lorenz, "Correction of Spatial Distortion in MR Imaging: A prerequisite for accurate stereotaxy," J. Comp. Asst. Tomog. **11,** 499-505 (1987).

[25] M. Breeuwer, M. Holden, and W. Zylka, "Detection and correction of geometric distortion in 3D MR images," Proceedings of SPIE **4322,** 1110-1120 (2001).

[26] K. Schubert, F. Wenz, R. C. Krempien, O. Schramm, and G. Sroka-Perez, "Integration of an Open Magnetic Resonance Scanner in Therapy Simulation and Three-Dimensional Radiation Treatment Planning," Strahlenther Onkol **175,** 225-231 (1999).

[27] M. Holden, M. Breeuwer, K. McLeish, D. J. Hawkes, S. F. Keevil, and D. L. G. Hill, in *SPIE*; *Vol. 4322*, edited by M. Sonka and K. M. Hanson (2001).

[28] A. Kawanaka and M. Takagi, "Estimation of static magnetic field and gradient fields from NMR image," J. Phys. E.: Sci. Instrum. **19,** 871-875 (1986).

[29] E. Yamamoto and H. Kohno, in *Correction of distortions caused by field errors in MR imaging*, New York, 1987.

[30] S. J. Doran, E. M. Charles-Edwards, S. A. Reinsberg, and M. O. Leach, "A complete distortion correction for MR images: I. Gradient warp correction," Physics in Medicine and Biology **50,** 1343-1361 (2005).

[31] M. A. Moerland, R. Beersma, R. Bhagwandien, H. K. Wijrdeman, and C. J. G. Bakker, "Analysis and correction of geometric distortions in 1.5 T. magnetic resonance images for use in radiotherapy treatment planning," Phys Med Biol **40,** 1651-1664 (1995).

[32] A. S. Jackson, S. A. Reinsberg, S. A. Sohaib, E. M. Charles-Edwards, S. A. Mangar, C. P. South, M. O. Leach, and D. P. Dearnaley, "Distortion-corrected T2 weighted MRI: a novel approach to prostate radiotherapy planning," Br J Radiol **80,** 926-933 (2007).

[33] S. A. Reinsberg, S. J. Doran, E. M. Charles-Edwards, and M. O. Leach, "A complete distortion correction for MR images: II. Rectification of static-field inhomogeneities by similarity-based profile mapping," Physics in Medicine and Biology **50,** 2651-2661 (2005).

[34] K. Sekihara, S. Matsui, and H. Kohno, "NMR imaging for magnets with large inhomogeneities," IEEE Trans Med Imaging **MI-4,** 193-199 (1985).

[35] R. E. Wendt, III, M. R. Wilcott, III, W. Nitz, P. H. Murphy, and R. N. Bryan, "MR imaging of susceptibility-induced magnetic field inhomogeneities," Radiology **168,** 837-841 (1988).

[36] M. R. Willcott, III, G. L. Mee, and J. P. Chesick, "Magnetic Field Mapping in NMR Imaging," Magn Reson Imaging **5,** 301-306 (1987).

[37] E. A. Schneider and G. Glover, "Rapid In Vivo Proton Shimming," Magn Reson Med **18,** 335-347 (1991).

[38] M. Breeuwer, W. Zylka, J. Wadley, and A. Falk, in *CARS* (Paris, France, 1999).

[39] L. N. Baldwin, K. Wachowicz, S. D. Thomas, R. Rivest, and B. G. Fallone, "Characterization, predication, and correction of geometric distortion in 3T MR images," Med Phys **34,** 388-399 (2007).

[40] D. Wang and D. M. Doddrell, "A proposed scheme for comprehensive characterization of the measured geometric distortion in magnetic resonance imaging using a three-dimensional phantom," Medical Physics **31,** 2212-2218 (2004).

[41] D. Wang, D. M. Doddrell, and G. Cowin, "A novel phantom and method for comprehensive 3-dimensional measurement and correction of geometric distortion in magnetic resonance imaging," Magnetic Resonance Imaging **22,** 529-542 (2004).

[42] D. Wang, W. Strugnell, G. Cowin, D. M. Doddrell, and R. Slaughter, "Geometric Distortion in clinical MRI systems Part I: evaluation using a 3D phantom," Magnetic Resonance Imaging **22,** 1211-1221 (2004).

3. Chapter 3: A phantom-based MR distortion characterisation scheme

3.1. Introduction

Magnetic Resonance Imaging (MRI) is an extremely powerful diagnostic tool because of its excellent soft-tissue characterization. One of its many applications includes radiotherapy treatment planning (RTP) for cancer, where successful treatment outcomes rely on accurate localization of both tumour and surrounding structures. Delineation of soft-tissue tumours has been shown to be much easier when performed on MR than on CT.[1-6] Specifically, brain tumour gross tumour volumes (GTVs) have been shown to be significantly (up to 75%) larger when defined on MR than when defined on CT.[1,5,6] Thus, reliance on CT-defined tumour volumes could lead to significant under-dosing. In contrast, MR-delineated prostate volumes have been shown to be smaller than CT-delineated volumes,[7,8] while nearby critical structures have been shown to be more easily contoured and therefore better spared during treatment. Both prostate and brain studies have shown that MRI-based tumour volumes agree better with composite MR/CT volumes, show reduced interobserver variability, and are more accurate.[2-4,7-9] As sophisticated conformal treatments capable of delivering sharp dose gradients around target volumes become more commonplace, accurate tumor localization becomes paramount. Unfortunately, the direct use of MR for radiotherapy treatment planning is hampered by intrinsic image distortion that prevents the accurate geometric representation of anatomical structures. The work presented in this chapter is motivated

by our interest in developing geometrically accurate and precise MR images for use in MR-based radiotherapy treatment planning.

Geometric accuracy in MRI is limited by the homogeneity of the background field, the linearity of the applied gradients, the magnetic susceptibility of the imaged tissues, and chemical shift artifacts. Reconstruction of the MR image relies on the assumption that both a perfectly uniform background field and linearly varying gradient fields are present. It may be difficult to achieve this, however, due to a number of design features. Short, wide-bore systems are often preferred as they improve the patient 'friendliness' of the magnet, but such designs will inevitably compromise B_0 homogeneity. In addition, fast, high-performance gradients – especially those employing short coils – often suffer from increased gradient non-linearity.[10] Differences in the assumed and true magnetic field experienced at each point within the magnet's bore lead to distortions in the images generated. The magnitude and direction of geometric distortion varies for each type of imaging protocol and distortions of up to 25 mm over a 24 cm field of view have been reported for 1.5 T magnets.[10-13] While geometric errors of several millimeters may not be problematic for routine diagnostic purposes, an accuracy of 1-2 millimetres is required for radiation therapy purposes.[11,12,14-16]

Currently, there is a push towards using higher field magnets for both imaging and spectroscopic purposes. With respect to spectroscopy, an increase in the magnetic field strength increases the sensitivity and resolution of the spectra produced.[17] Cancer centers will therefore be more likely to invest in 3 T systems for clinical use as interest in

biological target definition increases. Furthermore, the signal-to-noise ratio (SNR) increases linearly with B_0 field strength.[18,19] Therefore, higher field systems can be employed to increase image SNR, or alternatively, the SNR can be left unaltered in exchange for reduced scanning time; this may be particularly advantageous for severely ill patients for whom prolonged immobility is difficult to impossible. However, distortions due to B_0 shimming and patient-related effects are also proportional to B_0 field strength and thus comprehensive knowledge of geometric distortions at higher magnetic fields becomes even more important. In order to reduce the effects of B_0 distortions, it is often suggested to use the highest read gradient possible[14,20]; however, this increases the bandwidth per pixel and reduces the signal readout time, effectively decreasing the SNR and lessening one of the primary benefits of high field imaging. Clearly, there are both advantages and disadvantages to imaging at higher field strengths. Provided image distortions at 3T are not too large as to be reliably detected and corrected, such images may find greater use in the radiotherapy treatment planning process.

Routine practice for radiotherapy treatment planning applications includes fusion of both MR and CT data sets. This combines the spatial accuracy of CT with the soft-tissue contrast of MR, overcoming not only the problem of inherent MR image distortion but also the lack of electron density information. However, reliance on image fusion involves inherent errors and registration based on the locations of external landmarks placed on the skin[21] will be particularly prone to distortions which generally increase with distance from isocenter.[20] Even registration based on the locations of bony landmarks (which are both more rigid and less prone to distortion errors because of their

greater proximity to isocenter than surface landmarks) may involve significant distortion-related errors when MR images are acquired on magnets with poor field homogeneity or gradient non-linearity. Provided adequate distortion correction can be achieved, the reliability of MR/CT image fusion could be greatly improved. Alternatively, with additional provisions for image intensity correction, bulk tissue electron densities may be assigned to segmented MR images allowing for treatments to be planned on MR images without fusion to CT data.[20,22]

Characterisation of system-related distortions forms the basis of any distortion correction scheme. Such distortions are inherent to the scanner, can be measured using phantom techniques, and corrections can be applied to all images, regardless of the subject. A variety of phantom designs and distortion characterisation schemes were briefly discussed in §2.3. Breeuwer *et al* used an array of 61 rods (6 mm in diameter) with periodically spaced spheres (14 mm in diameter) to evaluate 3D distortion in MRI.[11,23,24] After measuring the positions of phantom objects to obtain an estimation of the distortion transformation, a polynomial function was fit to the data. However, total image distortion represents not only system distortions, but also distortions due to the imaged object (i.e. susceptibility distortions caused by the phantom itself); therefore, the results cannot be applied to images of any other object. Moreover, because the magnitude of B_0 distortions are influenced by the sequence parameters (i.e. by the *k*-space trajectory or by the gradient strengths), the results cannot be applied to rectify images of the phantom under different imaging conditions. Lastly, the large size of the detected points – the 14 mm diameter spheres – limits the accuracy with which control point locations can be

detected, and their sparse distribution – 793 control points for body-sized phantom – limits the sampling of the distortion field.

Tanner *et al* and Doran *et al* used a large phantom (440 x 270 x 360 mm^3) containing three sets of intersecting, orthogonal fluid-filled rods within a rigid frame.[12,25] Because point objects were not used, however, a single set of images (i.e. transverse or coronal) can only provide information about in-plane distortion. The 3D information about the distortion field cannot be directly measured, but must be estimated by rescanning the phantom or reformatting and re-analysing the data set in an alternate plane orientation. For example, to obtain an estimate of the 3D distortion field, the (*x, y*) coordinates of control points in the transverse images must be matched with the (*x, z*) coordinates from the coronal images and with the (*y, z*) coordinates in the sagittal images. This greatly increases the work-load and prevents a true 3D measurement of the distortion field.

For full 3D evaluation of the distortion field, Wang *et al* analysed 1.5 T images of a 3D grid-type phantom. The fluid-filled phantom contained a series of plastic grid sheets whose intersection points generated a distribution of 10,830 control points over a 310 x 310 x 310 mm^3 volume. Compared to the previous methods, this phantom design permits a significant increase in the sampling density of the distortion field. However, characterisation of the distortion field implies that the imaged control point locations differ from the "true" locations in a precise and known way, and Wang *et al* make no mention of how the "true" positions were determined. Thus, if there were manufacturing discrepancies affecting the grid regularity, distortion field measurements will be in error.

Furthermore, object and machine related distortion sources were not separated so the distortion data cannot be used to correct images of other objects using different sequence implementations.

The work presented in this chapter seeks to overcome the limitations of previous phantom designs and distortion characterisation schemes. A 3D grid phantom, similar to the design proposed by Wang *et al* is used to finely sample and precisely determine 3D image distortion without the need for combining multiple 2D data sets. Moreover, the phantom is imaged using both MR and CT in order to establish the "true" location of the control points. The reverse gradient technique[26] is used to separate image distortions caused by gradient non-linearity from other sources of distortion. By simulating the magnetic susceptibility distortions[27,28] of the phantom, object-related susceptibility and machine-related B_0 inhomogeneity distortions are further separated. This chapter, therefore, describes the methods and results of our full characterization of the machine-related distortions inherent in our 3.0 T Intera MRI scanner (Philips Medical Systems, Cleveland, OH). By individually characterizing the distortions due to background inhomogeneities, gradient non-linearities and phantom-related susceptibility artifacts for a base set of data, phantom images can be fully corrected when acquired using alternate sequence implementations, while images of other objects can be corrected for machine-related distortions. Armed with detailed knowledge of spatial distortion, MR images can be undistorted and either combined or used individually for new treatment planning methods that benefit from the superior soft-tissue information that magnetic resonance techniques provide.

3.2. Theory

In an MR image, the location of a given feature, r', is shifted from its true position, r, by an amount, Δr. That is:

$$r' = r + \Delta r \qquad \text{Eq. 3-1.}$$

Furthermore, the amount of distortion is proportional to the ratio of the magnetic field perturbation, ΔB, to the gradient strength, G:

$$\Delta r = \frac{\Delta B}{G} \qquad \text{Eq. 3-2.}$$

MR distortion can be determined by comparing the locations of corresponding features in both MR and CT data sets. For phantoms containing easily identifiable point objects, this process is very straightforward. Not only can the total amount of distortion be measured, but using more advanced techniques, the distortions due to different effects can also be separated. Spatial distortions due to field inhomogeneities – caused by imperfections in the polarizing field as well as object-induced local field distortions – are manifest only along frequency encoded directions while spatial distortions due to gradient non-linearities are apparent in each of the 3 cardinal directions.[25] See also §2.2.3.2. For standard (i.e. spin echo and gradient echo) 2D imaging protocols, spatial distortions due to field inhomogeneities appear along the read encode and slice select directions while the phase encode direction is unaffected by such distortion. For the ensuing discussion, we concern ourselves mainly with 3D MR scans where slice selection is done via an

additional phase encoding step and is, therefore, also unaffected by B_0-related distortions. Such distortions are limited to the read direction and to the initial slab-selection process. If the initial slab excitation pulse has an insufficiently broad frequency profile (i.e. if field inhomogeneities cause spins within the desired slice to resonate with frequencies not included within the excitation bandwidth), the outer extremities of the object may not be excited, the slab profile will be distorted and will not correspond to the object profile. However, if the slab width is selected to be larger than the true width of the object, the frequency profile of the excitation pulse may account for resonant frequencies beyond the expected range and all spins within the volume will be excited. By using a sufficiently broad slab width and by further defining the slice direction through phase encoding, field distortions – both machine- and object-specific – need only be considered along the single frequency encoding direction. For example, if the read encode gradient is aligned with the x-axis and phase encodes are performed along each of the y and z axes for a 3D MR scan, the following distortions will be present:

$$
\begin{aligned}
x' = x + \Delta x &= \frac{x \cdot dG_x(x,y,z)}{G_x} + \frac{\Delta B_0(x,y,z)}{G_x} + \frac{\Delta B_\chi(x,y,z)}{G_x} + \frac{\Delta B_{CS}(x,y,z)}{G_x} \\
y = y + \Delta y &= \frac{y \cdot dG_y(x,y,z)}{G_y} \\
xz = z + \Delta z &= \frac{z \cdot dG_z(x,y,z)}{G_z}
\end{aligned}
\qquad \text{Eq. 3-3}
$$

where Δx, Δy, Δz are the total amounts of distortion, G_x, G_y, G_z are the gradient strengths and dG_x, dG_y, dG_z are the gradient non-linearities in each of the three directions; and ΔB_0 ,

ΔB_χ, and ΔB_{CS} are the field distortions due to imperfections in the B_0 field, and susceptibility and chemical shift effects, respectively. Thus, distortions due to ΔB_0, ΔB_χ, and ΔB_{CS} can be separated from x-gradient distortions by reversing the polarity of the read encode gradient, G_x, since this will reverse the signs of $\Delta B_0/G_x$, $\Delta B_\chi/G_x$, and $\Delta B_{CS}/G_x$, but not that of $x \cdot dG_x/G_x$. This effect is illustrated in Figure 3-1 and Figure 3-2.

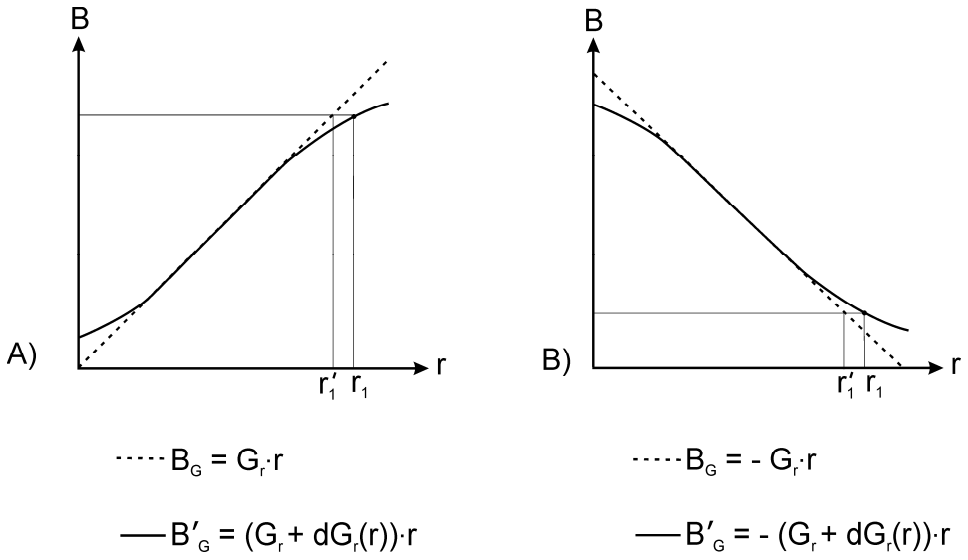

Figure 3-1

Illustration of distortions due to gradient non-linearities for reversed gradient polarities. A) the applied gradient is assumed to be linear (dotted line, G_r), whereas the actual gradient suffers nonlinearities (solid line, $G_r + dG_r(r)$). Thus, a feature at position r_1 is misplaced to the left at position r_1'. B) when the gradient polarity is reversed, the polarity of the non-linearity is also reversed. This means that a feature at position r_1 is again misplaced to the left at position r_1' - distortions due to gradient non-linearities are not sensitive to the gradient polarity.

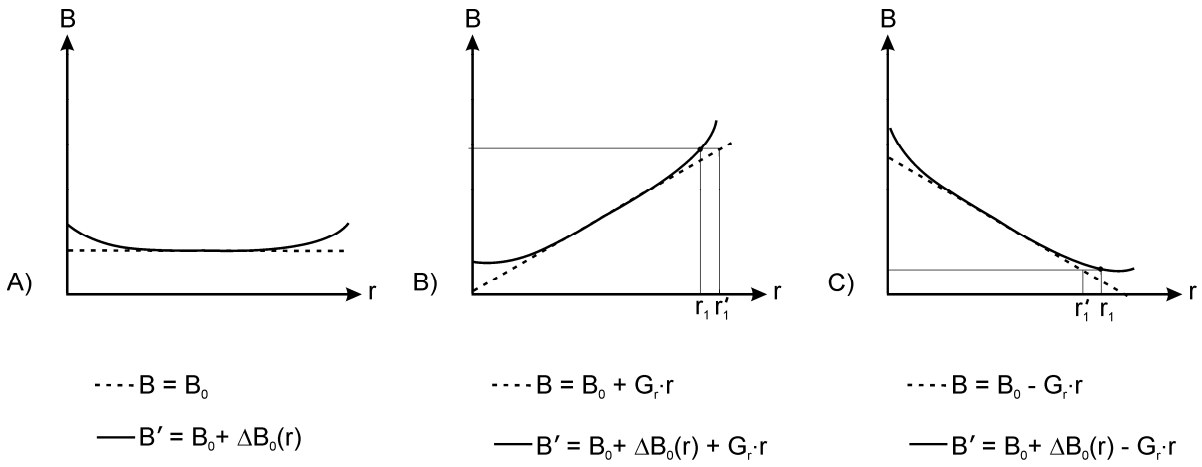

Figure 3-2

Illustration of spatial distortion due to field inhomogeneities under reversal of gradient polarity. A) the background field is assumed to be constant for all *r*, whereas an inhomogeneous field, $B_0 + \Delta B_0(r)$, is actually present. B) when the applied gradient and inhomogeneous background field are superimposed, the resulting magnetic field is B' (solid line). Thus a feature at position r_1 is mistakenly placed to the right at position r_1' if the magnetic field distribution given by *B* (dotted line) is assumed. C) when the gradient polarity is reversed and is again superimposed with the inhomogeneous field, a feature at position r_1 is misplaced to the left at position r_1'. The direction of the spatial distortions due to field inhomogeneities is reversed under gradient polarity reversal whereas distortions due to gradient non-linearity are not. It is this difference that permits the separation of distortion effects through the 'reversed gradient method'.

Figure 3-1 shows that due to non-linearities in the gradient, a feature at position r_1 will be mistakenly placed to the left at position r_1' if the non-linearity is not taken into account; when the gradient and its associated non-linearity are reversed in polarity, the feature at position r_1 is again misplaced to the left at position r_1'. In the case of field inhomogeneities, a perfectly uniform background field is assumed; however, a non-uniform background field exists. When the applied field gradient is superimposed on the non-uniform background field, we see the field profile shown in Figure 3-2 and a feature at position r_1 is misplaced to the right at r_1'. This time when the reversed polarity gradient and the inhomogeneous field are superimposed, a feature at position r_1 is misplaced to the left at r_1'. For example, the x coordinate of a particular feature will be found at position x^+ in an MR image with a positive read encode gradient and at a position x^- in an MR image with a negative read encode gradient. That is,

$$x^+ = x + \frac{x \cdot dG_x(x,y,z)}{G_x} + \frac{\Delta B_0(x,y,z)}{G_x} + \frac{\Delta B_\chi(x,y,z)}{G_x} + \frac{\Delta B_{CS}(x,y,z)}{G_x}$$
$$x^- = x + \frac{x \cdot dG_x(x,y,z)}{G_x} - \frac{\Delta B_0(x,y,z)}{G_x} - \frac{\Delta B_\chi(x,y,z)}{G_x} - \frac{\Delta B_{CS}(x,y,z)}{G_x} \qquad \text{Eq. 3-4}$$

The spatial distortion due to field inhomogeneities can thus be determined by calculating the displacement from the average x position:

$$\frac{x^+ - x^-}{2} = \frac{\Delta B_0(x,y,z)}{G_x} + \frac{\Delta B_\chi(x,y,z)}{G_x} + \frac{\Delta B_{CS}(x,y,z)}{G_x} \qquad \text{Eq. 3-5}$$

The distortion due to the x gradient non-linearities can be determined by subtracting Eq. 3-5 from the total amount of distortion in the x direction, Δx. For a phantom filled with a uniform substance, chemical shift effects will not be an issue; furthermore, for a known geometry and substance, susceptibility distortions can be simulated for the phantom and subtracted from Eq. 3-5. The magnetic field distortions caused by an arbitrary magnetic susceptibility distribution can be simulated using the explicit finite difference method.[28] The 2D algorithm presented by Bhagwandien *et al* [28] is easily extended to three dimensions. Thus, in the absence of chemical shift effects and for a known susceptibility distribution – as is the case with our phantom – susceptibility-induced distortions can be numerically calculated and subtracted from Eq. 3-5 in order to isolate inhomogeneities in the polarizing field, ΔB_0.

Field distortions due to main field inhomogeneity, chemical shift and susceptibility are constant and, therefore, as implied by Eq. 3-2, their related spatial distortions will scale inversely according to the strength of the read gradient. In contrast, field distortions due to gradient non-linearities, dG_x, will scale in proportion to the gradient strength such that the resultant spatial distortions they generate will be constant. Indeed, distortions due to gradient errors have been shown to be independent of gradient strength.[14,25] With these relationships in mind, it should therefore be possible to use the distortions measured in one image to predict distortions in a separate image (i.e. in one acquired using a different read gradient strength and/or direction) by appropriately scaling the image distortions from ΔB_0, ΔB_{CS} , and ΔB_χ. Thus, it may be possible to predict the amount and type of

distortion in images of our phantom for a variety of different imaging protocols for which detailed 3D distortion data is not acquired.

For objects where susceptibility effects are not a concern, the gradient distortions acquired from the data presented in this study could be combined with a scaled version of the B_0 distortion data to predict clinical image distortions. In this case, no additional scans would be necessary to correct patient images. In a more realistic situation, susceptibility effects would be a concern; these could be modeled according to the methods of Bhagwandien *et al,*[28] using information about patient geometry, or the combined effects of susceptibility, chemical shift and B_0 distortions could be measured through phase difference maps according to the methods of Jezzard and Balaban.[29] The latter method involves acquiring two images with slightly different echo times to create a phase difference map. The difference in phase evolution at each pixel can be used to create a detailed field distortion map which can be used to correct all subsequent images for that patient. This procedure is implemented and explored in Chapter 4.

3.3. Methods and Materials

3.3.1. The Phantom

An ideal phantom contains an array of small, localized control points whose precise locations can be determined in all 3 dimensions. The phantom should be rigid and should

provide suitable image contrast in both CT and MR. The design proposed by Wang *et al*[13] was therefore adapted and a similar 3D grid phantom was constructed in-house. The phantom consists of 17 polystyrene grid sheets, evenly spaced within a 30 cm x 30 cm x 30 cm polymethyl methacrylate case. Also constructed was an alignment jig into which the phantom fit; this was used to reduce alignment errors (particularly in the *x* and *y* directions) between subsequent data sets and to facilitate registration of MR and CT data. The phantom is displayed in Figure 3-3. Because the dimensions of the phantom are very close to the resonant RF wavelength of ^{1}H in water – 26cm at 3 T[30] – interference from superimposed RF waves has complex effects on RF homogeneity.[31] The resonant RF wavelength in mineral oil is approximately 160 cm which negates the problem of standing waves when the phantom is used at 3 T and the AAPM thus recommends oil over water to reduce such artefacts.[32]

Control points are found where each of the grid intersections is interfaced with the mineral oil. That is, a control point is defined as the intersection of three planes where the first two planes are contained by the grid and the third plane is the liquid/grid interface. See Figure 3-4. Each of the 17 sheets contains 289 grid points per face for a total of 9,826 control points (2 x 17 x 289). Control point spacing is approximately 15.0 x 15.0 x 7.6 mm in the *x, y,* and *z* dimensions respectively. In the recent study by Wang *et al* using this type of phantom, no mention was made of how the true position of the phantom control points was determined.[13] The authors quote the grid spacing in each of the three dimensions and it is thus assumed that the true control point positions were defined using this perfectly regular spacing. While the grid sheets used in this phantom

experiment were also manufactured and purchased commercially, a small amount of variability, particularly in the *z* direction, was noted. For this reason, the true grid positions were determined via a corresponding CT scan. While the grids are not perfectly rigid, they are immobilized as much as possible through positioning pins embedded inside the phantom.

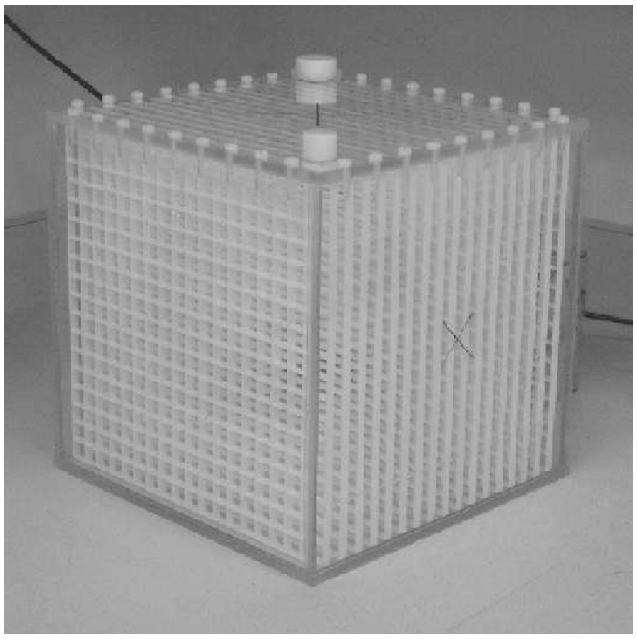

Figure 3-3

The 3D Distortion Characterization Phantom

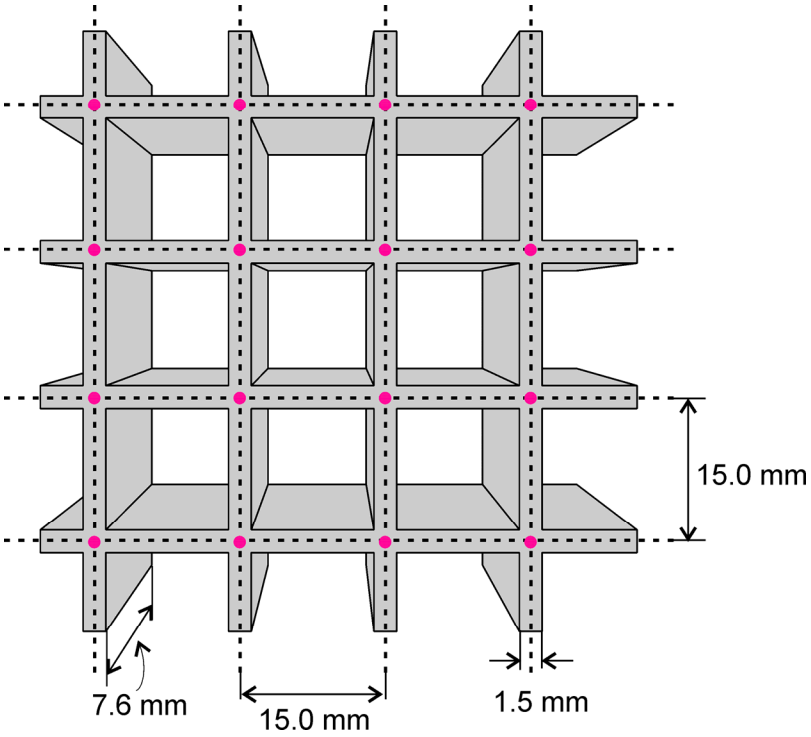

Figure 3-4

Control points are located on the front and back surfaces of each grid sheet, i.e. as indicated by the pink dots for the front surface of the illustrated grid sheet. Grid dimensions are as indicated.

3.3.2. Image Acquisition

MR images were acquired on a 3.0 T Intera MRI scanner (Philips Medical Systems, Cleveland, OH) using the body coil and a standard 3D gradient sequence echo with TE, TR, and flip angle of 5.1 ms, 11.1 ms and 28º respectively. The sequence included phase encode spoiling, but no RF spoiling, and a single *k*-space line was encoded per TR. A

370 mm field of view (FOV) was used along with a 512 x 512 imaging matrix and a total of 440 contiguous slices were acquired at a spacing of 0.72 mm. The resulting *x, y, z* voxel size was thus 0.72 x 0.72 x 0.72 mm^3. The selected slab volume extended approximately 6 cm in the *z*-direction beyond each end of the volume used in our distortion analysis. B_0 distortions were considered in the read encode direction only. In order to separate gradient and B_0/susceptibility distortions in the *x* direction, two 3D scans were performed with identical imaging parameters save the reversal of the read gradient polarity.

Finally, automatic shims were turned off for all scans to eliminate changes in B_0 homogeneity. The auto shimming function was found to moderately increase homogeneity over the central region of the imaged volume at the slight expense of the homogeneity at the volume's extremities. Thus, mean distortions were not significantly increased without the automatic shimming function.

In order to define the true, undistorted control point positions, a corresponding CT scan of the phantom was generated. CT images were acquired using a Philips Gemini PET/CT scanner (Philips Medical Systems, Philadelphia, PA). Again, a 370 mm FOV was used and 600 contiguous slices were acquired with a reduced slice thickness of 0.5 mm due to scanner limitations. Voxel dimensions in the CT data set were thus 0.72 x 0.72 x 0.5 mm^3.

3.3.3. Control Point Detection and Data Alignment

Matlab-based software was developed in order to locate the 3D coordinates of each of the control points in the phantom and was based on an algorithm published by Wang *et al*.[13] For clarity, the method is illustrated in Figure 3-5 and a description of the method follows. Control point detection is based on image edge detection using 3D Prewitt Operators followed by first moment calculation in each of the three orthogonal directions. Initially, the first derivative of the data set is evaluated along the *z* direction (perpendicular to the plane of the grids), resulting in an increased signal at the grid interfaces where the control points are located; this provides an initial estimation of each control point's *z* coordinate (Figure 3-5B). Next the interfacial slices are convolved with a cross-shaped mask to visually enhance the location of the grid points (Figure 3-5C). A threshold is applied and regions of interest (ROIs) are automatically generated around each of the enhanced control points, thus providing additional initial estimates of the *x* and *y* coordinates (Figure 3-5D). The final *x* and *y* coordinates of the control point are determined by calculating the first moment of the magnitude of the derivative evaluated along each of the *x* and *y* directions over an expanded ROI of a standard size (typically 9 x 15 pixels) (Figure 3-5E). The mean *x* position of the control point on the interfacial slice is determined as

$$\bar{I}(j,k) = \frac{\sum_{p=1}^{n_y}\sum_{q=1}^{n_x} i_q \cdot \left| f_x'(i_q, j_p, k) \right|}{\sum_{p=1}^{n_y}\sum_{q=1}^{n_x} \left| f_x'(i_q, j_p, k) \right|} \qquad \text{Eq. 3-6}$$

where f_x' is the derivative evaluated along the x direction, n_x and n_y correspond to the x and y dimensions of the ROI, and i, j, and k are the discretized pixel coordinates in the x, y and z directions, respectively. Because the x and y derivative profiles may not be particularly well-defined at the interfacial slice, this calculation is repeated on all slices within the grid. A line is fit to the x and y coordinates on each slice and the final x and y coordinates are obtained by extrapolating to the interfacial slice. The mean y coordinate is found using an analogous equation. To determine the final z coordinate, a second ROI is centered on the final x and y positions of the control point and the first moment in the z direction was found using a similar equation. In this way, 3D coordinates can be determined for each of the 9,826 control points in the phantom (Figure 3-5E).

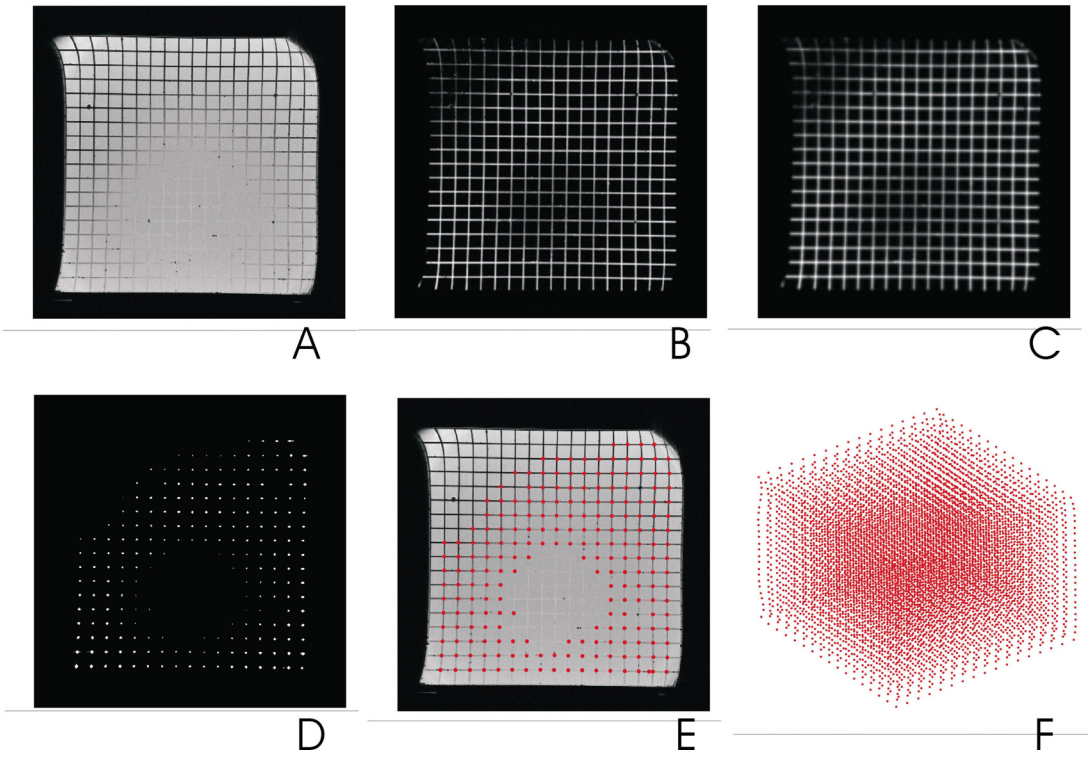

Figure 3-5

A) a representative slice of the 3D grid phantom; B) image derivative evaluated along the *z*-direction at the same location as the slice shown in A; C) the previous slice convolved with a cross-shaped mask; D) the previous image after binary thresholding; E) image A with over-lay of detected control points – note: the control points of a single grid sheet may span several slices in which case the image slice is incremented until all control points are determined; F) a 3D plot of all control points within the grid phantom

Control points may occasionally be obscured by the presence of bubbles within the phantom and on average, the positions of approximately 0.5% of control points were

missing. In such an event, the user may view control points plane-by-plane and missing control points can be interpolated based on the positions of four nearest neighbors.

Finally, pixel indices were converted to Cartesian coordinates using an origin placed at the isocenter of the MR scanner; the information required to perform this transformation is easily obtained from the image's DICOM header file. In a similar fashion, the corresponding Cartesian coordinates of each of the control points was determined from both the reversed read gradient MR scan and the CT scan. The control points in each of the three data sets were sorted from top left to bottom right and from front to back such that corresponding distorted and undistorted control point coordinates could be compared because of their identical positions within the data matrices. By using a set-up jig, which was specially designed to fit both within the MR bore and on top of the PET/CT couch, phantom alignment errors in the x and y directions were minimized. Alignment errors may still exist in the z direction and for this reason, it was necessary to determine an alignment shift which was applied to the CT data set so that the positions of control points near isocenter in both MR and CT data sets coincided. This alignment was achieved by first correcting the MR data for B_0 and susceptibility distortions (i.e. by taking the mean x, y, z coordinates from the positive and negative read gradient scans for each control point). Next, 31 control points in CT and the corrected MR data were manually selected around isocenter (7 along the x and y axes on each of the front and back faces of the central grid and a further 7 along the z axis through isocenter). It should be noted that if gradient distortions are present over the region immediately surrounding isocenter, this registration procedure would be faulty and would introduce a constant shift

into each of the gradient distortion calculations. However, since imaged anatomy is always placed at isocenter, magnets are designed to have minimal distortion over this central region. The previously used assumption that gradient distortions are negligible at isocenter,[12] is employed here. It is thus reasonably assumed that gradient distortions around isocenter are negligible; other groups have previously used this assumption.[12]

3.3.4. Simulation of Susceptibility Distortions

For simple geometries (i.e. cylinders), the field inhomogeneities generated by susceptibility variations can be determined analytically (see § 2.2.3), while more complex geometries require numerical methods. The 3D magnetic field distortions created by the presence of the phantom were calculated using an explicit finite difference method outlined by Bhagwandien *et al*.[28] The method requires knowledge of the geometry, susceptibility value(s), and orientation (with respect to B_0) of the object in question and the solution is derived iteratively by formulating a differential equation based on Maxwell's equations. For further details, the reader is referred to the literature.[28]

The magnetic susceptibility of the mineral oil was measured to be (-8.9 ± 0.5) ppm using an Evans MSB-1 magnetic susceptibility balance while the susceptibility values for the polymethyl methacrylate shell and the polystyrene grids were determined from the literature to be -6.744 ppm and -7.419 ppm respectively.[33] All susceptibility values refer to SI volume susceptibilities, except where noted. The Evans susceptibility balance enables the calculation of material susceptibility by measuring the force exerted on a

small pair of suspended permanent magnets upon interaction of their magnetic fields with that of the sample material.[34] The cgs mass susceptibility (given in cm^3g^{-1}) of the sample material is calculated as

$$\chi_{cgs} = \frac{l}{m}\left[\frac{C(R - R_0)}{10^9} + \chi_V^{air} A\right] \qquad \text{Eq. 3-7}$$

where l is the length of the sample in cm, m is the mass of the sample in grams, C is the calibration constant, R is the balance reading with the sample is in place, R_0 is the reading when the sample is absent, χ_V^{air} is the volume susceptibility of air (0.029×10^{-6} cgs) and A is the cross sectional area of the sample.[34] The SI volume susceptibility can be from the cgs mass susceptibility as

$$\chi = 4\pi\chi_{cgs}\rho \quad \text{Eq. 3-8}$$

where χ is the standard SI volume susceptibility and ρ is the sample density.

3.3.5. Distortion Map Creation

3D distortion maps of *x, y* and *z* gradient non-linearities were generated by comparing the positions of each of the control points from the MR scans (averaged positions) and the CT scan. Distortions due to B_0 and susceptibility effects were calculated using both MR data sets according to the reversed gradient method described in the Theory section.

3.3.6. Distortion Prediction

To our knowledge, distortion measurement and correction procedures previously presented have only shown correction in images acquired using imaging parameters identical to those used for the measurement step. It would be clinically advantageous, however, to be able to correct image distortions for a variety of imaging protocols using a base set of distortion characterization data. We use the base set of distortion data acquired using a 3D gradient echo sequence with frequency encoding in the *x* direction to predict distortion in a 2D SE image with frequency encoding in the *y* direction. Before proceeding with the distortion prediction and correction we first verified that eddy currents did not significantly alter expected distortions when different echo times were used.

3.3.7. Distortion Correction

Once the 3D distortion map is known, the geometric fidelity of MR images can be restored using simple distortion correction techniques. The distortion correction procedure is similar to procedures used in automatic non-rigid image registration and was performed using ITK, an open-source software toolkit (National Library of Medicine Insight Segmentation and Registration Toolkit).[35] The ITK toolkit provides various programming modules useful for image registration purposes. One such module performs inter-modality registration through image warping using an Elastic Body Spline (EBS) kernel.[36] The EBS is a spline based on a physical model of an elastic body; provided with a set of corresponding points in two image sets, it results in a smooth

mapping of one image to the other. Identifying a dense array of corresponding physical points in two image sets can be a difficult problem for standard image registration, but is easily accomplished using the above mentioned phantom and control point detection technique. Furthermore, because the distortion data is defined over a 3D volume, distortion can be corrected in any plane – axial or oblique. The distortion correction procedure used in this study corrects individual 2D image slices; correction for 3D image distortion was implemented in later work – see Chapter 4.

3.4. Results

Corresponding axial slices of the MR and CT phantom data sets are shown in Figure 3-6. As can be seen from the MR image, the amount of distortion over the central region of the phantom is limited while distortion far from the magnet's isocenter is more severe.

Commercially available plastic grids were used to construct our phantom and a small amount of variability in control point spacing was found. It was thus deemed necessary to calculate the MR distortion by measuring the difference in control point positions in MR relative to CT. For example, while warping of the grid planes was observed in the *z* direction in the MR scan, it was also observed (though to a lesser degree) in the CT scan; this is illustrated in Figure 3-7. Without the baseline CT scan, all of the *z* warping seen in the MR scan would be attributed to slice warp and/or *z*-gradient non-linearities. The presence of a small amount of warp in the CT data set indicates the imperfect design of the grids and should not be mistaken for gradient non-linearity.

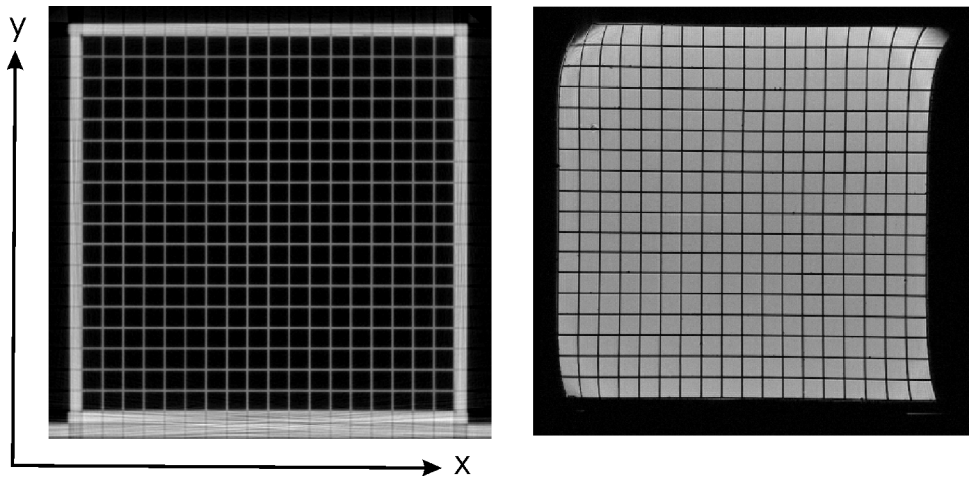

Figure 3-6

A representative CT (left) and MR (right) slice of the phantom.

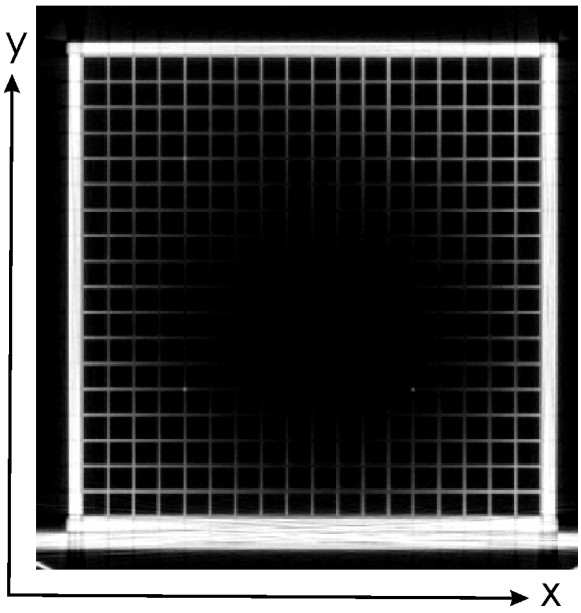

Figure 3-7

CT slice of the one of the grid sections showing visible mechanical distortion in the *z* direction (orthogonal to page). Without determining the true locations of the control points via a CT scan, this warping would be interpreted as *z*-gradient non-linearity.

The distortion caused by each of the gradients and by inhomogeneities in the main magnet was measured and mapped according to Eq. 3-3 - Eq. 3-5 and the distortion due to susceptibility effects was modeled. While these distortions maps are defined over a 3D volume (dimensions 266 x 266 x 205 mm^3), a selection is shown in Figure 3-8 for a transverse plane through isocenter. In this plane, the maximum magnitude of distortion is 4.5 mm in the top right corner of the phantom at a radial distance of 197 mm from isocenter. Figure 3-9 shows the same types of distortion for a transverse plane approximately 8.5 cm from isocenter. Distortions due to non-linearities in the *x, y* and *z*

gradients are similar both in magnitude and in general form at both locations while distortions due to main field inhomogeneities are significantly increased further from isocenter. In this plane, the maximum magnitude of distortion is 5.4 mm and occurs at a radial distance of 215 mm from isocenter. The maximum distortions in our data set generally occur at the top corners of the phantom as the phantom was not perfectly centered in the magnet; the top corners are thus the points furthest from isocenter. It should be noted that while many vendors apply corrections for gradient non-linearities as part of routine post-processing, the Philips 3T Intera magnet does not. Even if such corrections were available, it would still be both prudent and worthwhile to do an independent check of gradient non-linearity distortions and verify the efficacy of automatic image correction.

The field distortions caused by the susceptibility difference between the polystyrene grids and the surrounding oil were modeled as per the discussion in § 3.3.4 and were found to be 0.49 ppm at maximum. For the gradient strength used in this imaging sequence (4.50 mT/m), this corresponds to a maximum linear displacement of 0.33 mm. At approximately half a pixel width, and on the order of the uncertainty of the method, the effect of the grid susceptibility was deemed negligible. Thus, susceptibility distortions were modeled using only the susceptibility distribution of the oil and the polymethyl methacrylate case. Based on the simulations, susceptibility effects result in a maximum absolute distortion of 1.73 ppm or 1.15 mm in the *x* direction.

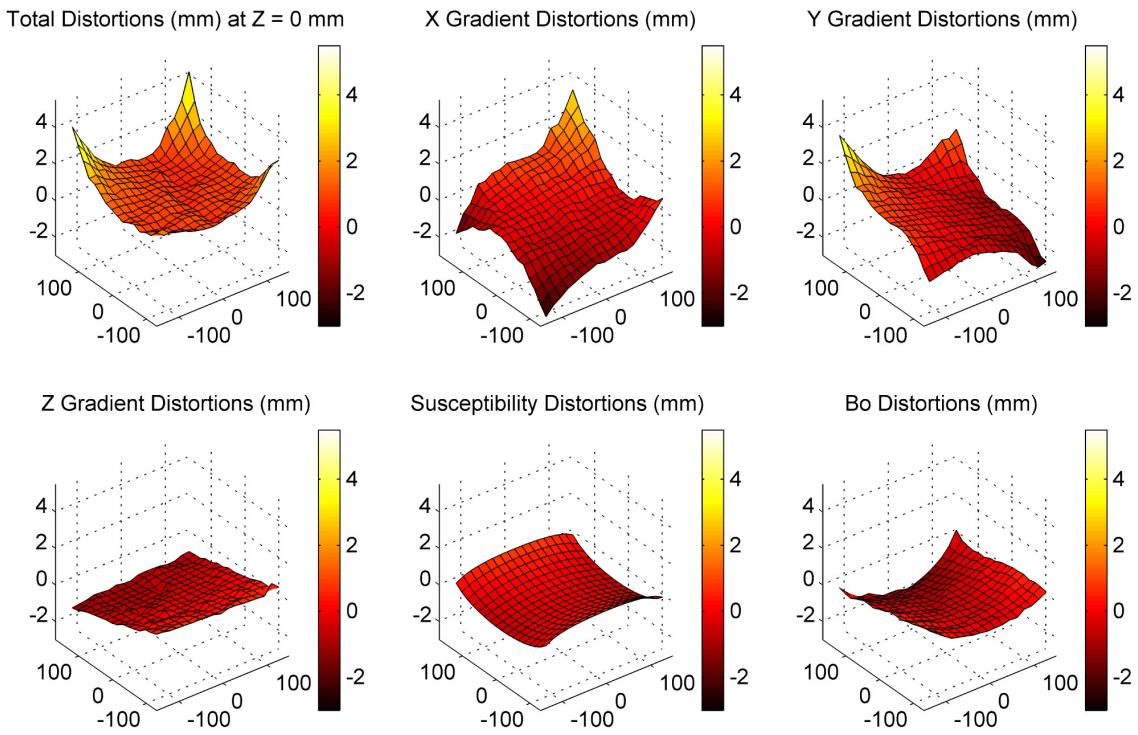

Figure 3-8

Image distortion in a transverse plane through isocenter. Top row (left to right): measured magnitude of spatial distortion, measured spatial distortion due to *x*- and *y*-gradient non-linearity. Bottom row (left to right): measured spatial distortions due to *z*-gradient non-linearity, simulated distortion due to susceptibility effects, and measured spatial distortions due to main field inhomogeneities, ΔB_0.

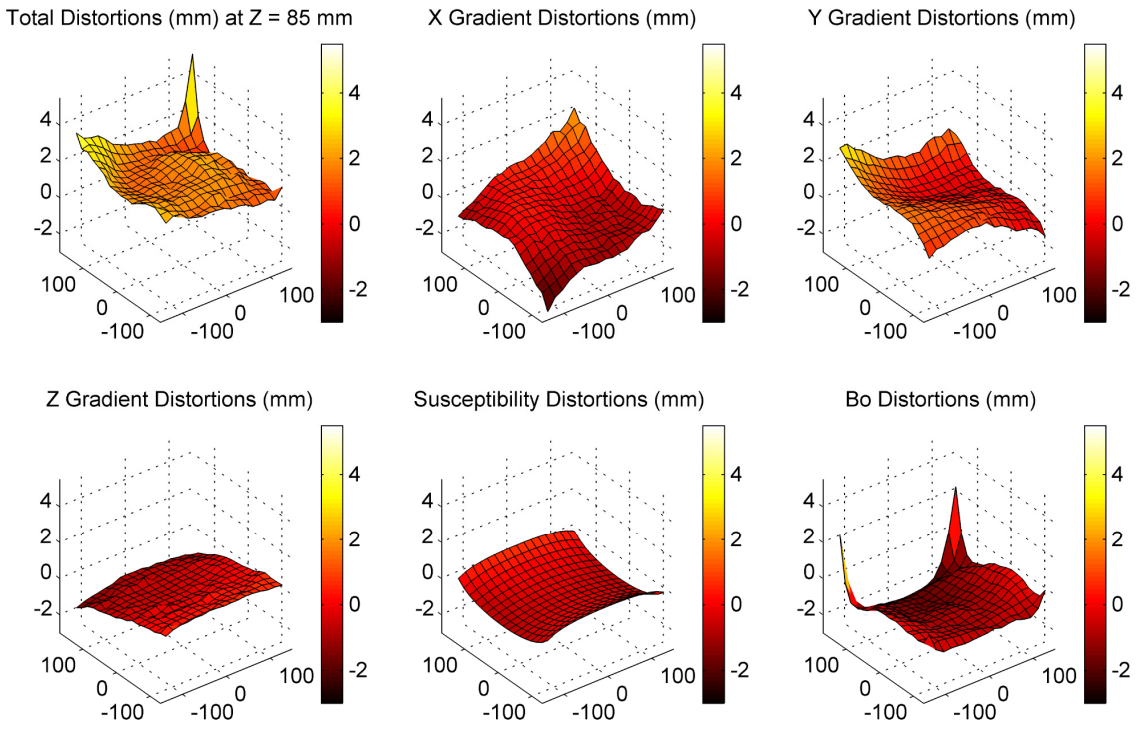

Figure 3-9

Image distortion in a transverse plane 85 mm from the magnet's isocentre. Top row (left to right): measured magnitude of spatial distortion, measured spatial distortion due to *x*- and *y*-gradient non-linearity. Bottom row (left to right): measured spatial distortions due to *z*-gradient non-linearity, simulated distortion due to susceptibility effects, and measured spatial distortions due to main field inhomogeneities, ΔB_0.

The manufacturer's specifications indicate that the peak-to-peak main field homogeneity should be 4.5 ppm for a 40 x 40 x 30 cm^3 rectangular volume and 1.3 ppm for a 20 cm diameter spherical volume. For our approximately 27 x 27 x 21 cm^3 rectangular volume,

we measured maximum peak-to-peak B_0 field inhomogeneity distortions of 8.1 mm in the x direction; this corresponds to 12.2 ppm for the given gradient strength of 4.50 mT/m. For a 20 cm diameter spherical volume, we measured a maximum peak-to-peak distortion of 1.8 mm corresponding to 2.6 ppm. Despite the fact that measured B_0 inhomogeneity was larger than that specified by the manufacturer, gradient non-linearity appeared to be the main source of image distortions over the majority of the analysed volume. B_0 inhomogeneities were only responsible for the majority of image distortion in transverse planes at the extreme ends of the phantom.

In order to validate the reproducibility of the results, distortions were measured on 3 different data sets collected over several months. The phantom was removed from the magnet between scans and the set up jig was used in order to improve the set-up reproducibility. Acquisition parameters were identical in each of the 3 data sets. Unlike the reproducibility study performed by Wang *et al,*[13] this type of study allows testing not only of the performance of the control point detection software, but also the setup and overall distortion reproducibility. As such, slightly higher reproducibility errors are expected. The mean and standard deviation of reproducibility errors between pairs of data sets is graphed in Figure 3-10. Because the phantom was removed and replaced between subsequent scans, distortion measurements are acquired at slightly different positions in each of the data sets. Interpolation of one data set in each of the pairs is thus required in order to compare the reproducibility of distortion measurements at the same locations. A trilinear interpolation scheme was used. The mean and standard deviation of reproducibility errors between data sets 1 and 2 was obtained by averaging the

reproducibility errors when distortion in data set 1 was interpolated at the positions given in data set 2 and vice versa. The same procedure was followed for comparing data sets 1 and 3, and data sets 2 and 3.

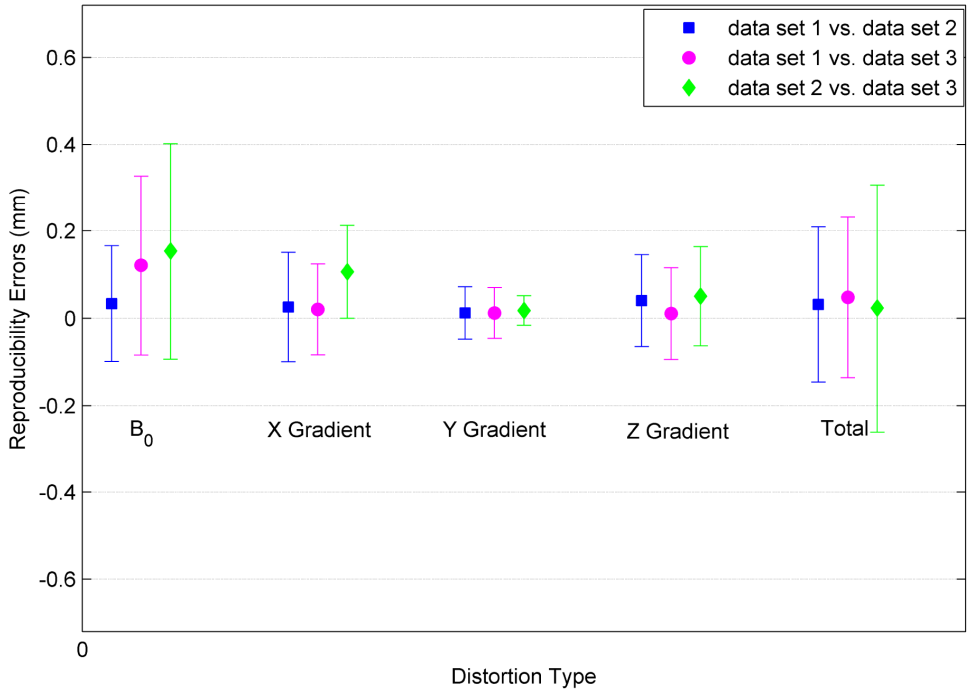

Figure 3-10

Mean reproducibility errors (± standard deviation) for different types of distortion for 3 data sets. Measurement of distortions due to gradient non-linearity is more reproducible than measurement of B_0 distortion.

Clearly spatial distortions caused by non-linearities in the y and z gradients are very reproducible with mean errors (± standard deviation) ranging from 0.02 ± 0.03 mm to

0.05 ± 0.11 mm. These errors are less than ¼ of the pixel dimensions. Reproducibility errors in the *x* gradient, B_0 inhomogeneity and magnitude distortion are somewhat larger and range from 0.02 ± 0.10 to 0.15 ± 0.25 mm. The largest of these errors represents just over ½ a pixel dimension. It should also be noted that interpolation errors contribute to these quoted reproducibility errors; by comparing identical data sets, interpolation was found to contribute 0.0 ± 0.2 mm of intrinsic error.

The variation in maximum and mean total image distortion versus image volume is shown in Figure 3-11. Maximum and mean distortions were calculated over both cubic and spherical volumes of interest around isocenter with cube side length and sphere diameters ranging from 40 mm to 300 mm. As expected, the maximum distortions are always greater in the cubic VOI than in the spherical VOI of corresponding size. For a cubic VOI (side length 300 mm), maximum and mean distortions were 6.40 mm and 1.32 ± 0.53 mm, while for a spherical VOI (diameter 300 mm) they were 2.97 mm and 1.21 ± 0.41 mm.

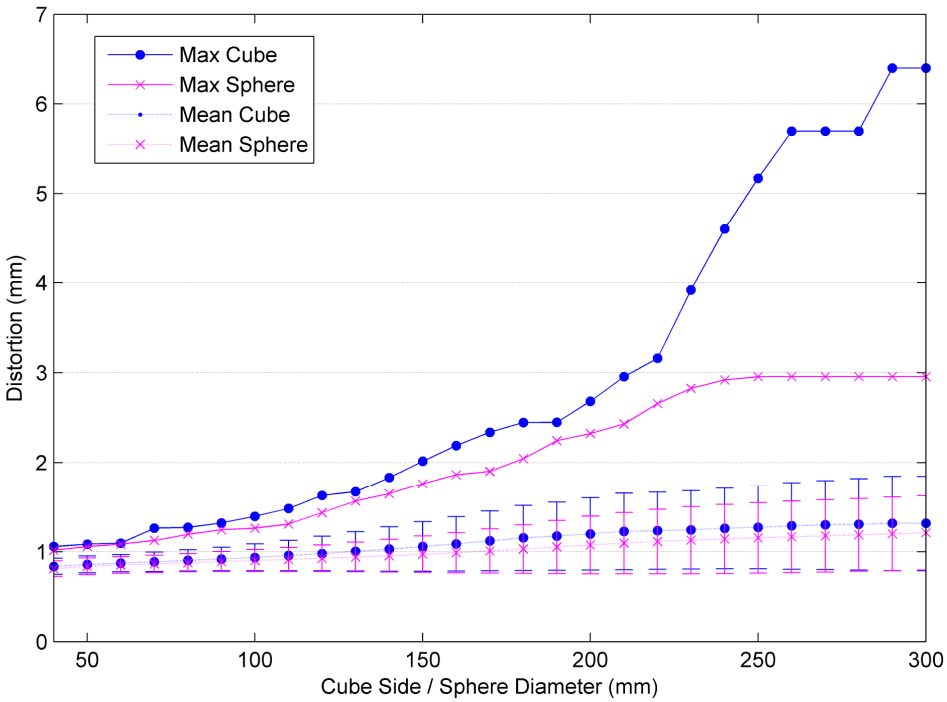

Figure 3-11

Maximum and mean (with standard deviation) magnitude of distortions (mm) over various cubic and spherical volumes of interest

Next, an individual image slice from the 3D data set was corrected using the EBS kernel. Distorted control point coordinates as determined from the MR slice and undistorted control point coordinates as determined from the corresponding CT slice were used as paired landmarks in order to unwarp the MR image geometry to match the correct CT image geometry. The mean (± standard deviation) of spatial distortions for the 289 control points in the slice before image correction was found to be 2.53 ± 0.94 mm. The residual distortion in the corrected image was determined by locating the 2D control

point coordinates in the corrected image (in much the same way that the 3D coordinates were found in the original data set) and comparing them to the known *x* and *y* coordinates of the CT image. Residual distortions were found to be 0.28 ± 0.15 mm; this represents a 9 fold reduction in mean image distortion. The original and corrected images are shown in Figure 3-12A and Figure 3-12B while the difference map is shown in Figure 3-12C. The distortion maps before and after correction are shown in Figure 3-12D and Figure 3-12E, respectively.

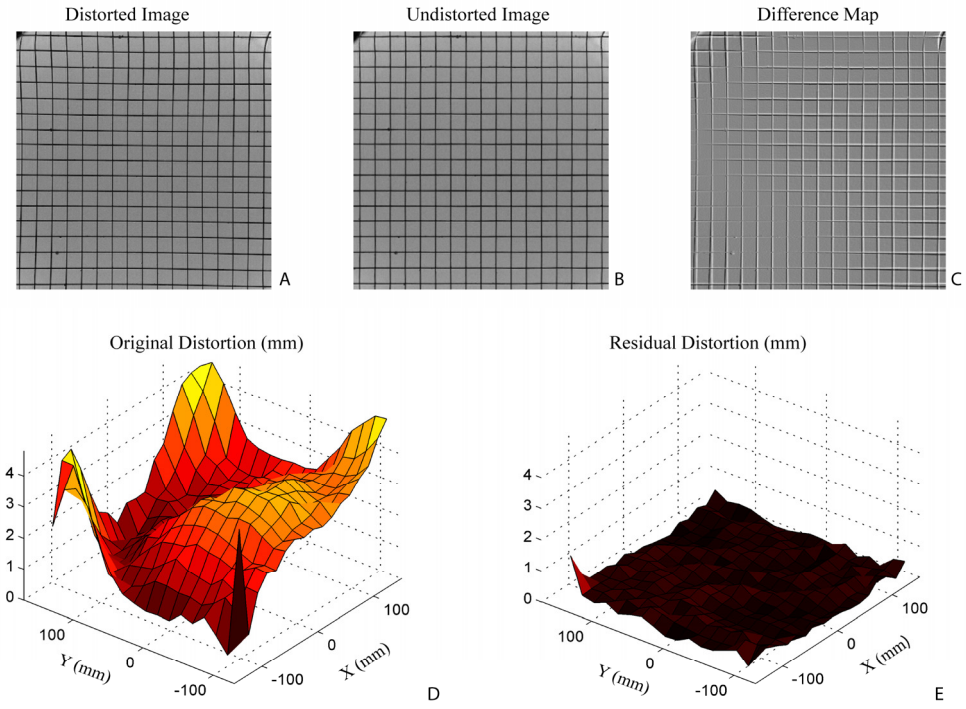

Figure 3-12

A) The original transverse MR image of the grid phantom obtained 94 mm along the *z*-axis from isocenter; B) Image A corrected using the Elastic Body Spline; C) Difference map showing image A – image B (Note: distorted grid lines appear black while corrected grid lines appear white); D) The original distortion map of image A with mean ± standard deviation distortion of 2.53 ± 0.98 mm; E) The residual distortion map of image B; distortion is reduced to 0.28 ± 0.15 mm.

Because many distortion measurement schemes do not separate the different distortion sources, corrections derived from phantom studies cannot be applied to images acquired using different sequence parameters and cannot be applied to (partially) correct images of

other objects. Having separated the various sources of distortions, however, we sought to apply corrections to phantom images acquired using a different sequence implementation. For our purposes, distortion measurements were made with a 3D data set acquired so phase encoding was performed in the slice direction, slice warp was not present, and frequency encoding was carried out only in the *x* direction. In a more typical multi-slice clinical scan, slice warp (B_0 effects) would be present due to the additional frequency encoding in the slice direction; however, slice warp could easily be predicted and accounted for since distortion sources are separated in the initial data set. Unfortunately, Tanner *et al* showed that eddy currents generated by rapidly pulsed gradients caused system distortions to be dependent upon echo times,[25] and we therefore began by investigating the significance of such eddy currents in our magnet. To do so, we measured the distortion at the four corners of a series of five identical gradient echo image acquisitions and compared this to distortion measurements on a series of five gradient echo images where the echo time was increased in each successive image. The results of this experiment are shown in Table 3-1. The average uncertainty (standard deviation) in distortion measurement was 0.06 mm for the five identical images and was 0.24 mm for the five images with TEs ranging from 5 to 50 ms. A similar experiment was carried out with spin echo images and the uncertainty was found to increase from 0.05 mm to 0.27 mm. This approximately four-fold increase in the uncertainty in distortion measurements could be attributed to differences in remnant eddy currents. Despite the increase in uncertainty, distortion was measured at the four corners (where distortions are expected to be greatest) to within half a pixel of uncertainty and eddy current effects were deemed negligible in such cases. Indeed, the Philips 3T Intera

system is equipped with shielded gradients and eddy currents are compensated using pre-emphasis calibration; although these measures may not negate all effects of eddy currents, the residual effects will not appreciably affect the proposed distortion prediction scheme.

Control Point	Mean distortion ± standard deviation [mm]	
	5 identical acquisitions	5 different echo times (5,10,20,30,50 ms)
Top Left	-0.01 ± 0.05	-0.22 ± 0.30
Top Right	4.97 ± 0.07	4.91 ± 0.30
Bottom Left	-0.73 ± 0.07	-1.02 ± 0.20
Bottom Right	1.79 ± 0.04	1.83 ± 0.16

Table 3-1

Effects of eddy currents on distortion measurements. Distortion was measured in the 4 corners (top left, top right, bottom left, bottom right) of the phantom for 5 identical image acquisitions (to estimate noise contributions) and for 5 image acquisitions with increasing echo times (to estimate the effect of time-varying eddy currents on distortion measurements). The mean and standard deviation was calculated at each corner for each of the two sets of measurements. Measurement uncertainty increased when echo times were varied but remained within the range of half a pixel dimension.

Distortion prediction was therefore tested on a mulit-slice spin echo (SE) image of the phantom with frequency encoding in the *y*-direction. Distortions measured from the 3D GE sequence were used as the basis from which to predict the distortion in the SE image. Gradient non-linearity distortion corrections were directly applied, while the B_0 and susceptibility distortions were scaled according to the strength of the SE frequency encoding gradient and were applied in the appropriate direction (i.e. along the *y*-axis). Figure 3-13A shows a gradient echo image of the phantom at $z = 85$ mm; the frequency encode direction is aligned with the *x*-axis and a large amount of distortion is thus observed in the horizontal direction. Figure 3-13B shows the SE image acquired at the same *z* location, but with the frequency encoding (and largest amount of distortion) along the *y* direction. Using the image distortion map created from the GE image in Figure 3-13A, the distortion map for the SE image in Figure 3-13B was predicted and the image was corrected. The corrected SE image is shown in Figure 3-13C while a difference map (original – corrected) is shown in Figure 3-13D. By predicting and correcting the spatial distortion in the SE image, mean distortion was reduced from 1.63 ± 1.02 mm to 0.29 ± 0.22 mm.

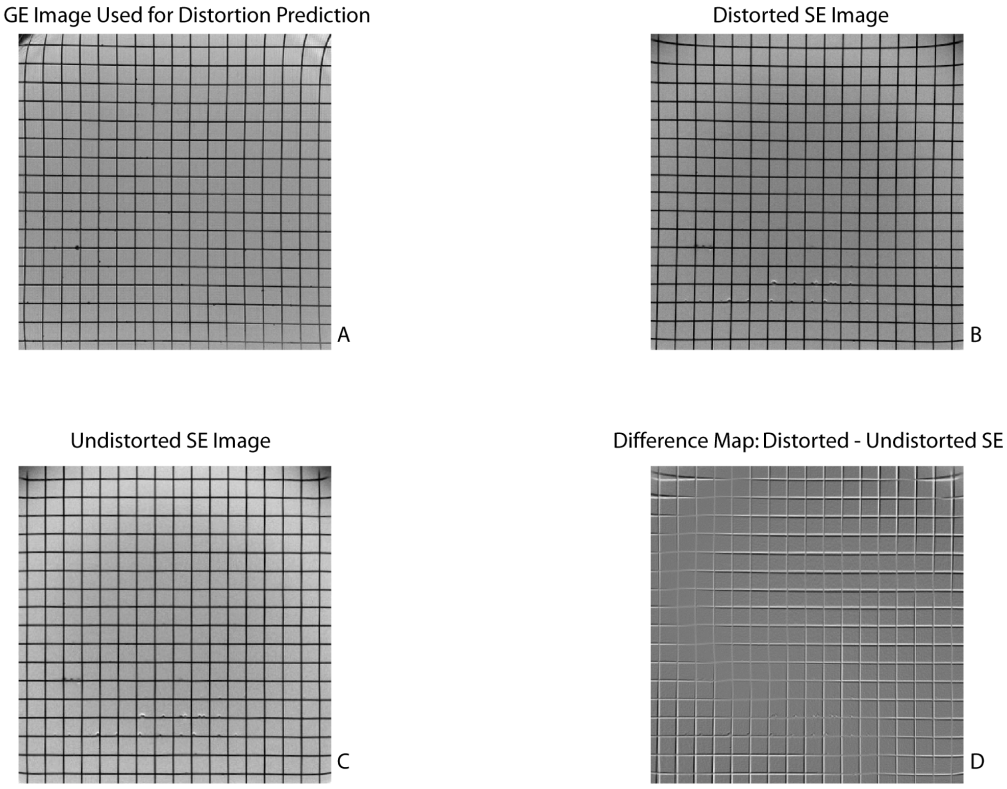

Figure 3-13

A) a single distorted slice of the 3D GE image from which distortion maps were obtained. The most pronounced distortion is visible in the *x*-direction (horizontal); B) a distorted SE. The most pronounced distortion is visible in the *y*-direction (vertical); C) the SE image following distortion correction (the spatial distortion map for the SE image was predicted based on the GE distortion map). The distortion was reduced from 1.63 ± 1.02 mm to 0.29 ± 0.22 mm; D) a difference map showing Image B – Image C (Note: the distorted grid lines appear black while the corrected grid lines appear white).

In order to verify the accuracy of the distortion prediction, the control point locations for the SE image were also automatically measured. The mean ± standard deviation value for the difference in predicted and measured control point locations was 0.27 ± 0.23 mm respectively; this represents less than one pixel of discrepancy. Image correction using the automatically measured image distortion yielded a mean residual distortion of 0.14 ± 0.07 mm. This result is slightly better than that achieved by the using the predicted distortion, 0.29 ± 0.22 mm; however, the ability to predict distortion to within one pixel of accuracy allows a variety of different images of the same object to be corrected based on one set of distortion data. That is, distortion maps do not need to be calculated for each specific imaging sequence.

3.5. Discussion

In order to make use of the excellent soft tissue imaging capabilities of MR in the radiation treatment planning procedure, inherent image distortions need to be measured and removed. This is most easily done using some type of phantom measurement and the previous literature suggests a variety of phantom types. The phantom presented in this study and in those by Wang *et al* [13] has over 12 times as many control points as the phantom presented by Breeuwer *et al*;[11,23] this permits a much higher sampling rate of the distortion field. Combined with the much smaller physical size of each control point, this allows a more comprehensive and precise characterisation of image distortion. Compared to the phantom (linearity test object, LTO) used by Doran *et al,*[12] our grid phantom has both advantages and disadvantages. Because the control points in our

phantom occur at well-specified points and are not the extended rod objects of the LTO, it is possible to accurately quantify distortions in all three dimensions; our phantom allows straightforward through-plane distortion measurement. Our phantom is, however, quite heavy and cumbersome compared to the mostly air-filled LTO. It is further acknowledged that a larger phantom, more representative of the size and shape of a human torso, is required to facilitate distortion correction over more clinically relevant volumes. Such design modifications were subsequently undertaken and results using the larger phantom are detailed in the following chapter. Finally, as compared to the control point detection scheme used by Doran *et al*,[12] our detection scheme does not require manual matching of any control points in MR and CT.

In terms of the method used to quantify distortions, our approach again shows advantages over the previously published methods. In the study by Wang *et al* using the same type of phantom, it appears distortion measurements were made relative to *a priori* known control point locations – it is not, however, mentioned how these control point locations were determined.[13] It is thus understood by our group that a perfectly regular spacing of the control points was assumed and that distortion was measured relative to this assumed spacing. This assumption was avoided in our study as control grid locations were directly measured using a corresponding CT scan. Indeed, Figure 3-7 illustrated the fact that MR grids were slightly warped even in CT images. Having independently measured the control point locations using CT, we can be confident that the calculated distortion maps account for displacement of control point locations due to imaging effects only.

This investigation showed that gradient non-linearities were the main component of image distortion near the center of the magnet; this finding is in agreement with that of Wang *et al* for a 1.5 T magnet.[13] As such, image distortions on a 3 T MR system will not necessarily be larger than those found at 1.5 T (since it is only ΔB_0, ΔB_{CS}, and ΔB_χ that scale with the strength of the polarizing field). Indeed, Wang *et al* found maximum distortions on their 1.5 T system of 10-25 mm over a 240 x 240 x 240 mm^3 volume while we found maximum absolute distortions of less than 7 mm over a 266 x 266 x 205 mm^3 volume on our 3 T system. (Note: software corrections were not applied). In addition, Doran *et al* report a maximum absolute distortion (due to gradient non-linearities only) of 9 mm over a volume of 257 x 255 x 257 mm^3.[12] Although B_0 and susceptibility distortions have a larger effect at higher field strengths, we report smaller maximum distortions at 3 T than previous researchers reported at 1.5 T. Finally, in agreement with the literature, we showed that distortion measurements were very stable when monitored over several months.[24] Together, these results imply that the Philips 3 T Intera is a well-shimmed system with excellent gradient linearity and minimal B_0 inhomogeneity; as such it is a suitable system for moving forward with MR-based radiotherapy applications.

Although it is advantageous to carry out MR-based radiotherapy studies using a system which generates minimal image distortion, post-processing techniques can be used to further improve the geometric accuracy of MR images. Through distortion correction, mean distortions in our 3T MR system were reduced from 2.43 ± 0.94 mm to 0.28 ± 0.15 mm in an image from which distortion maps were created. For an alternative imaging sequence, the base set of distortion maps was used to predict and correct the image

distortion. Following the prediction and image correction, distortion was reduced from an initial amount of 1.63 ± 1.02 mm to 0.29 ± 0.22 mm (less than one pixel of residual distortion). This illustrates how an accurate initial characterization of magnetic field variations and gradient non-linearities can lead to the satisfactory correction of images acquired with any number of different imaging protocols; individual time-consuming distortion characterization scans are not required for each image.

The fat/water chemical shift has not expressly been dealt with in this study since the phantom contained a single molecular compound. If both fat- and water- based signal had been present, all signal arising from fat would be offset with respect to the water signal due to the difference in local resonance frequencies. In order to circumvent this problem, there are a number of potential strategies: 1) fat suppression techniques can be used; 2) the read gradient can be maximized to reduce the effects of distortion from not only ΔB_{CS}, but also ΔB_0 and ΔB_χ as per Eq. 3-2 – this strategy, however, comes at the cost of reduced SNR;[20,37] 3) an additional image can be acquired to provided information about field distortions and this information can be used to correct chemical shift artefacts in a post-processing step. The third method, field mapping, is introduced in Chapter 4.

The results of this study suggest that machine-related distortion in 3T MR images can be adequately corrected and that images which meet the stringent requirements of spatial accuracy for treatment planning can be produced. After segmenting MR images and applying bulk electron density information, some literature suggests RTTP could be carried out with MR images alone – without the need for image registration and without

the introduction of errors associated with this process.[20,22] Other literature suggests that while MRI provides superior soft-tissue contrast and more complete and more consistent tumour delineation, the tumour volume information provided by MR is complimentary to that provided by CT. If this is the case, it may be prudent to use both MR and CT images to provide a composite co-registered image.[1,5] However, fusing CT images to MR when the MR image suffers from geometric distortion will only exacerbate the fusion errors by forcing registration to a geometrically incorrect volume. Whether or not MR images are used alone or fused with CT, it can only be beneficial to start with images which are free of distortions and as spatially accurate as possible.

3.6. Conclusions

The work described in this chapter was undertaken in an effort to support future investigations relating to MR-based radiotherapy treatment planning. Specifically, we set out to 1) construct a 3D phantom that could be used to accurately determine machine-related geometric image distortion over a reasonable field of view; 2) separate machine and object distortions so that machine-related distortion corrections could be applied to images of other objects; 3) verify the accuracy of both direct distortion correction and indirect distortion correction (i.e. distortion prediction); and 4) investigate the magnitude of image distortions at 3T in order to evaluate the usefulness of the Philips 3T Intera system for future MR-based radiotherapy treatment planning applications.

Geometric distortion due to both inhomogeneities in the background field and non-linearities in the applied gradients were easily visualized on the MR images of a regularly structured 3D grid phantom. From a CT scan, the locations of just under 10,000 control points within the phantom were accurately determined in three dimensions using a Matlab-based computer program. MR distortion was then determined by measuring the corresponding locations of the control points when the phantom was imaged using the MR scanner. Using a reversed gradient method, distortions due to gradient non-linearities were separated from distortions due to inhomogeneities in the background B_0 field. Because the various sources of machine-related distortions can be individually characterized, distortions present in other imaging sequences (for which 3D distortion cannot accurately be measured using phantom methods) can be predicted negating the need for individual distortion measurement for a variety of other imaging sequences. Distortions were found to be primarily caused by gradient non-linearities and maximum image distortions were reported to be less than those previously found by other researchers at 1.5 T. Image slices were corrected for distortion in order to provide geometrically accurate phantom images and the reliability of the correction procedure was validated by comparing distortion-corrected control point locations to true (i.e. as determined from CT) control point locations. The results of this study show that geometrically accurate images are possible at 3T despite the linear increase of B_0 inhomogeneities and susceptibility effects. The use of MRI in radiotherapy treatment planning appears to be a feasible clinical option at 3 T due to both the minimal distortions observed and the ease and efficacy with which distortions can be corrected.

The methods presented here in Chapter 3 are expanded upon in Chapter 4 to include characterization of gradient non-linearities over a larger field of view as well as methods for correction of all types of image distortions – both machine- and patient-related.

3.7. References

[1] B. Emami, A. Sethi, and G. J. Petruzzelli, "Influence of MRI on target volume delineation and IMRT planning in nasopharyngeal carcinoma," Int. J. Radiation Oncology Biol. Phys. **57,** 481-488 (2003).

[2] V. S. Khoo, A. R. Padhani, S. F. Tanner, D. J. Finnigan, M. O. Leach, and D. P. Dearnaley, "Comparison of MRI with CT for the radiotherapy planning of prostate cancer: a feasibility study," Br J Radiol **72,** 590-7 (1999).

[3] B. H. Kristensen, F. J. Laursen, V. Logager, P. F. Geertsen, and A. Krarup-Hansen, "Dosimetric and geometric evaluation of an open low-field magnetic resonance simulator for radiotherapy treatment planning of brain tumours," Radiother Oncol **87,** 100-109 (2008).

[4] S. H. Ng, V. F. Chong, S. F. Ko, and S. K. Mukherji, "Magnetic resonance imaging of nasopharyngeal carcinoma," Top Magn Reson Imaging **10,** 290-303 (1999).

[5] R. K. Ten Haken, A. F. Thronton, H. M. Sandler, M. L. LaVigne, D. J. Quint, B. A. Fraass, M. L. Kessler, and D. L. McShan, "A quantitative assessment of the addition of MRI to CT-based, 3-D treatment planning of brain tumors," Radiotherapy and Oncology **25,** 121-133 (1992).

[6] A. F. Thornton, Jr., H. M. Sandler, R. K. Ten Haken, D. L. McShan, B. A. Fraass, M. L. La Vigne, and B. R. Yanke, "The clinical utility of magnetic resonance imaging in 3-dimensional treatment planning of brain neoplasms," Int J Radiat Oncol Biol Phys **24,** 767-75 (1992).

[7] A. S. Jackson, S. A. Reinsberg, S. A. Sohaib, E. M. Charles-Edwards, S. A. Mangar, C. P. South, M. O. Leach, and D. P. Dearnaley, "Distortion-corrected T2 weighted MRI: a novel approach to prostate radiotherapy planning," Br J Radiol **80,** 926-933 (2007).

[8] M. Roach, 3rd, P. Faillace-Akazawa, C. Malfatti, J. Holland, and H. Hricak, "Prostate volumes defined by magnetic resonance imaging and computerized tomographic scans for three-dimensional conformal radiotherapy," Int J Radiat Oncol Biol Phys **35,** 1011-8 (1996).

[9] M. Debois, R. Oyen, F. Maes, G. Verswijvel, G. Gatti, H. Bosmans, M. Feron, E. Bellon, G. Kutcher, H. Van Poppel, and L. Vanuytsel, "The contribution of magnetic resonance imaging to the three-dimensional treatment planning of localized prostate cancer," Int J Radiat Oncol Biol Phys **45,** 857-865 (1999).

[10] D. Wang, W. Strugnell, G. Cowin, D. M. Doddrell, and R. Slaughter, "Geometric Distortion in clinical MRI systems Part I: evaluation using a 3D phantom," Magnetic Resonance Imaging **22,** 1211-1221 (2004).

[11] M. Breeuwer, M. Holden, and W. Zylka, "Detection and correction of geometric distortion in 3D MR images," Proceedings of SPIE **4322,** 1110-1120 (2001).

[12] S. J. Doran, E. M. Charles-Edwards, S. A. Reinsberg, and M. O. Leach, "A complete distortion correction for MR images: I. Gradient warp correction," Physics in Medicine and Biology **50,** 1343-1361 (2005).

[13] D. Wang, D. M. Doddrell, and G. Cowin, "A novel phantom and method for comprehensive 3-dimensional measurement and correction of geometric distortion in magnetic resonance imaging," Magnetic Resonance Imaging **22,** 529-542 (2004).

[14] C. J. G. Bakker, M. A. Moerland, R. Bhagwandien, and R. Beersma, "Analysis of Machine-Dependent and Object-Induced Geometric Distortion in 2DFT MR Imaging," Magnetic Resonance Imaging **10,** 597-608 (1992).

[15] D. L. Hill, D. J. Hawkes, M. J. Gleeson, T. C. Cox, A. J. Strong, W. L. Wong, C. F. Ruff, N. D. Kitchen, D. G. Thomas, A. Sofat, and et al., "Accurate frameless registration of MR and CT images of the head: applications in planning surgery and radiation therapy," Radiology **191,** 447-54 (1994).

[16] C. P. Karger, A. Hoss, R. Bendl, V. Canda, and L. Schad, "Accuracy of device-specific 2D and 3D image distortion correction algorithms for magnetic resonance imaging of the head provided by a manufacturer," Phys Med Biol **51,** N253-61 (2006).

[17] R. Gruetter, S. A. Weisdorf, V. Rajanayagan, M. Terpstra, H. Merkle, C. L. Truwit, M. Garwood, S. L. Nyberg, and K. Ugurbil, "Resolution Improvements in *in Vivo* ^{1}H NMR Spectra with Increased Magnetic Field Strength," Journal of Magnetic Resonance **135,** 260-264 (1998).

[18] B. L. Schmitz, A. J. Aschoff, M. H. K. Hoffmann, and G. Grön, "Advantages and Pitfalls in 3T MR Brain Imaging: A Pictorial Review," American Journal of Neuroradiology **26,** 2229-2237 (2005).

[19] J. T. Vaughn, M. Garwood, C. M. Collins, W. Liu, L. DelaBarre, G. Adriany, P. Andersen, H. Merkle, R. Goebel, M. B. Smith, and K. Ugurbil, "7T vs. 4T: RF Power, Homogeneity, and Signal-to-Noise Comparison in Head Images," Magnetic Resonance in Medicine **46,** 24-30 (2001).

[20] A. Fransson, P. Andreo, and R. Potter, "Aspects of MR Image Distortions in Radiotherapy Treatment Planning," Strahlentherapie und Onkologie **177,** 59-73 (2001).

[21] C. A. Pelizzari, G. T. Chen, D. R. Spelbring, R. R. Weichselbaum, and C. T. Chen, "Accurate three-dimensional registration of CT, PET, and/or MR images of the brain," J Comput Assist Tomogr **13,** 20-6 (1989).

[22] Y. K. Lee, M. Bollet, G. Charles-Edwards, M. A. Flower, M. O. Leach, H. McNair, E. Moore, C. Rowbottom, and S. Webb, "Radiotherapy treatment planning of prostate cancer using magnetic resonance imaging alone," Radiotherapy and Oncology **66,** 203-216 (2003).

[23] M. Breeuwer, W. Zylka, J. Wadley, and A. Falk, in *CARS* (Paris, France, 1999).

[24] M. Holden, M. Breeuwer, K. McLeish, D. J. Hawkes, S. F. Keevil, and D. L. G. Hill, in *SPIE*; *Vol. 4322*, edited by M. Sonka and K. M. Hanson (2001).

[25] S. F. Tanner, D. J. Finnigan, V. S. Khoos, P. Mayles, D. P. Dearnaley, and M. O. Leach, "Radiotherapy planning of the pelvis using distortion corrected MR images: the removal of system distortions," Phys. Med. Biol **45,** 2117-2132 (2000).

[26] H. Chang and J. M. Fitzpatrick, "A technique for accurate magnetic resonance imaging in the presence of field inhomogeneities," IEEE Trans Med Imaging **11,** 319-329 (1992).

[27] R. Bhagwandien, M. A. Moerland, C. J. Bakker, R. Beersma, and J. J. Lagendijk, "Numerical analysis of the magnetic field for arbitrary magnetic susceptibility distributions in 3D," Magn Reson Imaging **12,** 101-7 (1994).

[28] R. Bhagwandien, R. van Ee, R. Beersma, and C. J. G. Bakker, "Numerical Analysis of the Magnetic Field for Arbitrary Magnetic Susceptibility Distributions in 2D," Magnetic Resonance Imaging **10,** 299-313 (1992).

[29] P. Jezzard and R. S. Balaban, "Correction for geometric distortion in echo planar images from B0 field variations," Magn Reson Med **34,** 65-73 (1995).

[30] F. Schick, "Whole-body MRI at high field: technical limits and clinical potential," Eur Radiol **15,** 946-959 (2005).

[31] D. I. Hoult and D. Phil, "Sensitivity and power deposition in a high-field imaging experiment," Journal of Magnetic Resonance Imaging **12,** 46-67 (2000).

[32] R. R. Price, L. Axel, T. Morgan, R. Newman, W. Perman, N. Shneiders, M. Selikson, M. Wood, and S. R. Thomas, "Quality assurance methods and phantoms for magnetic resonance imaging: report of AAPM nuclear magnetic resonance Task Group 1," Medical Physics **17,** 287-95 (1990).

[33] *CRC Handbook of Chemistry and Physics*; *Vol.*, edited by D. R. Lide (Chemical Rubber Company, Boca Raton, Fla., 2002).

[34] J. Woolcock and A. Zafar, "Microscale techniques for determination of magnetic susceptibility " Journal of Chemical Education **69,** A176 - A179 (1992).

[35] http://www.itk.org/, (2006).

[36] M. H. Davis, A. Khotanzad, D. P. Flamig, and S. E. Harms, "A Physics-Based Coordinate Transformation for 3-D Image Matching," IEEE Transactions on Medical Imaging **16,** 317-328 (1997).

[37] D. G. Nishimura, *Principles of Magnetic Resonance Imaging* (Stanford University Press, 1996).

4. Chapter 4: Validation of a clinically suitable distortion characterisation scheme

4.1. Introduction

In recent years, considerable interest has been shown in MR for use in radiation treatment planning. This can be attributed to (1) the superior soft tissue contrast of MR compared to computed tomography (CT) which results in better structure delineation,[1,2] and (2) the growing use of conformal dose delivery techniques which require greater accuracy in tumor delineation. Unfortunately, geometric distortions hamper the utility of MRI for radiotherapy applications. In the previous chapter, distortions of up to 7 mm were found over a 266 x 266 x 205 mm^3 FOV, while the literature cites larger distortions over smaller fields of view (i.e. up to 25 mm over a 240 mm FOV)[3-5]. Despite such findings, reports of MR-based treatment planning and comparisons of tumour volumes delineated on MR and CT images far outweigh the reports of detailed distortion measurement and correction schemes. In many cases, distortion correction is based on vendor-supplied methods[6], or patient-related distortions are assumed negligible because either low field systems[7-10] or small fields of view are used.[11-13] While distortions may be limited at low field strengths and for small FOVs, these assumptions cannot be extended to large FOVs and higher field strengths: many types of geometric distortion scale in proportion to the strength of the background field

and distortions typically increase for larger FOVs. Furthermore, much of the MR distortion correction literature focuses on gross image distortion observed in echo planar images.[14-16] The efficacy of these correction methods are qualitatively observed, but quantitative measurements of residual distortion are not given for the more subtle forms of image warping which may affect typical treatment planning images.[17-19] Before proceeding to MR-based treatment planning, it is our belief that further methods for measuring and correcting MR distortion remain to be developed; these corrections should be vendor-independent, comprehensive (i.e. accounting for both machine- and patient-related distortions), and verifiable.

Chapter 3 described a method for distortion measurement and correction based on images of a cubic phantom containing a regular array of grids.[20] By combining the reverse gradient method with simulations of the phantom susceptibility distortions, both gradient non-linearity and B_0 distortions were characterized. The method was shown to be both an accurate and reproducible means of measuring and correcting machine-related distortion. However, because of the small size of the original phantom (30 cm x 30 cm x 30 cm), distortions could only be characterized over a limited field of view. Furthermore, patient (or object) related distortions were not expressly dealt with. Chemical shift distortions were not present and susceptibility distortions were simulated based on the phantom's known geometry and composition. Although in-vivo patient susceptibility distortions could be simulated,[21,22] such a solution is not ideal since neither

precise patient geometry nor composition is known without additional scanning information (i.e. CT) or atlas-based approximations of patient anatomy.

The current chapter outlines a complete and time-efficient method for distortion measurement of both machine- and patient-related distortion sources. The method builds upon the foundations presented in Chapter 3 by acquiring gradient non-linearity distortion information over an increased and clinically relevant field of view; furthermore, it combines the phantom-based measurement of gradient non-linearity through the reverse gradient method with measurement of field distortions caused by B_0 inhomogeneity, susceptibility and chemical shift through a double echo gradient echo phase mapping scan.[19] Where more than one imaging sequence may be required for tumor diagnosis and delineation,[6] this method could save considerable patient scanning time since images from several sequences can be corrected based on the same field distortion map which takes approximately 2 minutes to acquire. The comprehensive measurement and correction scheme was validated on a variety of phantoms, each designed to highlight a different type of distortion; it was then applied to correct images of a patient volunteer. The method minimally increases patient scan time, is robust, corrects for both system- and patient-related distortions, is applicable for a variety of sequences, and can be applied at any field strength.

4.2. Theory

In the preceding discussion, image distortions were classified as being either machine- or patient-related. For the purposes of the current chapter, however, an alternate classification is more appropriate: geometric image distortions are either sequence-independent or sequence-dependent.

4.2.1. Sequence-independent spatial distortions

Sequence independent spatial distortions are those due to gradient non-linearities. Every image acquired on a particular scanner will suffer the same distortions due to the inherent non-linearity of the *x, y,* and *z* gradient coils. Being independent of sequence parameters, such spatial distortions are not affected by a reversal in read gradient polarity (Figure 3-1), while sequence-dependent spatial distortions are (Figure 3-2).[17,20] Thus, when implemented on an object of known geometry (i.e. a grid phantom containing discrete points), the reverse gradient technique outlined in Chapter 3 provides an effective way to separate sequence-independent and sequence-dependent spatial distortion contributions.[19,21] By taking the average position of grid locations from both forward and reverse gradient images, and by comparing them to the CT grid locations, the sequence-independent spatial distortions can be obtained. Finally, because these distortions arise from gradient non-linearities, they are neither object- nor sequence-dependent. Every image, regardless of the sequence implementation, will be formed using some combination of the gradient coils. Once gradient non-linearities have been

characterized, corrections can be applied to any object imaged under any combination of sequence parameters.

4.2.2. Sequence-dependent spatial distortions

Sequence-dependent spatial distortions arise from field distortions due to inhomogeneities in the main field (ΔB_0), differences in susceptibility (ΔB_χ), and chemical shift (ΔB_{CS}). Thus, they are comprised of both machine- and object-dependent field distortion sources. They will henceforth be collectively referred to as field distortions, ΔB, where $\Delta B = \Delta B_0 + \Delta B_\chi + \Delta B_{CS}$. As illustrated in Figure 3-2 and expressed in Eq. 3-4, the spatial distortions resulting from these field distortions are reversed in direction under gradient polarity reversal. Field distortions, ΔB, therefore result in sequence-dependent spatial distortions. In order to separate gradient non-linearities from sequence-dependent distortions, the reverse gradient method relies on accurate matching of discrete points in both forward and reverse gradient images. While this technique can easily be applied to phantom images, it is much more difficult to implement for patient images where paired image features are not easily identified. Chang and Fitzpatrick used fourth-order Runge-Kutta integration to solve the problem of matching discrete image points[17] while Reinsberg *et al* proposed using mutual-information and cross-correlation based registration of the two reversed gradient image sets.[23]

Apart from the reversed gradient method, sequence-dependent distortions can be determined and corrected using the double echo gradient echo scheme proposed by Jezzard and Balaban.[19] This method generates a field distortion map from which the spatial distortions can be calculated; it requires a single additional scan of interleaved gradient echo images acquired using two different echo times. For standard gradient echo sequences, the phase contributions, ϕ, at the echo time, TE , can be written as:

$$\phi(x, y, z, TE) = 2\pi\gamma \cdot \{\Delta B(x, y, z) \cdot TE\} \qquad \text{Eq. 4-1}$$

where (*x,y,z*) gives the spatial location, γ is the gyromagnetic ratio of hydrogen, and ΔB represents the underlying field distortions. If the phase image is recorded at two different echo times such that $\Delta TE = TE_2 - TE_1$, then the field distortions can be obtained from the unwrapped phase difference map, $\Delta\phi$. That is,

$$\Delta B(x, y, z) = \frac{\Delta\phi(x, y, z, \Delta TE)}{2\pi\gamma\Delta TE} \qquad \text{Eq. 4-2}$$

The field distortion map, ΔB , can be converted to a sequence-dependent spatial distortion map in either pixel shifts or Cartesian coordinate shifts through Eq. 3-2 and can be added to the sequence-independent spatial distortion map.

4.2.3. Geometric Distortion Correction

To rectify image distortion, a complete mapping from distorted coordinates (*x′, y′, z′*) to corrected coordinates (*x, y, z*) is required. That is,

$$x' = x + \Delta x(x, y, z)$$
$$y' = y + \Delta y(x, y, z)$$
$$z' = z + \Delta z(x, y, z) \qquad \text{Eq. 4-3}$$

where $\Delta x(x,y,z)$, $\Delta y(x,y,z)$, and $\Delta z(x,y,z)$ each contain sequence independent contributions (i.e. $\Delta x_{SI}(x,y,z)$) and may contain sequence-dependent contributions (i.e. $\Delta x_{SD}(x,y,z)$) depending upon the particular imaging sequence employed. Therefore, to obtain the full distortion map, both sequence-independent and sequence-dependent distortions must be known.

As discussed in §2.2.4.2, the way in which field distortions, ΔB, affect image distortion depends upon how the image is acquired – hence, the term sequence-dependent spatial distortions. Eq. 2-42 showed that the effect of field distortions could be determined by evaluating the phase evolution in the k_x and k_y directions (i.e. in the frequency encode and phase encode directions, respectively). Furthermore, it showed that in the case of basic 3D gradient or spin echo imaging where one line of *k*-space is filled following each excitation, sequence-dependent spatial distortions are manifest only in the frequency encoding direction. Under ideal conditions, the phase evolution in the frequency encoding direction, $\Delta\phi_{fe}$, is given as:

$$\Delta\phi_{fe} = 2\pi\gamma\left[G_{fe} \cdot r \cdot \Delta t\right] \qquad \text{Eq. 4-4}$$

where G_{fe} is the frequency encoding gradient strength, r is the generalized direction of frequency encoding and Δt is the time between subsequent

digitizations (i.e 1/bandwidth). However, because of inherent field inhomogeneities, ΔB, additional phase is accumulated such that Eq. 4-4 must be rewritten as:

$$\begin{aligned} \Delta\phi_{fe} &= 2\pi\gamma\left[G_{fe}\cdot r\cdot\Delta t+\Delta B\Delta t\right] \\ \Delta\phi_{fe} &= 2\pi\gamma\cdot G_{fe}\Delta t\left[r+\Delta B/G_{fe}\right] \end{aligned} \qquad \text{Eq. 4-5}$$

It is the last term in Eq. 4-5 that gives rise to the spatial mispositioning in the frequency encode direction:

$$r' = r + \Delta r_{SD} \qquad and\ \Delta r_{SD} = \Delta B / G_{fe} \qquad \text{Eq. 4-6}$$

where r' is the distorted position, r is the true position, and Δr_{SD} is the sequence-dependent spatial distortion. From Eq. 4-6, it can be seen that the sequence dependent distortion, Δr_{SD}, caused by the field distortions, ΔB, scales inversely with the strength of the read gradient. If we reintroduce the sequence-independent spatial distortions, we can express the total distortion transformation for a 3D SE or GE image as

$$\begin{aligned} r' &= r + \Delta r_{SD} + \Delta r_{SI} && (frequency\ encode\ \ direction, i.e.\ x) \\ r' &= r + \Delta r_{SI} && (phase\ encode\ \ direction, i.e.\ y) \\ r' &= r + \Delta r_{SI} && (partition\ encode\ \ direction, i.e.\ z) \end{aligned} \qquad \text{Eq. 4-7}$$

where Δr_{SD} affects only the frequency encode direction, and the terms Δr_{SI} come directly from the phantom-derived gradient non-linearity mapping. If 2D images are acquired instead of a 3D image set, then an equation analogous to the

expression for the frequency encode direction can be written for third direction (i.e. the *z* or slice-select direction).

In the case of echo planar imaging (EPI), all of *k*-space is traversed following a single excitation of the sample. Distortions remain an issue in the frequency encoding direction and are calculated from Eq. 4-6; however, because of the very large read gradient that is needed in order to fill all of *k*-space following a single excitation, distortions in the frequency encoding direction are minimized. Moreover, because only a single excitation is used, phase evolution due to B_0 inhomogeneity, susceptibility and chemical shift also affect the phase encode direction. If the time between subsequent phase encodes is given as $\Delta t_{pe} = N \cdot \Delta t + 2 \cdot t_{ramp}$, where N is the number of samples in the frequency encoding direction, Δt is the time between subsequent digitizations (again, 1/bandwidth), and t_{ramp} is the ramp time for the switched gradients, then an equation analogous to Eq. 4-5 can be written for the phase evolution between adjacent phase encode steps:

$$\begin{aligned}
\Delta\phi_{pe} &= 2\pi\gamma\left[\Delta G_{pe}\tau \cdot r + \Delta B \cdot \Delta t_{pe}\right] \\
\Delta\phi_{pe} &= 2\pi\gamma\left[\Delta G_{pe}\tau \cdot r + \Delta B\left(N \cdot \Delta t + 2 \cdot t_{ramp}\right)\right] \\
\Delta\phi_{pe} &= 2\pi\gamma \cdot \Delta G_{pe}\tau\left[r + \Delta B\left(N \cdot \Delta t + 2 \cdot t_{ramp}\right)/\left(\Delta G_{pe}\tau\right)\right] \\
\Delta\phi_{pe} &= 2\pi\gamma \cdot \Delta G_{pe}\tau\left[r + \Delta B / \widetilde{G}_{pe}\right]
\end{aligned} \qquad \text{Eq. 4-8}$$

where ΔG_{pe} is the blipped phase encode gradient step size, τ is the duration of the blipped phase encoding gradient, *r* is the generalized phase encode direction, and

$\widetilde{G}_{pe} = \left(\Delta G_{pe}\tau\right)/\left(N \cdot \Delta t + 2 \cdot t_{ramp}\right)$ is the "effective" phase encode gradient in an EPI experiment. Similarly, it is the last term in Eq. 4-8 that gives rise to sequence dependent distortions in the phase encode direction. That is:

$$r' = r + \Delta r_{SD} \qquad where\ \Delta r_{SD} = \Delta B / \widetilde{G}_{pe} \qquad \text{Eq. 4-9}$$

Again, r' is the distorted coordinate, r is the true coordinate, and Δr_{SD} is the sequence-dependent spatial distortion. As in Eq. 4-6, we have ignored the gradient non-linearities. Including both sequence-independent and sequence-dependent distortions, the distortion transformation for an EPI sequence is given as:

$$\begin{aligned} r' &= r + \Delta r_{SD} + \Delta r_{SI} \qquad (frequency\ encode\ \ direction) \\ r' &= r + \Delta r_{SD} + \Delta r_{SI} \qquad (phase\ encode\ \ direction) \end{aligned} \qquad \text{Eq. 4-10}$$

where Δr_{SD} is different for the frequency and phase encode directions and is determined according to Eq. 4-6 and Eq. 4-9, respectively.

From the above equations, it is evident that knowledge of the *k*-space trajectory, (effective) gradient strengths, and a detailed field distortion map, ΔB, are all required for correction of sequence dependent distortions. In summary, sequence-dependent distortions scale with the inverse of the gradient strength; they affect standard spin echo and gradient echo images in the frequency encoding direction(s) only, but affect echo-planar images in both the phase encode and frequency encode directions. Thus, a single field distortion map can be used to calculate several sequence-dependent spatial distortion maps and to correct

multiple images of the same object or anatomy provided that the *k*-space trajectory and gradient strengths of each imaging sequence are known. In contrast, sequence independent distortions affect each image in the same way. When a variety of distortion-corrected images with complementary clinical information are required for tumor delineation and treatment planning purposes,[6] the ability to quickly correct all images with the information provided by a single additional patient scan, (i.e. the field mapping scan), presents an attractive and time-efficient option.

4.2.4. Intensity Correction

Through the transformation from distorted to corrected coordinates (or vice versa), signal intensity arising from a uniform voxel is either compressed or stretched to a voxel of a different size, shape, and location. Therefore images suffer from not only geometric distortions, but also intensity distortion[4,17]. The Jacobian, *J*, describes the localized magnitude of the volume change under the coordinate transformation. Thus, to recover the true image intensity at the true coordinates *i(x, y, z)* from the apparent image intensity at the distorted coordinates *i′ (x′, y′, z′),* we have

$$i(x,y,z) = i'(x',y',z') \cdot J(x,y,z) \qquad \text{Eq. 4-11}$$

where

$$J(x,y,z) = \begin{vmatrix} \partial x'/\partial x & \partial x'/\partial y & \partial x'/\partial z \\ \partial y'/\partial x & \partial y'/\partial y & \partial y'/\partial z \\ \partial z'/\partial x & \partial z'/\partial y & \partial z'/\partial z \end{vmatrix} \qquad \text{Eq. 4-12}$$

In order to calculate the Jacobian, the complete distortion transformation is required (Eq. 4-3), and is obtained through the gradient non-linearity maps, field distortion map, and knowledge of the particular sequence implementation. Partial derivatives of the form $\partial x'/\partial x$, evaluated at the point (x_i, y_j ,z_k), were calculated as finite differences, i.e.

$$\frac{\partial[x'(x_i, y_j, z_k)]}{\partial x} = \frac{x'(x_{i+1}, y_j, z_k) - x'(x_{i-1}, y_j, z_k)}{x_{i+1} - x_{i-1}} \qquad \text{Eq. 4-13}$$

4.3. Methods and Materials

4.3.1. The phantom

The basic 3D grid phantom used in Chapter 3 and described in §3.4.1 was used once again. However, in order to facilitate large field of view measurements, two lateral extensions were built. The same materials – a polymethylmethacrylate case, polystyrene grid sheets, and mineral oil – were used to construct the extensions. With the extensions attached on either side of the basic cubic phantom, the large FOV phantom fills the lateral extent of the magnet's bore – 578 mm – as shown in Figure 4-1. An alignment grid was used to ensure reproducible set up in the MR bore and on the CT couch.

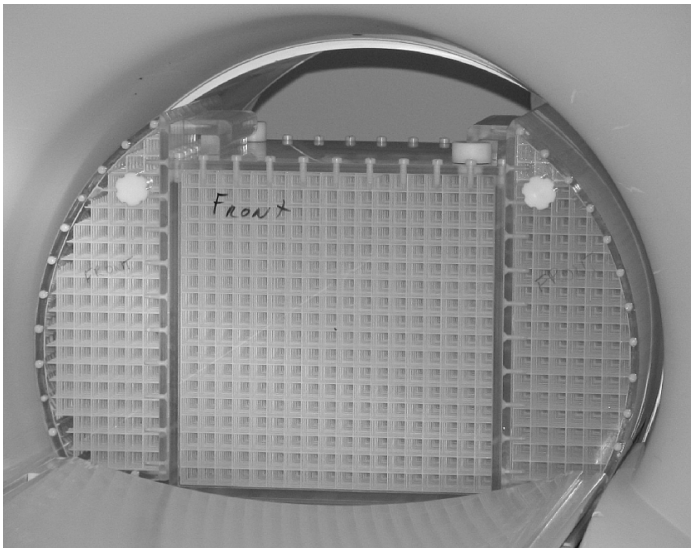

Figure 4-1

The large FOV distortion characterization phantom designed to fill the lateral extent of the Philips 3T Intera bore. Details of the basic phantom design are given in Chapter 3, §3.4.1.

4.3.2. Image Acquisition

MR images were acquired on the 3.0 T Intera MRI scanner (Philips Medical Systems, Cleveland, OH) using the body coil. To determine gradient distortions, the large FOV phantom was scanned using the reverse gradient technique and a 3D gradient echo (GE) sequence with TE, TR and flip angle of 2.01 ms, 8.60 ms, and 28º, respectively. A single *k*-space line was encoded per TR. The image was

acquired using a 530 mm FOV, a 512 x 512 matrix and 440 slices with a slice spacing of 0.72 mm. The *x, y, z* voxel dimensions were thus 1.04 x 1.04 x 0.72 mm^3. Two scans were obtained – the first with a positive read gradient polarity (20.84 mT/m), and the second with a negative read gradient polarity (-20.84 mT/m). In order to define the true, undistorted control point locations, a corresponding CT image was acquired using the Philips Brilliance Big Bore CT scanner (Philips Medical Systems, Cleveland, OH). A 600 mm FOV was used and images were acquired on a 512 x 512 imaging matrix with 614 spiral slices and a reconstructed slice spacing of 0.5 mm. Voxel dimensions were thus 1.17 x 1.17 x 0.5 mm^3. By comparing the average control point locations from the reverse gradient MR scans to the true locations in the CT scan, the spatial distortions due to gradient non-linearities could be separated from those due to the combined effects of B_0 inhomogeneity, susceptibility and chemical shift.

Field distortions were measured using a double echo gradient echo imaging scheme[19] and were used to calculate sequence-dependent spatial distortion maps. After acquiring the double gradient echo phase difference map, the auto shimming, higher order shimming, and resonant frequency (f_0) determination procedures were disabled. This ensures identical imaging conditions for the distortion mapping and anatomical imaging scans. While it is not necessary to disable these procedures entirely, it is imperative that the shimming and f_0 value not be re-calculated for scans acquired for different series during the same imaging session.

For the chemical shift of fat relative to water to be visible in the phase difference map, the ΔTE must be selected such that $\Delta TE \neq n/\Delta f_{fat-water}$, where $\Delta f_{fat-water}$ is the difference in the resonance frequencies of fat and water (428 Hz at 3.0 T [24]). With fat and water not in phase, it is possible to correct for the chemical shift displacement in distorted images. However, when the full distortion map is determined – from which the Jacobian-based intensity correction is calculated – phase discontinuities at fat/water interfaces which arise when $\Delta TE \neq n/\Delta f_{fat-water}$, lead to an ill-defined Jacobian. From Eq. 4-12, the calculation of the Jacobian requires evaluation of the derivative of the distorted coordinate (as a function of the true coordinate). If the distortion field is not smooth (i.e. it is discontinuous, as it is at fat/water boundaries), the Jacobian is undefined. Therefore, an in-phase map (i.e. $\Delta TE = n/\Delta f_{fat-water}$) is better suited for the calculation of the Jacobian since fat/water phase differences are irrelevant. Furthermore, B_0 and susceptibility inhomogeneities lead to distortions that are generally smooth, and derivatives are thus well-defined. Finally, because the chemical shift artifact only results in linearly shifted signal (as opposed to stretched or compressed signal), the distorted image can be accurately corrected for intensity distortions using the Jacobian calculated from the in-phase map. Phase difference maps were typically acquired as a 3D GE sequence with TR/TE/FA = 8.6 ms / 3.3 ms / 28° and an echo time difference, $\Delta TE = 0.6\,\text{ms}$ (fat and water out of phase) or $\Delta TE = 2.3\,\text{ms}$ (fat and water in phase). A phase difference map acquired with the above

parameters on a 256 x 256 x 40 imaging grid adds approximately 2 minutes of additional scan time.

4.3.3. Image Analysis

To determine the large FOV gradient non-linearity data, the MR and CT phantom images were processed using in-house developed Matlab-based software. The method by which control point coordinates were determined was covered in Chapter 3, §3.4.3.

Phase difference maps acquired using the double echo gradient echo imaging sequence were used to calculate sequence-dependent spatial distortion maps. Differences in precessional frequency – arising from variations in magnetic field strength (susceptibility or B_0 inhomogeneities) or from differences in Larmor frequency (fat and water) – lead to phase evolution over time, as shown by Eq. (1). The phase difference map is phase-wrapped with pixel values in the $[-\pi, \pi]$ range. In order to calculate the field distortions and, hence, the sequence-dependent spatial distortions, it is therefore necessary to unwrap the phase difference map as an initial step. This was done using in-house developed Matlab-based software and a robust unwrapping technique.[25] The method presented by Cusack *et al* was extended to operate in 3D – this augmentation added considerable processing time, but had the added advantage of increasing the robustness of the unwrapping method; unwrapping errors are extremely rare.

3D Phase unwrapping can take between 30 minutes and a few hours, but does not add to patient scanning time since it is carried out after the imaging session. The resulting 3D unwrapped phase difference map was used to calculate the field distortion map, ΔB , using Eq. 4-2.

4.3.4. Distortion Correction

Because several images of an object or patient may be collected during one imaging session, it is advantageous to be able to correct each image for distortion. As mentioned, field distortions, ΔB, lead to sequence-dependent spatial distortions which depend on both the particular *k*-space trajectory of the imaging sequence and the selected gradient strengths. Field distortion maps were scaled according to Eq. 4-6 and/or Eq. 4-9 to provide as many sequence-dependent spatial distortion maps as required. It should be noted, however, that these distortion maps are subject to their own distortions; that is, they are collected in distorted image space. Because of the high read gradient strengths used to acquire the phase difference maps, their sequence-dependent spatial distortions are minimal (usually less than 1 pixel); nevertheless, both sequence-independent and sequence-dependent distortions are first corrected such that the final sequence-dependent distortion maps are given in undistorted image space.

The mapping of distorted to corrected image coordinates is accomplished by combining the phantom-based sequence-independent distortion map with the

object- or patient-based sequence-dependent spatial distortion map. If necessary, the two distortion maps are interpolated to the same resolution and orientation as the image for which distortion correction is required. Thus, a pixel-to-pixel mapping of distorted and corrected coordinates is produced. Image correction then amounts to the simple task of 3D interpolation which is carried out in Matlab. This method of distortion correction differs from the method used in Chapter 3 (image warping with the Elastic Body Spline (EBS) kernel); instead of warping the distorted image into the corrected image space through a select number of control points (17 x 17 = 289 / per slice using the EBS method in Chapter 3), this method allows each pixel to be an effective control point (i.e. 512 x 512 = 262,144 / per slice). Thus, much smaller scale image distortions can be handled. As a final step, the image intensities are corrected through calculation and application of the Jacobian scaling factor. This is easily calculated based on the final 3D distortion map according to Eq. 4-12.

4.4. Results

The full distortion correction technique was benchmarked using a variety of phantoms, each designed to measure and/or illustrate a particular type of distortion. First, gradient non-linearities were mapped using the large FOV phantom based on both MR and CT images of the phantom. Corresponding MR and CT images are shown in Figure 4-2. Severe distortion is visible near the image edges; in fact, the full lateral extent of the phantom could not be imaged in

MR due to extreme inhomogeneities near the edge of the bore which result in rapid intra-voxel dephasing. Gradient distortions were mapped over a 440 x 265 x 87 mm^3 region and were observed to increase rapidly with increasing distance from the magnet's isocenter. Peak-to-peak distortions from gradient non-linearities in the central portion of the phantom (266 x 266 x 87 mm^3) were 5.4 mm, 5.0 mm, and 1.6 mm (in the *x, y,* and *z* gradients respectively). When gradient non-linearities were measured over the large FOV phantom, the values nearly doubled – to 10.6 mm, 9.8 mm, and 3.1 mm respectively.

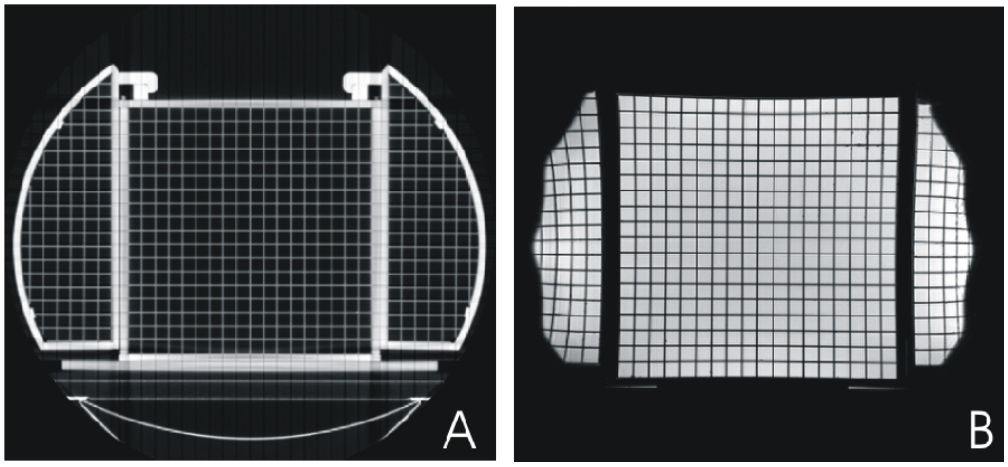

Figure 4-2

A) A transverse CT image of the large FOV grid phantom, and B) the corresponding MR image slice. Imaging FOVs were 600 mm and 530 mm, respectively.

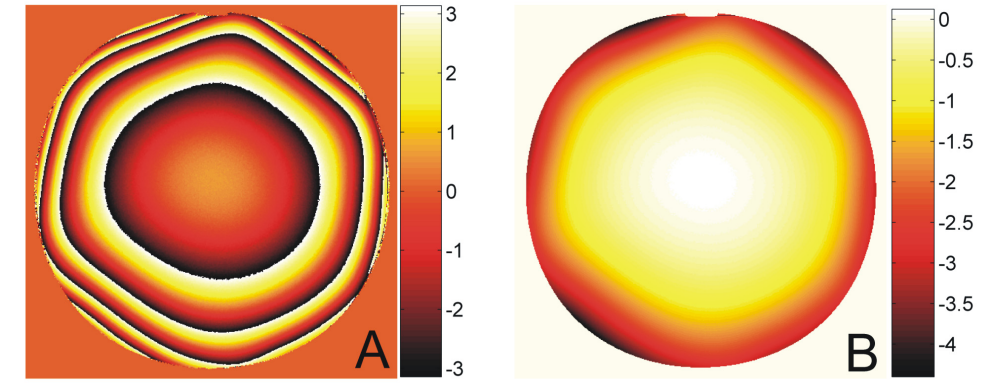

Figure 4-3

(A) A phase difference map for a large (FOV=400mm) uniformity phantom as obtained from the double echo gradient echo imaging sequence with ΔTE = 7 ms and B_0 = 3 T. Phase values are wrapped in the interval [-π, π]; (B) The field distortion map obtained from the unwrapped phase difference map in accordance with Eq. 4-2. Field distortion is displayed in parts per million.

The sequence-dependent distortion mapping procedure was first tested on a large uniformity (flood-field) phantom. Figure 4-3A shows the wrapped phase difference map acquired using the double gradient echo imaging sequence (ΔTE = 7 ms), while Figure 4-3B shows the field distortion map in parts per million calculated from the unwrapped phase difference map. The field distortion map was acquired without any autoshimming and illustrates the good homogeneity of the Philips 3T Intera system over a large central region. The image was acquired

with a 400 mm FOV in a transverse plane through isocenter and peak-to-peak field inhomogeneity does not exceed 5 ppm. The same measurement was performed using the large FOV grid phantom (see Figure 4-1) and similar results were obtained; however, the larger size of the grid phantom allowed field distortion measurements to be taken even further from the isocenter; distortions were seen to increase rapidly with increasing distance from isocenter. Peak-to-peak field inhomogeneity rose to approximately 20 ppm near the edge of the 500 mm FOV image. Previous simulations showed that the difference in grid and oil susceptibility was 0.49 ppm (see § 3.4) and therefore the effect of the grid susceptibility on the B_0 inhomogeneity value of 20 ppm can be considered negligible.

Next, the distortion correction technique was tested on a susceptibility phantom as shown in Figure 4-4. The central cylindrical portion (2.8 cm diameter) is open to the air while the surrounding volume (8.2 cm diameter) is filled with water. Because of the large difference in magnetic susceptibility values for air and water – χ_{water} = -9.05 ppm, χ_{air} = 0.36 ppm[26] – strong magnetic field gradients are generated and distortions near air/tissue interfaces often represent a worst case scenario in clinical images. The susceptibility phantom was thus designed to simulate these interfaces (as in the sinuses or bowels) and to provide a means of evaluating the distortion measurement and correction technique under such simplified imaging conditions.

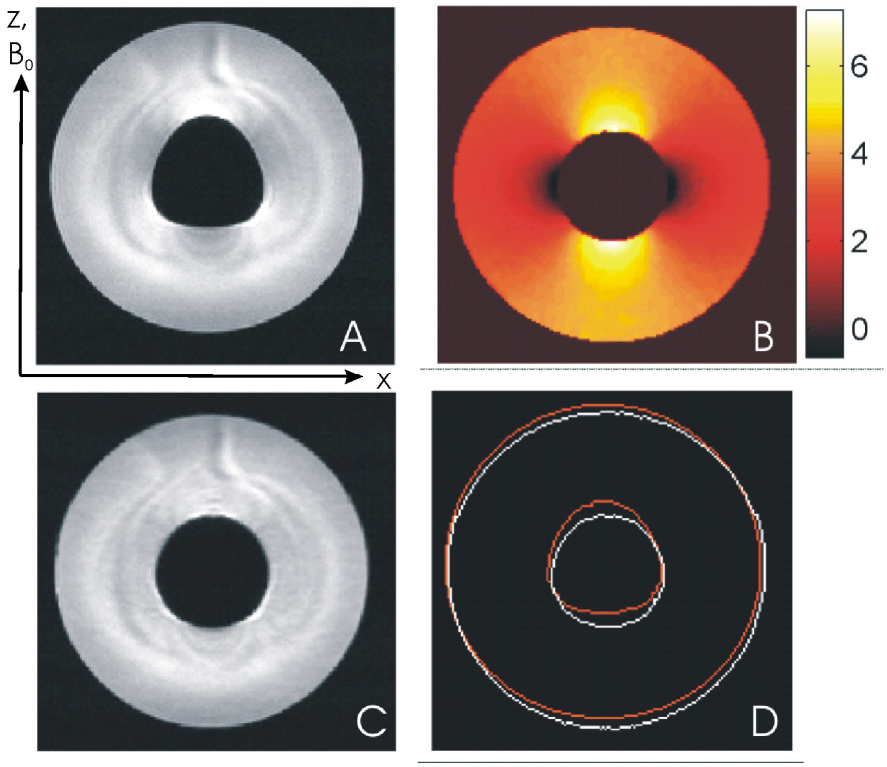

Figure 4-4

An cylindrically symmetric air/water phantom illustrates susceptibility artefacts; the background field, B_0 is aligned with the z direction. (A) Original distorted image acquired using a 5.4 mT/m frequency encode gradient. The central circular tube is distorted in the vertical (frequency encode) direction. (B) The field distortion map in ppm. (C) The corrected image shows good restoration of the circular shape. (D) Edge images for the original and corrected phantom images.

Coronal images were acquired using a low read gradient strength (5.4 mT/m); a single slice is shown in Figure 4-4A. The field distortion was measured using the double gradient echo sequence (ΔTE = 0.6 ms) and a larger read gradient strength (20.6 mT/m) and is shown in Figure 4-4B in parts per million. From the field distortion map, sequence-dependent spatial distortions were calculated; distortions of up to 7 pixels exist in the frequency encoding direction (vertical) in Figure 4-4A where the circular shape of the central air tube is distorted into an arrowhead shape. The full spatial distortion map for the image of Figure 4-4A was generated by scaling the sequence-dependent spatial distortion map and combining it with the sequence-independent distortions (gradient non-linearity maps) obtained from the large FOV phantom. The circular nature of the central air tube is very well represented in the corrected image shown in Figure 4-4C. For improved visualization of the effect of the distortion correction procedure, an edge function was used to highlight the basic shapes present in the original and corrected images; this is shown in Figure 4-4D.

After testing the distortion measurement and correction scheme on the susceptibility phantom, it was implemented on a fat/water phantom, as illustrated in Figure 4-5. The main chamber of the phantom contains water on the bottom and mineral oil on the top; the central chamber contains oil as well as several smaller chambers of water. The field distortion map obtained from the double gradient echo phase difference mapping sequence is shown (in parts per million) in Figure 4-5B. While Jezzard and Balaban[19] suggest choosing an echo time

difference such that $\Delta TE = n / \Delta f_{fat-water}$ ($\Delta f = 428$ Hz at 3T so $\Delta t = n \cdot 2.34$ ms)[24] in order to avoid chemical shift artifacts in the field map, we have chosen a shorter echo time difference – $\Delta t = 0.6$ ms – so that fat and water are out of phase. Thus, the field distortion map contains information about not only susceptibility and B_0 distortions, but also chemical shift boundaries, and all three types of distortion can be corrected. Again, the distorted image was corrected by combining the sequence-dependent spatial distortions (calculated from the field distortion map) with the gradient non-linearity data. Because the fat/water boundaries result in discontinuities in the distortion map, the Jacobian, which is based on derivatives, is not well-behaved. Thus, either a second field distortion map can be acquired with fat and water in-phase and used for the Jacobian calculation, or the distortion map can be post-processed to remove the constant offset chemical shift distortions before the Jacobian is calculated. In this case, two field distortion maps were obtained – the first, with $\Delta t = 0.60\ ms$, was used for distortion correction (pixel interpolation), and the second, with $\Delta t = 2.34\ ms$, was used for calculating the Jacobian. As previously mentioned (§ 4.3.2), removing chemical shift information from the phase difference map (i.e. by choosing $\Delta t = 2.34\ ms$), does not degrade the efficacy of the Jacobian correction. Chemical shift results only in displacement of the fat signal relative to the water signal; there is no change in the effective voxel size and thus image intensities are not altered

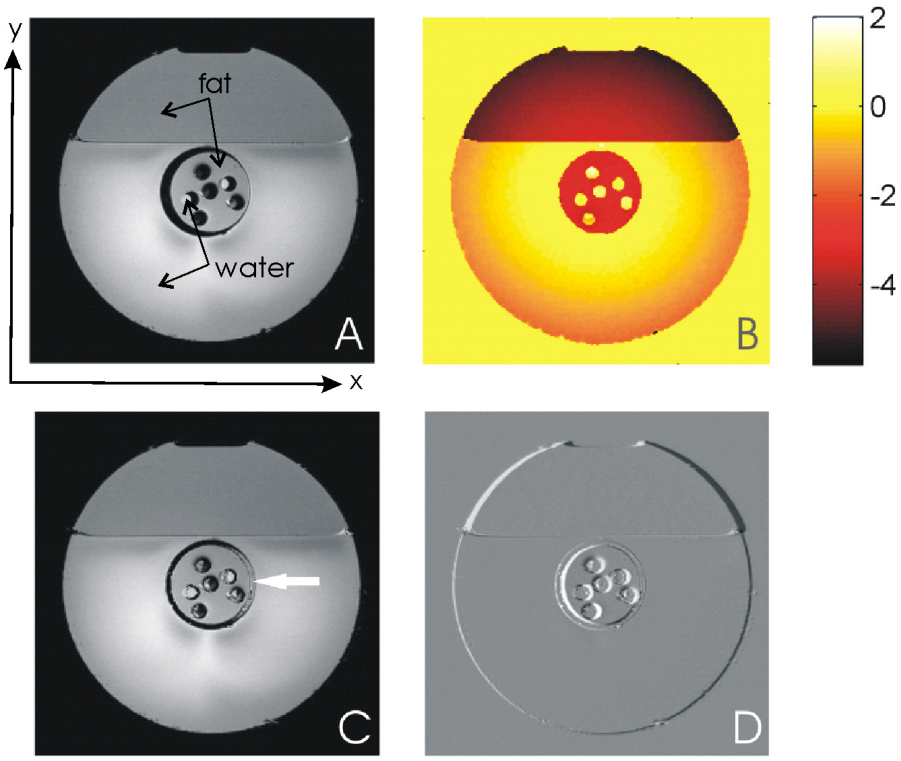

Figure 4-5

(A) A GE image of the fat/water phantom clearly shows the chemical shift artifact. Regions containing fat (mineral oil) are shifted to the right with respect to regions containing water. The fat shift direction coincides with the direction of frequency encoding. (B) The field distortion map for the fat/water phantom in parts per million. The oil-filled regions (top and large central chamber) are visibly demarcated from water-filled regions (bottom and small central chambers) by the constant offset in ppm. (C) The distortion-corrected image shows better alignment of the oil and water chambers; however, distortion cannot be fully corrected where distortion mapping was not one-to-one (white arrow). (D) A difference map for the original and corrected image.

Original and corrected images are shown in Figure 4-5A and Figure 4-5C respectively, and the difference map is shown in Figure 4-5D. Both the central chamber and the oil-filled top section of the phantom are shifted to their correct positions in the rectified image. Limitations of the method can be noted, however, in the rectified image where the signal voids surrounding the large central oil chamber and the small central water chambers are not properly represented as signal voids (white arrow). In these regions, the distortion mapping is not one-to-one – that is, signal from more than one pixel gets mapped to a single pixel in the distorted image. Such distortions cannot be fully corrected.

To test the accuracy of the distortion correction scheme, a single field distortion map was obtained for a grid phantom. This was followed by the acquisition of several images, using a variety of sequence parameters. Spin echo, gradient echo and echo planar images were acquired with the 2XY shims mis-set to 20% of their maximal value; imaging parameters are summarized in Table 4-1. A sequence-dependent spatial distortion map was calculated for each of the images based on the field distortion map and the particular imaging parameters (i.e. the combination of the *k*-space traversal information – GE or SE vs. EPI - and the relevant gradient strengths). The sequence-dependent spatial distortion maps were combined with the sequence-independent distortion map and each of the images was corrected. Rectified images and difference maps are shown in Figure 4-6.

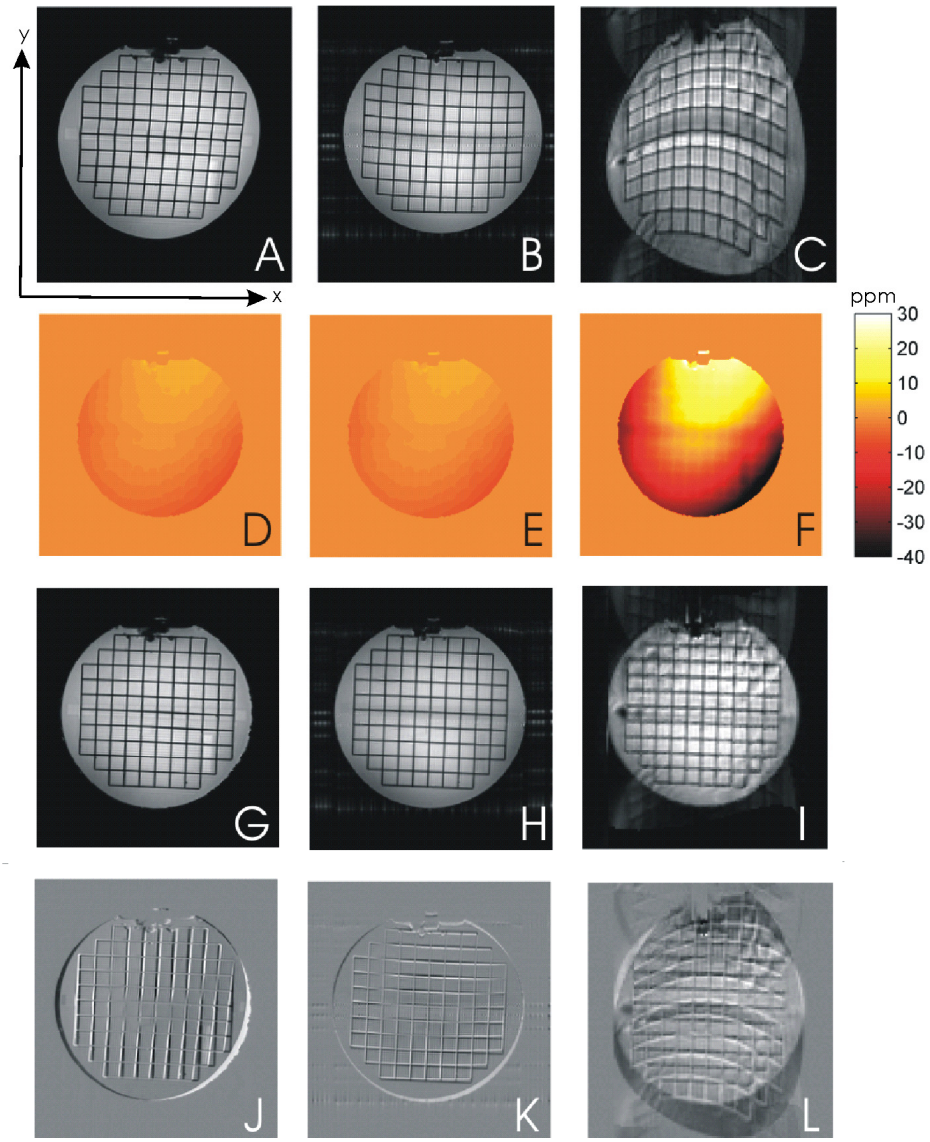

Figure 4-6

Validation of multi-image distortion correction using a grid phantom and a single field distortion map. (A-C) Gradient echo, spin echo, and echo planar images of the grid phantom. (D-F) Sequence-dependent spatial distortion maps for images A-C, shown in millimetres. (G-I) Images shown in A-C corrected for both sequence-dependent and sequence-independent spatial distortions. (J-L) Difference maps for images A/G, B/H, and C/I.

Image	G_{fe} [mT/m]	G_{pe} [mT/m]	Original Distortion [mm]		Residual Distortion [mm]	
			max	mean ± s.d.	max	mean ± s.d.
GE	0.8	n/a	4.4	1.8 ± 1.2	0.6	0.2 ± 0.1
SE	1.0	n/a	3.3	1.3 ± 0.9	0.3	0.2 ± 0.1
EPI	20.9	0.1	23.7	9.9 ± 6.3	3.4	1.2 ± 0.7

Table 4-1

Imaging parameters and validation data for the distortion correction scheme. Note: shims were slightly miss-set to enhance visualization of image distortion. Following distortion correction, maximum and mean distortion were greatly reduced for each of the GE, SE and EPI images.

The original GE, SE and EPI images are shown in the top row [Figure 4-6A - Figure 4-6C]. A single phase difference map was acquired and converted to a field distortion map according to Eq. 4-2; field distortions ranged from -1 ppm to +1 ppm. Individual sequence-specific spatial distortion maps were then calculated based on Eq. 4-6 and Eq. 4-9; these are shown in Figure 4-6D – Figure 4-6F. Total spatial distortions were modest for both the SE and GE images. The locations of the measured control points did not deviate from the true positions by more than 4.4 mm and 3.3 mm, respectively. Mean distortions were about 40% of the maximum distortions. Despite the modest initial distortion, the correction scheme greatly improved the accuracy of the control point locations; maximum residual distortion was reduced to 0.6 mm and 0.3 mm, respectively. An unrelated zipper artifact is observed in the SE image due to temporary RF

interference. Owing to the very low effective bandwidth in the phase encode direction used for the EPI image, spatial distortions were considerably greater. Maximum control point distortion was measured at 23.7 mm while the mean distortion for control points was 9.9 ± 6.3 mm. Even larger distortions are present at the phantom extremities. The ghosting visible in both the original and corrected EPI images arises from the misalignment between even and odd echoes that results from using both polarities of the read gradient to fill the EPI k-space.[14] Visual inspection of the corrected image shows great improvement in geometric accuracy; quantitatively, the maximum and mean distortions were reduced to 3.4 mm and 1.2 ± 0.7 mm, respectively. Although mean distortion in the corrected image is in the range of 1-2 mm, this is still less than the pixel dimensions. Moreover, some of this residual error may be attributed to the poorer image quality of EPI, the increased blur, and hence, the challenge of accurately defining control point locations. Additionally, even very small errors in the sequence dependent distortion map could affect the accuracy of the correction result. For example, an offset of 0.1 ppm could result in a 2 mm offset in the corrected image based on the gradient strength used for this particular sequence.

Finally, the full distortion correction technique was applied to both GE and SE pelvic images of a male volunteer. The large field of view phantom was used to collect gradient non-linearity data over the extent of the bore to facilitate correction of larger image sets (as for pelvic imaging), or for images acquired on anatomy near the edge of the bore (as is often the case for sarcomas). Figure 4-7

shows the sequence-independent spatial distortions due to *x, y* and *z* gradient non-linearities (Figure 4-7A – Figure 4-7C) as well as sequence-dependent spatial distortions, original, and difference images for a GE sequence (Figure 4-7D – Figure 4-7F), and for a SE sequence (Figure 4-7G – Figure 4-7I). The anatomical GE and SE images were acquired with a 400 x 250 x 120 mm^3 FOV, and an acquisition matrix of 256 x 160 x 24 for the GE image and 256 x 154 x 24 for the SE image. The read and slice select gradients for the GE image were 3.3 mT/m and 2.5 mT/m, respectively; for the SE image they were 2.0 mT/m and 2.5 mT/m, respectively. The phase difference maps were acquired as 3D GE sequences using the same FOV. An echo time difference of 0.6 ms was used in order to provide information about chemical shift artifacts. The phase unwrapping took 1 hour and there were no apparent unwrapping errors throughout the imaged volume. Sequence-independent spatial distortions were limited to [-2 mm, 2 mm] over the patient volume, while sequence-dependent spatial distortions fell within the range [-6 mm, 5 mm] for the GE sequence and [-10 mm, 8 mm] for the SE sequence.

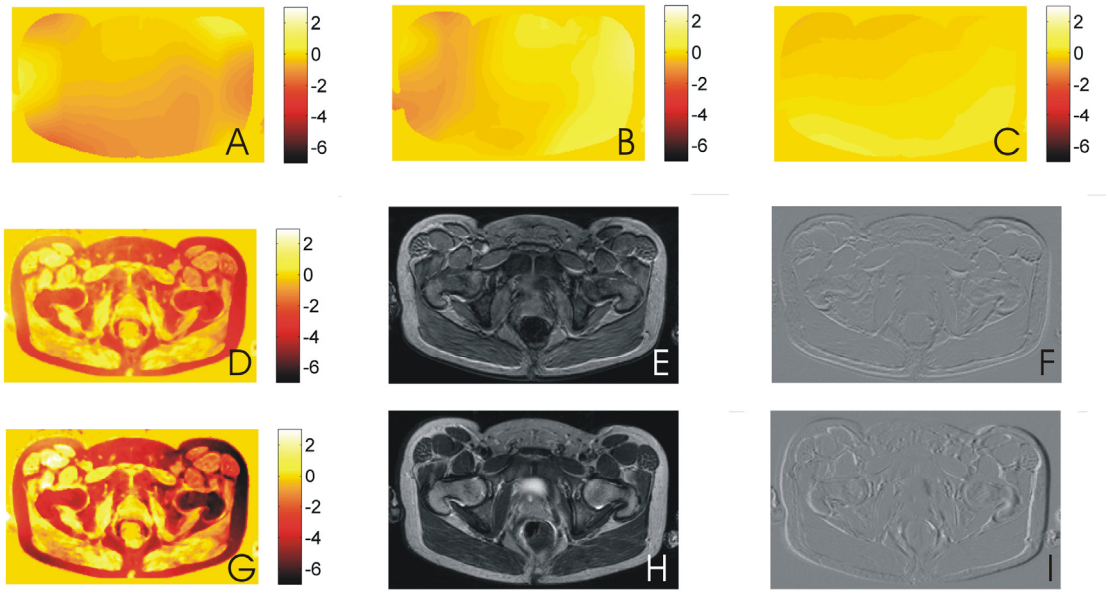

Figure 4-7

Distortion correction for GE images (D-E) and SE images (G-I) of a male volunteer. (A) *x*-gradient non-linearity distortions (mm). (B) *y*-gradient non-linearity distortions (mm). (C) *z*-gradient non-linearity distortions (mm). (D) sequence-dependent spatial distortions (mm) for the GE sequence. (E) original GE image. (F) difference map (corrected – original). (G) sequence-dependent distortions (mm) for the SE sequence. (H) original SE image. (I) difference map (corrected – original).

4.5. Discussion

The large FOV phantom provides gradient non-linearity (sequence-independent spatial distortion) data over the full imaging extent of the 3 T Intera bore. It is at the edges of large fields of view where distortion correction is most needed and,

consequently, where the largest effect of distortion correction techniques will be observed. Although tumor volumes may not be located near the bore's periphery, patient outlines often will be. For effective dose calculation in the radiation treatment planning process, correct patient outlines are imperative.

Phase difference mapping was used to measure field distortions due to B_0 inhomogeneities, susceptibility differences, and chemical shift artifacts. From the field distortion map, sequence-dependent spatial distortions were calculated; they were combined with gradient non-linearity data obtained from reverse gradient images of the large FOV phantom to provide full 3D distortion correction maps for each image. The technique was implemented on a variety of phantoms, each designed to focus on a particular type of distortion. Although the technique cannot fully correct for distortions which are not one-to-one (i.e. where signal from 2 distinct locations are mapped to a single voxel), it proved very effective under a variety of circumstances including large susceptibility differences, inhomogeneous field conditions, and very low gradient strengths.

Phase difference mapping as a means of calculating sequence-specific spatial distortions has a number of advantages over the reverse gradient technique. Although good results can be obtained using gradient reversal, matching corresponding image features in both images is a non-trivial task and is subject to propagating errors based on incorrect initialization of image boundaries.[17] While an additional scan is still required for phase difference mapping, the length of the

scan is typically quite short, and the single scan of a few minutes can be used to correct a variety of images for the same patient. It is assumed that no patient motion occurs between the acquisition of the phase difference map and the images for which distortion correction is required. It is unlikely that this condition is strictly met; however, radiation treatment is typically carried out with the aid of treatment shells which may reduce the likelihood of significant movement. To date, much of the MRI distortion correction literature has been devoted to correction of EPI distortions arising from B_0 inhomogeneities. Several interesting techniques including phase labeling[27,28] and phase evolution rewinding[15] may provide interesting alternatives to the spatial domain correction of sequence-dependent distortions shown here, but none of these techniques take into consideration sequence-independent distortion corrections (gradient non-linearity) which remain an issue for treatment planning purposes. Furthermore, residual distortion following image correction is rarely quantified. In order to use MR images for radiation treatment planning, full distortion correction must be carried out and minimal residual distortion must be confirmed.

4.6. Conclusions

In summary, a procedure for comprehensive distortion correction of clinical MR images has been presented. Correction combines gradient non-linearity data obtained from phantom measurements using the reverse gradient technique with

sequence-dependent spatial distortion maps obtained from a single 3D phase difference mapping image. Total patient scan time is typically increased by approximately 4 minutes and a variety of distortion corrected images can be obtained. The technique was validated on phantoms and then implemented on images of a patient volunteer. While the amount of distortion present in patient images can vary widely, distortion can generally be reduced to within the sub-pixel range.

4.7. References

[1] M. Debois, R. Oyen, F. Maes, G. Verswijvel, G. Gatti, H. Bosmans, M. Feron, E. Bellon, G. Kutcher, H. Van Poppel, and L. Vanuytsel, "The contribution of magnetic resonance imaging to the three-dimensional treatment planning of localized prostate cancer," Int J Radiat Oncol Biol Phys **45,** 857-865 (1999).

[2] R. C. Krempien, K. Schubert, D. Zierhut, M. C. Steckner, M. Treiber, W. Harms, U. Mende, D. Latz, M. Wannenmacher, and F. Wenz, "Open low-field magnetic resonance imaging in radiation therapy treatment planning," Int J Radiat Oncol Biol Phys **53,** 1350-1360 (2002).

[3] M. Breeuwer, M. Holden, and W. Zylka, "Detection and correction of geometric distortion in 3D MR images," Proceedings of SPIE **4322,** 1110-1120 (2001).

[4] S. J. Doran, E. M. Charles-Edwards, S. A. Reinsberg, and M. O. Leach, "A complete distortion correction for MR images: I. Gradient warp correction," Physics in Medicine and Biology **50,** 1343-1361 (2005).

[5] D. Wang, D. M. Doddrell, and G. Cowin, "A novel phantom and method for comprehensive 3-dimensional measurement and correction of geometric distortion in magnetic resonance imaging," Magnetic Resonance Imaging **22,** 529-542 (2004).

[6] B. H. Kristensen, F. J. Laursen, V. Logager, P. F. Geertsen, and A. Krarup-Hansen, "Dosimetric and geometric evaluation of an open low-field magnetic resonance simulator for radiotherapy treatment planning of brain tumours," Radiother Oncol **87,** 100-109 (2008).

[7] L. Chen, T. B. Nguyen, E. Jones, Z. Chen, W. Luo, L. Wang, R. A. Price, Jr., A. Pollack, and C. M. Ma, "Magnetic resonance-based treatment planning for prostate intensity-modulated radiotherapy: creation of digitally reconstructed radiographs," Int J Radiat Oncol Biol Phys **68,** 903-911 (2007).

[8] L. Chen, R. A. Price, Jr., T. B. Nguyen, L. Wang, J. S. Li, L. Qin, M. Ding, E. Palacio, C. M. Ma, and A. Pollack, "Dosimetric evaluation of MRI-based treatment planning for prostate cancer," Phys Med Biol **49,** 5157-5170 (2004).

[9] L. Chen, R. A. Price, Jr., L. Wang, J. Li, L. Qin, S. McNeeley, C. M. Ma, G. M. Freedman, and A. Pollack, "MRI-based treatment planning for radiotherapy: dosimetric verification for prostate IMRT," Int J Radiat Oncol Biol Phys **60,** 636-647 (2004).

[10] T. Mizowaki, N. Araki, Y. Nagata, Y. Negoro, T. Aoki, and M. Hiraoka, "The use of a permanent magnetic resonance imaging system for radiotherapy treatment planning of bone metastases," Int J Radiat Oncol Biol Phys **49,** 605-611 (2001).

[11] R. Prabhakar, P. K. Julka, T. Ganesh, A. Munshi, R. C. Joshi, and G. K. Rath, "Feasibility of using MRI alone for 3D radiation treatment planning in brain tumors," Jpn J Clin Oncol **37,** 405-411 (2007).

[12] T. Stanescu, H.-S. Jans, N. Pervez, P. Stavrev, and B. Fallone, "A study on the magnetic resonance imaging (MRI)-based radiation treatment planning of intracranial lesions," Physics in Medicine and Biology **53,** 3579-3593 (2008).

[13] T. Stanescu, A. Syme, and B. G. Fallone, "MRI-Based Treatment Planning for Radiotherapy of Brain Lesions," Medical Physics **32,** 2033-2033 (2005).

[14] N. K. Chen and A. M. Wyrwicz, "Correction for EPI distortions using multi-echo gradient-echo imaging," Magn Reson Med **41,** 1206-1213 (1999).

[15] Y. M. Kadah and X. Hu, "Simulated phase evolution rewinding (SPHERE): a technique for reducing B0 inhomogeneity effects in MR images," Magn Reson Med **38,** 615-27 (1997).

[16] D. T. Yeo, J. A. Fessler, and B. Kim, "Concurrent correction of geometric distortion and motion using the map-slice-to-volume method in echo-planar imaging," Magn Reson Imaging **26,** 703-14 (2008).

[17] H. Chang and J. M. Fitzpatrick, "A technique for accurate magnetic resonance imaging in the presence of field inhomogeneities," IEEE Trans Med Imaging **11,** 319-329 (1992).

[18] A. S. Jackson, S. A. Reinsberg, S. A. Sohaib, E. M. Charles-Edwards, S. A. Mangar, C. P. South, M. O. Leach, and D. P. Dearnaley, "Distortion-corrected T2 weighted MRI: a novel approach to prostate radiotherapy planning," Br J Radiol **80,** 926-933 (2007).

[19] P. Jezzard and R. S. Balaban, "Correction for geometric distortion in echo planar images from B0 field variations," Magn Reson Med **34,** 65-73 (1995).

[20] L. N. Baldwin, K. Wachowicz, S. D. Thomas, R. Rivest, and B. G. Fallone, "Characterization, predication, and correction of geometric distortion in 3T MR images," Med Phys **34,** 388-399 (2007).

[21] M. A. Moerland, PhD Thesis, University of Utrecht, 1996.

[22] M. A. Moerland, R. Beersma, R. Bhagwandien, H. K. Wijrdeman, and C. J. G. Bakker, "Analysis and correction of geometric distortions in 1.5 T. magnetic resonance images for use in radiotherapy treatment planning," Phys Med Biol **40,** 1651-1664 (1995).

[23] S. A. Reinsberg, S. J. Doran, E. M. Charles-Edwards, and M. O. Leach, "A complete distortion correction for MR images: II. Rectification of static-field inhomogeneities by similarity-based profile mapping," Physics in Medicine and Biology **50,** 2651-2661 (2005).

[24] E. M. Haacke, R. W. Brown, M. R. Thompson, and R. Venkatesan, *Magnetic resonance imaging: physical principles and sequence design* (Wiley-Liss, New York, 1999).

[25] R. Cusack and N. Papadakis, "New robust 3-D phase unwrapping algorithms: application to magnetic field mapping and undistorting echoplanar images," Neuroimage **16,** 754-764 (2002).

[26] J. F. Schenck, "The role of magnetic susceptibility in magnetic resonance imaging: MRI magnetic compatibility of the first and second kinds," Med Phys **23,** 815-850 (1996).

[27] U. Techavipoo, J. Lackey, J. Shi, T. Leist, and S. Lai, "Phase labeling using sensitivity encoding (PLUS): data acquisition and image

reconstruction for geometric distortion correction in EPI," Magn Reson Med **61,** 650-8 (2009).

[28] Q. S. Xiang and F. Q. Ye, "Correction for geometric distortion and N/2 ghosting in EPI by phase labeling for additional coordinate encoding (PLACE)," Magn Reson Med **57,** 731-41 (2007).

5. Chapter 5: Correction of Non One-to-One Distortion: phantom experiments and the fat-shift problem

5.1. Introduction

Magnetic resonance imaging (MRI) is noted not only for its exquisite soft tissue contrast, but also for the ease with which this contrast can be manipulated through alteration of the timing parameters. For these reasons, magnetic resonance (MR) images have been included in the radiotherapy treatment planning process to augment[1-3] or replace[4-6] information provided by computed tomography (CT) images. Unfortunately, MR images are affected by several types of distortion. Contributing to the total distortion field are gradient non-linearities, inhomogeneities in the main B_0 field, variations in tissue susceptibility, and chemical shift differences.[7,8] In general, these contributions lead to a smoothly varying distortion field. However, sharp interfaces between water-based and fat-based tissues lead to discontinuities in the distortion field and hence, non one-to-one mapping between the true signal location and the imaged signal location. Although various techniques for distortion correction have been investigated,[9-14] non one-to-one distortions arising from the chemical shift artifact lead to signal overlap which cannot be reversed using conventional distortion correction techniques. Both hyper- and hypo-intense signal regions are visible near fat/water interfaces in images where chemical shift artifacts are significant. Following distortion correction using the methods described in the previous chapter, the

hypo-intense regions are corrected, but the hyper-intense regions become smeared out along the fat-shift direction; thus residual fat-shift artifacts remain. The region affected by this artifact increases as the B_0 field increases in strength and as the read gradient decreases in strength.

Image distortion caused by fat-shift artifacts is very difficult to correct and therefore a number of different solutions have been proposed. Because the severity of the artifact increases with increasing magnetic field strength, distortion can be reduced by imaging using low field systems.[6,15,16] Alternatively, large receiver bandwidths have been used to minimize chemical shift artifacts.[4] Unfortunately, both these solutions result in deterioration of the signal to noise ratio. Another approach is to avoid imaging fat-based signal altogether. This is achieved through various fat suppression techniques, including selective excitation of the water signal, selective suppression of the fat signal (through pre-saturation), and inversion recovery. With no fat-based signal in the image, chemical shift distortions are avoided entirely.

In some situations, however, it may be preferable to retain fat-based signal in the image and thus the chemical shift artifact is unavoidable. For example, when Zhang *et al* compared various MRI sequences performed on a 3T magnet for accuracy in the diagnosis, staging and planning for rectal carcinoma, they reported that lesions were more clearly depicted on sequences without fat suppression than on those with fat suppression.[17] The high signal intensity of the fatty tissue

surrounding the rectum provided better contrast when compared to the low signal intensity of the tumour tissue. Fat suppression techniques should also be avoided when imaging a particular type of renal carcinoma, angiomyolipoma. Such tumours are composed of a combination of fat, smooth muscle and blood vessels and their diagnosis is dependent upon the detection of macroscopic fat within the tumour mass.[18,19] In fact, fat-shift artifacts, along with in-phase and opposed-phase images are often used to assist in diagnosis of these tumours.[18-20]

The distortion correction technique presented in Chapter 4 requires the acquisition of three images: the (distorted) treatment planning image, a phase difference map in which fat and water are in phase, and a phase difference map in which they are not in phase. Here we propose a method to remove the residual effects of the non one-to-one distortion mapping introduced by the chemical shift artifact; it does not require the acquisition of any additional images beyond the three images previously described. Instead, a number of pre-processing steps are introduced and carried out prior to the standard distortion correction procedure. The post-processing fat-shift correction method is successfully demonstrated on a phantom containing abutting fat and water compartments.

5.2. Theory

Consider the schematic drawing in Figure 5-1 where adjacent pixels contain signal from water and fat. In the absence of a localizing magnetic field gradient, adjacent pixels experience different local magnetic fields due to the chemical shift

effect. At 3 T, the difference in resonance frequency, Δf_{fw}, is ~428 Hz[21]. If the image is acquired using a readout bandwidth of 428 Hz/pixel, the two leftmost pixels experience the same resonance frequency and are thus assigned to the same location in space. In the distorted image, the leftmost pixel, 1′, contains the sum of the signal from pixels 1 and 2. The total signal at pixel 1′ can be expressed as

$$s_t = \left| s_f \cdot e^{-i\Delta\varphi_{fw}} + s_w \right| \qquad \text{Eq. 5-1}$$

where s_t is the total signal, s_f is the signal arising from the fat, s_w is the signal arising from the water, and $\Delta\phi_{fw}$ is the phase difference between the fat and water spins. If the fat and water signals are in-phase, they will add constructively, resulting in a hyper-intense signal at pixel 1′, i.e. $s_t = s_f + s_w$. However, if the signals are at opposed phase, they will add destructively and a signal void will be present at pixel 1′, i.e. $s_t = |s_f - s_w|$. For an in-phase image, pixel 1′ therefore appears bright in the distorted image due to the composite fat-water signal, whereas pixel 3′ appears as a signal void because no signal is assigned to this location. Using the standard distortion correction procedure, it is not possible to separate the signal in pixel 1′ into its original fat and water components. Thus, the summed pixel intensity is assigned to the "corrected" pixel locations 1″ and 2″. This leads to the smearing of high signal intensity shown in Figure 5-1 (bottom schematic).

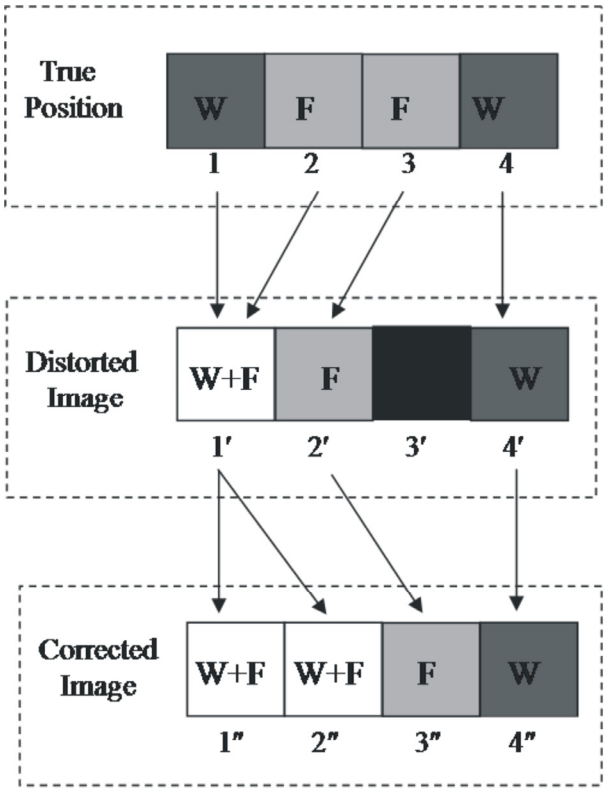

Figure 5-1

A 1D imaging schematic for an image containing both (W)ater- and (F)at-based signal. At 3T, $\Delta f_{fw} = 428\ Hz$, and if the readout bandwidth = 428Hz/pixel, voxel 1′ contains the combined signal from locations 1 and 2. Standard distortion correction procedures cannot resolve the mixed signal at pixel 1′ into its muscle and fat contributions. As a result, the corrected image smears the composite muscle/fat signal into pixels 1″ and 2″.

In a typical MR image, the majority of the signal comes from either water- or fat-based tissues. As such, one can consider the MR image to be a composite of two images: a water image and a fat image. The fat image is always shifted with respect to the water image as a result of the difference in resonance frequencies. In order to correct for the smearing out of the high-intensity overlap signal that

results from the non one-to-one distortion mapping near chemical shift interfaces, the fat image can first be shifted with respect to the water image. Furthermore, pixels containing overlapped signal can be separated into fat- and water-based contributions (as per Eq. 5-1) with only the fat-based contributions being shifted. Once the fat image has been shifted, the standard distortion correction procedure can be carried out.

5.3. Methods

5.3.1. Overlap mask determination

The pixels containing overlapped signal intensities in the distorted image must first be identified. A so-called overlap mask is created by analysing the distortion map for the particular imaging sequence in question. Along with distortions due to B_0 inhomogeneities and susceptibility effects, the chemical shift artifact is always present in the frequency encoding direction for standard Cartesian imaging protocols. As in Chapter 4, phase difference mapping is used to measure the sequence-dependent distortions and is acquired with a very high read gradient in order to minimize distortion (and non one-to-one mapping. The phase difference map in which fat and water are not in phase is then converted to a distortion map (in millimeters), and is added to the previously measured gradient non-linearity distortions in the direction corresponding to frequency encoding for the image requiring distortion correction. If, for example, frequency encoding is carried out in the x direction, this summed distortion map gives the relationship between the

true location, x, and the distorted (imaged) location, x'. This is also expressed in Eq. 3-3 and is illustrated in Figure 5-2 below. Where the mapping between x and x' is not unique, the distorted image will contain overlapped signal.

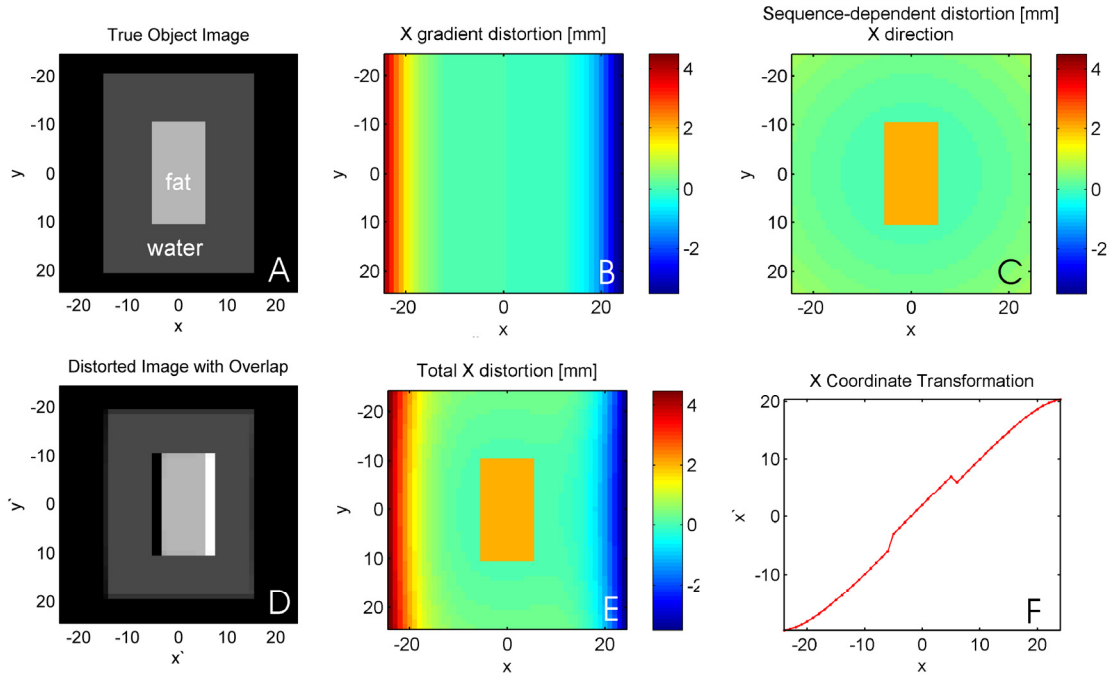

Figure 5-2

A) Simulated object with fat and water compartments; B) Simulated gradient nonlinearities; C) Simulated sequence-dependent distortions with fat and water not in phase (i.e. central portion) and increasing B_0 inhomogeneity near the edges of the FOV; D) Simulated image of the object displayed in A. Both hyper- and hypo-intense regions are seen as a result of the fat shift; E)Total distortion in the x (FE) direction; F) Coordinate transformation obtained using the total distortions at $y = 0$ in image E. Since $x' = x + dx$, x' can be plotted as a function of x. Note the non one-to-one coordinate mapping at $x \sim 6$.

In-house developed, Matlab-based software is used to analyse the distortion map and determine locations of discontinuity in order to create an overlap mask, M_O. As illustrated in Figure 5-3, a horizontal profile through the total distortion map in the FE direction (Figure 5-2E) is used to generate a plot relating the true and distorted coordinates, x and x'. A small portion of this plot is enlarged in Figure 5-3B to better illustrate the locations of non one-to-one mapping. Because of the fat shift distortion, signal imaged at $x' = 6$ is comprised of signal located at both $x = 5$ and $x = 7$. Likewise, signal imaged at $x' = 7$ is comprised of signal located at both $x = 6$ and $x = 8$. Thus, pixels $x' = 6$ and $x' = 7$ contain overlapped signal. This process is repeated for each value of y until the full 2D overlap map, M_O, is created (Figure 5-3C).

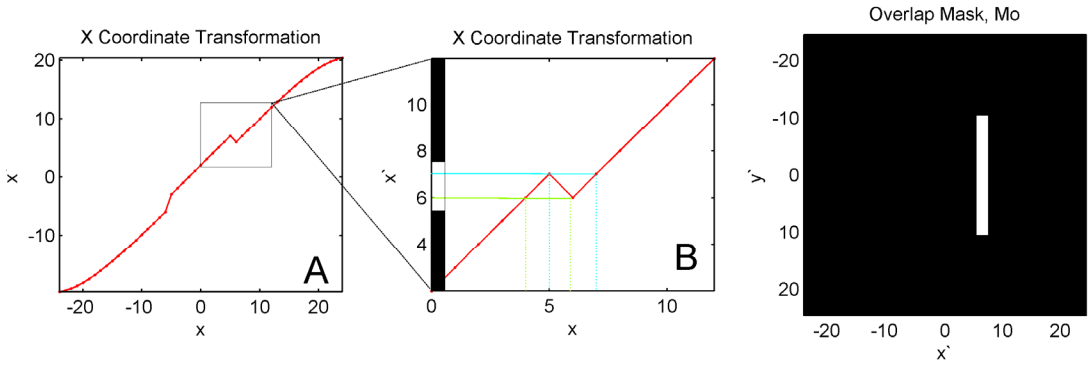

Figure 5-3

A) Coordinate transformation ($x \rightarrow x'$) obtained using the total distortions at $y = 0$ from Figure 5-2 E; B) An enlarged version of image A which better illustrates the non one-to-one mapping which results in overlapped signal at x'=6 and x'=7; C) The full 2D overlap mask, M_O, obtained for the simulated image shown in Figure 5-2.

Next, a portion of the distorted containing fat only is sampled and the mean fat signal intensity, s_f, is determined. If fat and water are in-phase in the distorted image (i.e. adding constructively when occupying the same voxel), then the total signal at the overlapped locations is easily separated into a fat portion and a water portion since both the total signal, s_t, and the fat signal, s_f, contributions are known and $s_t = s_f + s_w$. If fat and water are not in phase, their relative phase must be determined (where $\Delta\phi_{fw} = \Delta f_{fw} \cdot TE$) so that the fat and water contributions can be determined from Eq. 5-1.

5.3.2. Fat mask determination

To shift the fat portion of the distorted image, all fat-containing image pixels must first be identified. This is accomplished through the creation of a fat mask, M_F, which can be calculated from both the in-phase and not-in-phase phase difference maps acquired for the standard distortion correction procedure. The not-in-phase map contains information about phase evolution during the time, ΔTE, due to underlying B_0 inhomogeneities, susceptibility contributions and the difference in fat and water resonance frequencies. The in-phase map contains information due to B_0 and susceptibility effects only since the ΔTE is chosen such that fat and water signals are in phase. When both phase maps are unwrapped and converted into magnetic field maps[9] (Eq. 4-2), the in-phase map can be subtracted from the not-in-phase map such that their difference contains information due to chemical shift effects only. If the difference map is given in ppm, the regions containing no fat will be valued at 0 ppm, whereas those containing fat will be valued at approximately 3.35 ppm. A threshold can be applied to create a binary mask in which pixels containing ppm values of, for example, ≥3 ppm are labeled with 1 (for fat) and all others are labeled with 0 (for water).

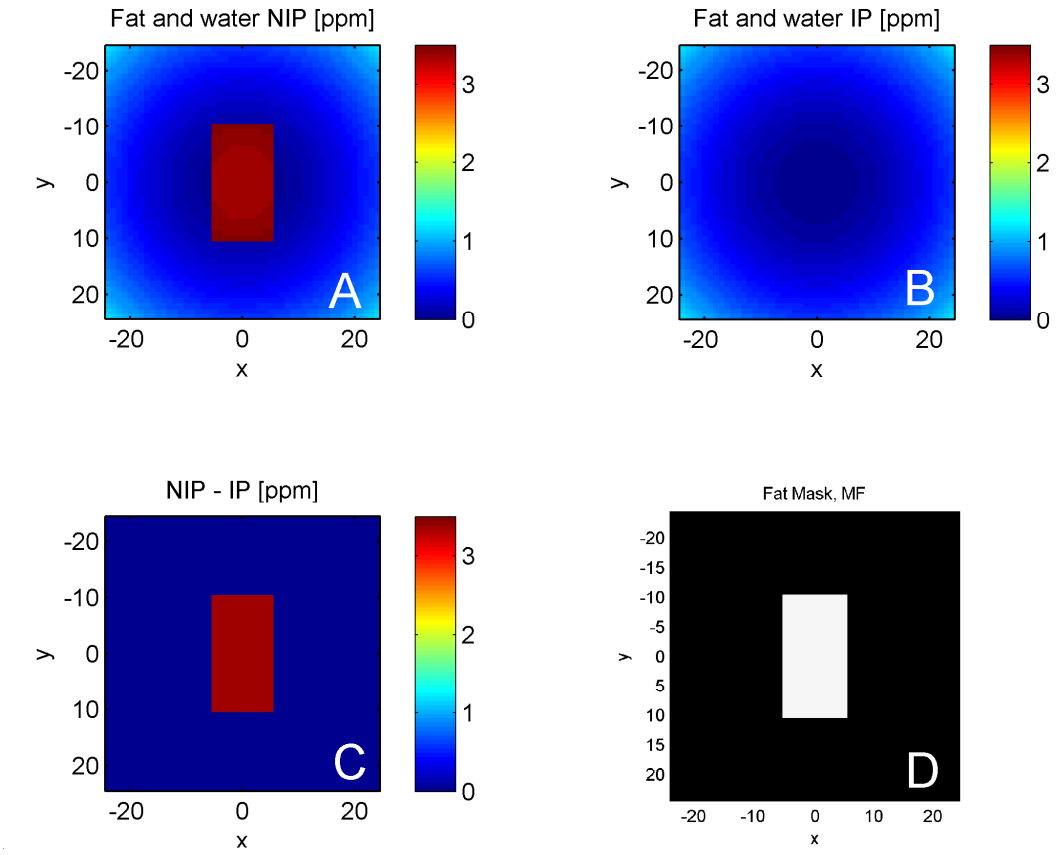

Figure 5-4

A) Sequence-dependent distortion map obtained with fat and water not in phase (NIP), i.e. ΔTE = 0.6 ms B) Sequence-dependent distortion map obtained with fat and water in phase (IP), i.e. ΔTE = 2.34 ms; C) The difference in the two distortion maps highlights the area of chemical shift distortions ($\Delta B_{fat\text{-}water}$ = 3.35 ppm); E) the fat mask, M_F, obtained by applying a threshold (> 3 ppm) to image C.

Obtained in this way, the fat mask locates regions containing fat in the undistorted space (x, y); therefore, in order to locate regions in containing fat in the distorted space (x', y'), the fat mask must itself be distorted. This is easily done by applying

the measured distortion maps in each of the directions to forward distort the fat mask. Once completed, both the overlap mask and fat mask are given in the distorted space.

5.3.3. Fat image shifting

The fat mask identifies the pixels in the distorted image which contain fat while the overlap mask identifies all the pixels which contain overlapped signal. Before the standard distortion correction procedure is carried out, the fat portion of the distorted image must be shifted to its true location. The amount of fat shift, in pixels, is calculated from information contained in the image header as:

$$\Delta p = \frac{\Delta f_{fw}}{\gamma \cdot G \cdot \Delta x} \qquad \text{Eq. 5-2}$$

where Δp is the fat-shift in pixels, Δf_{fw} is the difference in resonance frequency of fat and water (428 Hz at 3T), γ is the gyromagnetic ratio for Hydrogen, G is the read gradient strength (in mT/m), and Δx is the pixel resolution (in millimeters). Thus, all pixels contained in the fat mask, M_F , are shifted by the amount, $-\Delta p$, where the direction of the shift is determined by the direction of the read gradient. For those pixels contained in both M_F and M_O, (i.e. $M_F \cap M_O$), only the fat portion, s_f, of the overlapped signal intensity is shifted. This is illustrated in Figure 5-5.

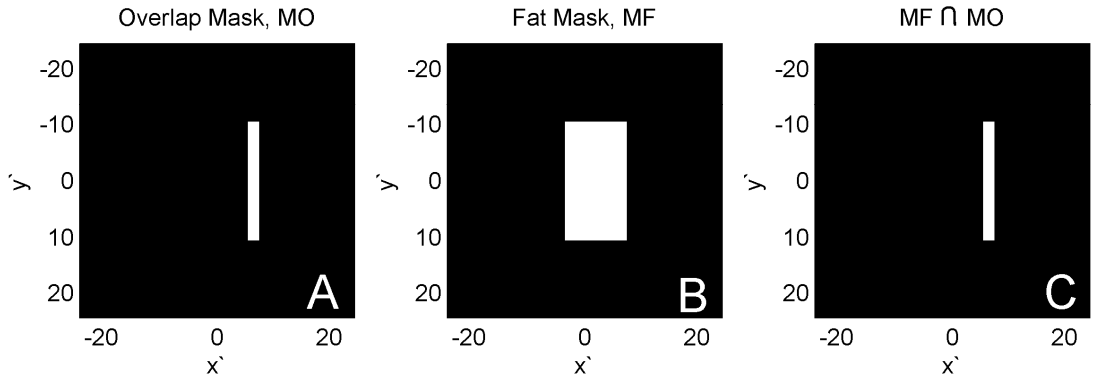

Figure 5-5

A) Overlap map, M_O, in distorted space (x', y'); B) Fat mask, M_F, in distorted space; C) Intersection of M_F and M_O , $M_F \cap M_O$.

5.4. Results

A phantom containing compartments of both mineral oil and water was used to illustrate the fat-shift artifact that frequently hinders clinical images. A distorted image of the phantom is shown in Figure 5-A. The image was acquired with a gradient echo sequence, a read gradient strength of 2.97 mT/m (applied in the x direction), TE = 9.3 ms (such that $\Delta\phi_{fw} = 2\pi \cdot (4)$], a 220 mm FOV, and an image resolution of 256 x 256 pixels. The phantom contains mineral oil in the top third of the phantom as well as in the large central chamber; water is contained in the bottom two-thirds and in the 6 small, central chambers. The chemical shift artifact is visible along the frequency encoding direction as the fat portion of the image is clearly shifted to the right with respect to the water portion of the image. Figure 5-B shows the same phantom after the standard distortion correction

procedure described in Chapter 4 is carried out; the residual artifact – the high signal intensity smear – is indicated by the white arrow.

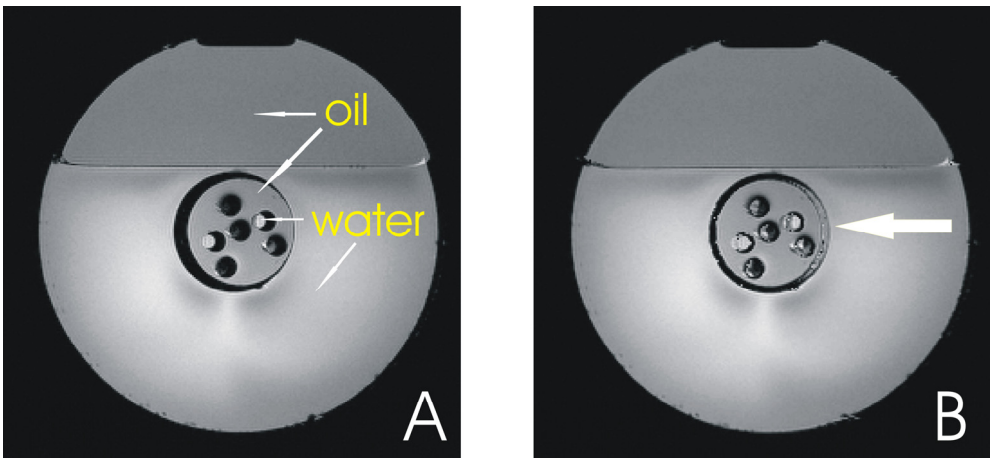

Figure 5-6

(A) a phantom containing water and mineral oil compartments. The fat-based signal (mineral oil) is clearly shifted to the right with respect to the water-based signal. (B) The image with the standard distortion correction procedure applied shows the residual artifact due to high signal intensity smearing.

In addition to the distorted image, two additional phase difference maps (fat/water in-phase [$\Delta TE = 2.34$ ms, $\Delta\phi_{fw} = 2\pi$] and fat/water not in phase [$\Delta TE = 0.60$ ms, $\Delta\phi_{fw} = 2\pi \cdot 0.257$]) were acquired from which magnetic field maps and distortion maps were calculated (Eqs. 4-2 and 3-2). Because frequency encoding was carried out in the x direction, the distortion map calculated from the phase difference map (fat and water not in phase) was added to the x-gradient non-

linearity distortion map to calculate the total distortions along the x direction (Figure 5-). This map was then analysed to create the overlap mask, M_O. The two magnetic field maps derived from the phase difference maps were subtracted and a threshold was applied to create the fat mask for the image. Figure 5- shows the distorted phantom image with the fat and overlap masks overlaid; the region within the fat mask, M_F, is shown in gray, while the intersection of M_F and M_O is shown in white. The fat signal intensity, s_f, was calculated from a 50 x 50 pixel region within the top third of the phantom (Figure 5-A) and was determined to be 546 ± 25. For in-vivo implementation, a similar procedure would be suitable; however, because fat is generally confined to smaller regions in the body than in this idealized phantom, a higher uncertainty in the mean fat signal intensity would be expected.

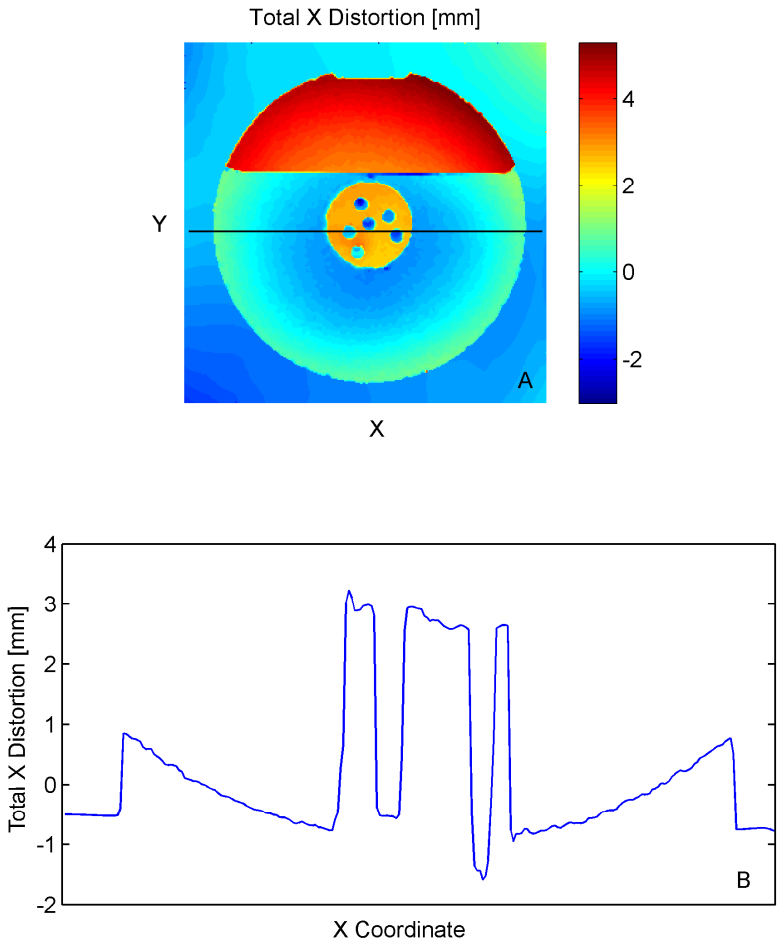

Figure 5-7

(A) Total distortions in the *x* direction for the image shown in Figure 5-A; (B) A profile along the black line shown in (A) highlights the obvious discontinuities in the distortion field. Such profiles are analysed by the Matlab software to label pixels which contain overlapped signal in the distorted image.

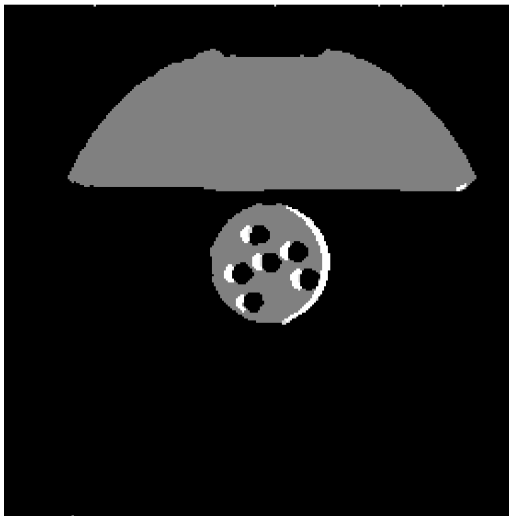

Figure 5-8

Phantom image with the fat mask, M_F , and the overlap mask M_O , overlaid. $M_F - M_O$ is shown in gray, while $M_F \cap M_O$ is shown in white.

The fat shift, Δp, present within the image was calculated from the relevant imaging parameters according to Eq. 5-2 as 3.94 pixels. Thus, the full signal intensity of pixels masked by M_F - M_O (the gray region of Fig. 3) is shifted to the left by 4 pixels, while only a portion of the signal intensity, s_f, is shifted for pixels masked by $M_F \cap M_O$ (white region of Figure 5-). Once the fat image has been shifted to its true location, the standard distortion correction procedure is carried out. Figure 5-A shows a close-up of the central chamber of the distorted phantom; Figure 5-B shows the phantom image with only the standard distortion correction while, for comparison, Figure 5-C shows the corrected image which has been pre-processed according to the methods described above. The smeared out high signal intensity region indicated by the white arrow in Figure 5-B and

again visible in Figure 5-B is not present in Figure 5-C. The pre-processing steps separate the overlapped signal intensity present in the distorted image into its constituent fat- and water-based signals. Only the fat portion of the image was shifted prior to correction for the remaining types of distortion (B_0, gradient non-linearity, and susceptibility).

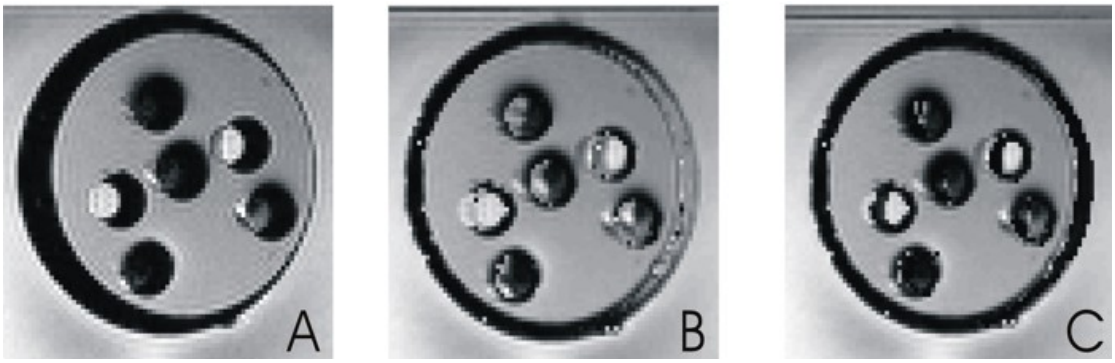

Figure 5-9

A close-up of the central phantom region: (A) original, distorted image; (B) image following standard distortion correction; (C) image with the pre-processing method to reduce residual fat shift artifact.

5.5. Discussion

The image pre-processing steps described here were used in conjunction with the field mapping based distortion correction procedure described in Chapter 4. Full image correction therefore requires the following: (1) previously acquired gradient non-linearity data (obtained, in our case, using the reverse gradient

method employed on grid phantom images); (2) patient-based methods for characterising sequence-dependent distortions - chemical shift effects along with B_0 and susceptibility distortion - (obtained, in our case, through field maps collected both with fat and water in phase and not in phase); and (3) determination of the fat mask and overlap mask and application of the pre-processing steps prior to the standard distortion correction procedure.

As an alternative to using the field mapping approach for correction of sequence-dependent distortions, the reverse gradient technique can also be used. However, this method, as proposed by Chang and Fitzpatrick, is limited by the requirement for a continuous distortion field;[22] thus, like the method we presented in Chapter 4, it cannot be used to fully correct chemical shift distortions. Reinsberg *et al* adapted the technique of Chang and Fitzpatrick and found that the continuous distortion field requirement could be relaxed somewhat when they used an alternative method for pixel pairing in the forward and reverse gradient in-vivo images (they used a mutual information based approach).[13] However, they noted that the technique was only able to cope with chemical shift artifacts when distortion occurred in the vicinity of signal void regions (i.e. bright fat in dark muscle) and could not be applied to non-conventional imaging techniques (i.e. EPI) where the chemical shift artifact is much greater.[13] In theory, the pre-processing method we have proposed can be combined with the field mapping technique and should be able to cope with chemical shift artifacts of any size and in any type of signal region (bright or dark).

Of course, in-vivo implementation is always more complicated than phantom implementation. Successful application for artifact correction in in-vivo images depends upon accurately identifying the region of non one-to-one distortion mapping, which is characterized by an irregular shape, and is generally only a few pixels in width at any given point. If the patient moves at all between the acquisition of the phase difference maps and the treatment planning image, the fat and overlap mask may not accurately correspond to the image undergoing artifact correction. Patient immobilization may be used to reduce instances of patient motion and would undoubtedly assist in successful application of the method in-vivo. Furthermore, the method is likely to be more successfully implemented in regions with little to no internal motion - i.e. brain and appendages. Application for pelvic and thoracic imaging could be difficult and may only be possible by interleaving phase map and treatment planning image acquisitions.

5.6. Conclusions

Although several distortion correction techniques have been described in the literature, full correction of the chemical shift artifact remains problematic. Despite distortion correction, discontinuities in the distortion field prevent complete image correction and residual chemical shift artifacts are apparent as a high intensity smear. Chemical shift artifacts can be partially avoided through various fat suppression techniques, but these methods are not always fully effective and require lengthy acquisition times. Furthermore, there are certain

clinical cases in which inclusion of the fat-based signal is important for diagnosis and/or tumour contouring purposes. Therefore, we have presented a method for pre-processing clinical treatment planning images which can be incorporated into a standard distortion correction procedure and which prevents the residual fat shift artifact. The technique was successfully demonstrated on a phantom containing both fat and mineral oil.

5.7. References

[1] B. Emami, A. Sethi, and G. J. Petruzzelli, "Influence of MRI on target volume delineation and IMRT planning in nasopharyngeal carcinoma," Int. J. Radiation Oncology Biol. Phys. **57,** 481-488 (2003).

[2] R. K. Ten Haken, A. F. Thronton, H. M. Sandler, M. L. LaVigne, D. J. Quint, B. A. Fraass, M. L. Kessler, and D. L. McShan, "A quantitative assessment of the addition of MRI to CT-based, 3-D treatment planning of brain tumors," Radiotherapy and Oncology **25,** 121-133 (1992).

[3] C. Rasch, I. Barillot, P. Remeijer, A. Touw, M. Van Herk, and J. V. Lebesque, "Definition of the Prostate in CT and MRI: a Multi-observer Study," Int J Radiat Oncol Biol Phys **43,** 57-66 (1999).

[4] Y. K. Lee, M. Bollet, G. Charles-Edwards, M. A. Flower, M. O. Leach, H. McNair, E. Moore, C. Rowbottom, and S. Webb, "Radiotherapy treatment planning of prostate cancer using magnetic resonance imaging alone," Radiotherapy and Oncology **66,** 203-216 (2003).

[5] T. Stanescu, H.-S. Jans, N. Pervez, P. Stavrev, and B. Fallone, "A study on the magnetic resonance imaging (MRI)-based radiation treatment planning of intracranial lesions," Physics in Medicine and Biology **53,** 3579-3593 (2008).

[6] L. Chen, R. A. Price, Jr., T. B. Nguyen, L. Wang, J. S. Li, L. Qin, M. Ding, E. Palacio, C. M. Ma, and A. Pollack, "Dosimetric evaluation of MRI-based treatment planning for prostate cancer," Phys Med Biol **49,** 5157-5170 (2004).

[7] A. Fransson, P. Andreo, and R. Potter, "Aspects of MR Image Distortions in Radiotherapy Treatment Planning," Strahlentherapie und Onkologie **177,** 59-73 (2001).

[8] V. S. Khoo, D. P. Dearnaley, D. J. Finnigan, A. Padhani, S. F. Tanner, and M. O. Leach, "Magnetic resonance imaging (MRI): considerations and applications in radiotherapy treatment planning," Radiother Oncol **42,** 1-15 (1997).

[9] L. N. Baldwin, K. Wachowicz, and B. G. Fallone, "A two-step scheme for distortion rectification of magnetic resonance images," Med Phys **36,** 3917-26 (2009).

[10] A. S. Jackson, S. A. Reinsberg, S. A. Sohaib, E. M. Charles-Edwards, S. A. Mangar, C. P. South, M. O. Leach, and D. P. Dearnaley, "Distortion-corrected T2 weighted MRI: a novel approach to prostate radiotherapy planning," Br J Radiol **80,** 926-933 (2007).

[11] C. J. G. Bakker, M. A. Moerland, R. Bhagwandien, and R. Beersma, "Analysis of Machine-Dependent and Object-Induced Geometric Distortion in 2DFT MR Imaging," Magnetic Resonance Imaging **10,** 597-608 (1992).

[12] S. J. Doran, E. M. Charles-Edwards, S. A. Reinsberg, and M. O. Leach, "A complete distortion correction for MR images: I. Gradient warp correction," Physics in Medicine and Biology **50,** 1343-1361 (2005).

[13] S. A. Reinsberg, S. J. Doran, E. M. Charles-Edwards, and M. O. Leach, "A complete distortion correction for MR images: II. Rectification of static-field inhomogeneities by similarity-based profile mapping," Physics in Medicine and Biology **50,** 2651-2661 (2005).

[14] L. Schad, S. Lott, F. Schmitt, V. Sturm, and W. J. Lorenz, "Correction of Spatial Distortion in MR Imaging: A prerequisite for accurate stereotaxy," J. Comp. Asst. Tomog. **11,** 499-505 (1987).

[15] L. Chen, T. B. Nguyen, E. Jones, Z. Chen, W. Luo, L. Wang, R. A. Price, Jr., A. Pollack, and C. M. Ma, "Magnetic resonance-based treatment planning for prostate intensity-modulated radiotherapy: creation of digitally reconstructed radiographs," Int J Radiat Oncol Biol Phys **68,** 903-911 (2007).

[16] L. Chen, R. A. Price, Jr., L. Wang, J. Li, L. Qin, S. McNeeley, C. M. Ma, G. M. Freedman, and A. Pollack, "MRI-based treatment planning for radiotherapy: dosimetric verification for prostate IMRT," Int J Radiat Oncol Biol Phys **60,** 636-647 (2004).

[17] X. M. Zhang, H. L. Zhang, D. Yu, Y. Dai, D. Bi, M. R. Prince, and C. Li, "3-T MRI of rectal carcinoma: preoperative diagnosis, staging, and planning of sphincter-sparing surgery," AJR Am J Roentgenol **190,** 1271-8 (2008).

[18] D. Halpenny, A. Snow, G. McNeill, and W. C. Torreggiani, "The radiological diagnosis and treatment of renal angiomyolipoma-current status," Clin Radiol **65,** 99-108 (2010).

[19] G. M. Israel, N. Hindman, E. Hecht, and G. Krinsky, "The use of opposed-phase chemical shift MRI in the diagnosis of renal angiomyolipomas," AJR Am J Roentgenol **184,** 1868-72 (2005).

[20] D. A. Burdenay, R. C. Semelka, N. L. Kelekis, C. Reinhold, and S. M. Ascher, "Small (<1.5 cm) Angiomyolipomas of the Kidney: Characterization by the Combined Use of In-Phase and Fat-Attenuated MR Techniques," Magn Reson Imaging **15,** 141-145 (1997).

[21] E. M. Haacke, R. W. Brown, M. R. Thompson, and R. Venkatesan, *Magnetic resonance imaging: physical principles and sequence design* (Wiley-Liss, New York, 1999).

[22] H. Chang and J. M. Fitzpatrick, "A technique for accurate magnetic resonance imaging in the presence of field inhomogeneities," IEEE Trans Med Imaging **11,** 319-329 (1992).

6. Chapter 6: An Investigation of the Dosimetric Consequences of Distortion Correction on MR-RTP

6.1. Introduction

Target localization for prostate radiotherapy treatment planning is typically carried out on CT images. However, MRI offers several advantages, including improved soft-tissue contrast between the prostate and surrounding structures and the ability to acquire images in coronal and saggittal planes for better organ visualization. Furthermore, MR scanners can be used to generate both anatomical and biological images which may further enhance the ability to contour relevant organ and biological target volumes and to develop targeted radiation therapy treatments. As radiation therapy moves towards more conformal treatment volumes, accurate tumor delineation becomes increasingly important; the superior contrast of MRI offers the potential for improved delineation of soft-tissue cancers and MR-based radiotherapy treatment planning is therefore an area of great interest.

Much work has been carried out to compare delineation of soft-tissue structures in MR and CT for prostate,[1-5] brain,[6-9] and cervical lesions.[10] With respect to prostate treatment planning, MRI allows better evaluation of pelvic organ boundaries (i.e. prostate, prostatic apex/base, seminal vesicles, rectum, bladder),[2,3]

reduced inter-observer variability in organ delineation,[1] and smaller contoured prostate volumes than in CT.[1,3,4] Better prostate visualization and more accurate contoured volumes may facilitate improved dose conformality, reduced toxicity to organs at risk, and possible improvements in patient outcomes. Although MR and CT fusion with CT-based dose calculation and MR-guided organ delineation has become routine practice,[2,11,12] the process of inter-modality registration can introduce errors. Furthermore, changes in bladder and rectal filling can alter internal anatomy making image fusion particularly problematic. Therefore, MR-based treatment planning is under investigation as an alternative to both CT-based and fused CT/MR-based treatment planning. It would remove errors associated with image fusion, reduce healthcare costs associated with redundant CT imaging, and eliminate patient exposure to CT dose.

Potential limitations of MR-based treatment planning include the absence of electron density information which is required for dose calculation, and inherent image distortions which may affect the accuracy of the dose calculation. With respect to the electron density information, image segmentation and bulk density assignment appears to be a viable solution. In 2004, Chen *et al* compared prostate plans calculated on CT images both with and without inhomogeneity corrections; they concluded that although doses calculated with homogeneity corrections were slightly lower than doses calculated without correction (due to increased bone attenuation), the differences were not clinically significant for either 3D-CRT or IMRT dose calculations in the pelvic region.[13] However, in another paper

published by the same research group in the same year in which they carried out MRI-based IMRT treatment planning, MR images were fused to CT in order to provide full inhomogeneity correction.[11] Y. K. Lee *et al* conducted a similar study comparing pelvic CRT plans with both homogeneous geometry assumptions and partial heterogeneity corrections (i.e. bone and water) to plans with full inhomogeneity correction.[14] They found that partial inhomogeneity correction was required to achieve dosimetric differences of less than 2%, the acceptable limit for radiotherapy treatment planning as stated by ICRU Report 42.[15] More recently, Kristensen *et al* performed a study of MR-based treatment planning for brain tumors and found that unit density assumptions (i.e. all water) led to dose differences at selected high dose points which differed by 1.5 ± 0.3 % on average whereas inclusion of bone segmentation led to reduced dose differences of only 0.5 ± 0.2%.[8] Bone segmentation was therefore deemed preferable.

The second limitation of MR-based treatment planning is inherent image distortion. If patient anatomy cannot be correctly defined, dose calculations will be in error. Although many studies have stated the importance of MR distortion correction for MR-based treatment planning,[5,11,12,16] to our knowledge, there has been no systematic study comparing the dosimetric differences of prostate treatment plans based on uncorrected and corrected MR images.

In their study comparing 15 MRI- and CT-based prostate IMRT plans, Chen *et al* found no significant differences in plans calculated using CT-based body contours

versus plans calculated using distortion-corrected MR-based body contours.[11] The same internal contours (defined on MR) were used for both plans and electron density information for the MR-based plan was derived from the fused CT data set. Thus, there was no evaluation of dosimetric differences before and after MR distortion correction. Based on their work, the Fox Chase Cancer Center has clinically implemented MRI-based treatment planning for prostate IMRT – but only for patients with maximum lateral dimensions ≤ 38 cm.[11] For larger patients, they continue to use MRI fusion with CT-based dose calculation due to the large residual geometric errors (up to 2.7 cm) which could not be corrected with their gradient distortion correction software.

More recent work comparing MR- and CT-based prostate treatment planning was carried out by Jackson *et al*.[5] Again, they fused CT and (distortion-corrected) MR data sets and used CT-derived electron density information for dose calculations. OARs were always defined on MR (and copied to CT for the CT-based plan), whereas the PTV was defined separately on MR and CT for each of the plans. The same field arrangements, beam weights, wedge angles, etc. were used for the paired plans; they differed only in field shape due to the differently defined PTVs. Jackson *et al* confirmed previous findings that MR-defined target volumes were smaller than CT-defined target volumes and found that the MRI delineation of the prostate resulted in a 4-6% decrease in rectal volumes receiving high doses (45 – 65 Gy).

The superiority of MR soft-tissue contrast has been well established and several studies have shown that MR-derived prostate contours differ significantly from CT-derived contours. These differences are seen primarily in the most inferior (apical) region of the prostate.[17] Prostate volumes have been shown to be 19-40% smaller when defined on MR as opposed to when defined on CT.[1-3,17-19] Smaller MR volumes may enable dose escalation through improved rectal sparing. Despite these significant advantages, inherent image distortion is often cited as a limitation to treatment planning based on MR images alone. In this study, we therefore consider the dosimetric effects of distortion correction on MR-based treatment planning for prostate patients. Image correction is based on the method outlined in Chapter 4. By comparing treatment planning endpoints calculated on both uncorrected and corrected MRI data, the importance of incorporating distortion correction schemes into MR-based prostate treatment planning can be evaluated. Provided dosimetric differences are small, the potentially labor intensive process of MR distortion correction may not be necessary and MR-based treatment planning may be streamlined in practice.

6.2. Methods

6.2.1. MRI Scanning Procedure

All patients were scanned on the Philips 3.0 T Intera MRI scanner (Philips Medical Systems, Cleveland, OH) using the body coil. Although pelvic coils can

be used for improved signal-to-noise ratio (SNR), these generally compress the patient anatomy in a way that is not mimicked during treatment sessions and the body coil was therefore used. Total duration for each patient's imaging session was between 15 and 25 minutes, which including time for briefing the patient about the protocol, obtaining informed consent, and patient set-up. Patients were to present with full bladder and empty rectum and Buscopan was injected a few minutes prior to MRI scanning in order to reduce internal bowel motion. Set-up was carried out according to the standard Cross Cancer Institute (CCI) prostate patient protocol: a custom-made flat-top table insert, a rigid knee and ankle support, a 10 cm sponge under the head, and arms crossed over the chest.

Four MRI sequences were performed – 2 B_0 mapping scans (as described in Chapter 4, §4.2.2), requiring 2 minutes 10 seconds each (2:10), as well as 2 anatomical imaging scans: a 3D BFFE (5:30), and a 3D FLASH sequence (3:40). Automatic shimming was performed prior to the acquisition of the BFFE sequence and identical shim settings were used for subsequent acquisitions. Using a 400-450 mm FOV, axial slices were obtained from the L5 vertebra to the ischial tuberosities (approximately 200 mm) to cover all structures relevant to dose volume histogram (DVH) calculations (i.e. bladder and rectum). A slice thickness of 3 mm was used for the BFFE and FLASH images, while 5 mm was used for the B_0 field mapping scans. In-plane pixel resolution varied according to the FOV, but was approximately 0.88 x 0.88 mm^2 for the BFFE image and 1.76 x 1.76 mm^2 for all other images. Read gradient strengths also varied between

patients according to the FOV selected; however, gradient strengths of 8.1 - 8.4 mT/m were used for the BFFE and FLASH sequences.

6.2.2. Structure Delineation and Treatment Planning

Uncorrected MRIs were transferred to the Varian Eclipse treatment planning system (Varian Medical Systems, Palo Alto, CA) where the body and boney structures were contoured by a physicist (LB) while the prostate and organs at risk were contoured by the oncologist (NP). Body and bone structures were also reviewed by the oncologist and modified, if necessary. The body, prostate and organs at risk were contoured based on the 3D BFFE images. Bones were surrounded by a distinct dark region in the 3D FLASH images and they were therefore used in conjunction with the BFFE images in order to contour boney structures. As a result of interpolating from original to corrected coordinate systems, the distortion-corrected image set appears slightly smoothed as compared to the original image set; for this reason, contouring and treatment planning were carried out on the uncorrected image sets. After the initial plans were generated, both images and contours were corrected using the distortion correction data.

Although CT images were available for each of the patients, they were not fused with the MR data sets due to potential errors associated with rigid image registration. CT images were used in isolation to determine the average image

intensity within the CT bone contours. This intensity, given in Hounsfield Units (HU), was then assigned to the bone contours on the MRIs so that the treatment plans could be calculated based on the bulk-electron density assigned MR data set. CT-based bone contours (pelvic bones and femurs) were obtained by thresholding and were exported to Matlab along with the corresponding CT images. The mean CT value within the bone contour was determined to be 325 ± 270 HU which compares well with the value of 320 HU reported by YK Lee *et al*.[14] Thus, a value of 325 HU was uniformly applied to the segmented bone structures while all other structures were assumed to be water-equivalent (0 HU). The CT images were therefore excluded from further use in this treatment planning study.

Based on each patient's uncorrected 3D BFFE imaging data set, both standard 3D-CRT and IMRT plans were created using separately defined PTVs: *PTV_standard* (for the 3D-CRT plan) and *PTV_IMRT* (for the IMRT plan). The *PTV_standard* was defined using a 5 mm posterior margin, and a 10 mm margin in all other directions. The treatment dose of 78 Gy was planned over 39 fractions with 95% isodose coverage to the full *PTV_standard*. Constraints published by Lawton *et al* were used for the two organs at risk: (1) the bladder was constrained to receive less than 55 Gy to 50% of its volume and less than 70 Gy to 30% of its volume; (2) the rectum was constrained to receive less than 55 Gy to 50 % of its volume and less than 70 Gy to 30 % of its volume.[20]

The *PTV_IMRT* was defined using 3 mm posterior and inferior margins and 8 mm margins elsewhere. The 78 Gy treatment dose was similarly planned over 39 fractions with full dosage to 95 % of the *PTV_IMRT*. The same Lawton constraints were used for both the bladder and rectum.

6.2.3. Distortion Correction

Gradient non-linearity maps were previously generated for the Philips 3.0T Intera system using the 3D grid phantom.[21,22] Maps of the *x-, y-,* and *z*-gradient nonlinearity distortions are available over a roughly elliptical FOV with maximal *x, y,* and *z* dimensions of 440 x 265 x 260 mm^3. Sequence-dependent spatial distortions were determined from the B_0 field distortion maps acquired for each patient during the imaging session. Two B_0 mapping scans were acquired for each patient: the first, with fat and water signals not in phase, was used to calculate sequence-dependent spatial distortions based on the relevant frequency encoding gradient strengths used for each the 3D BFFE and 3D FLASH images; the second, with fat and water signals in-phase, was used to calculate image intensity distortions. For further details regarding the distortion correction method, the reader is referred to Chapter 4, §4.4.

Patient images and contours were exported from Eclipse to a Matlab workstation. Full distortion correction maps were generated for each patient using the gradient non-linearity data as well as the not in phase B_0 mapping scan; 3D geometric

distortion correction was carried out for both the images and the contours using in-house developed software. Intensity distortions in the image data sets were corrected using the gradient non-linearity data in conjunction with the in-phase B_0 mapping scan. Once corrected, both the images and contours for each patient were transferred back to Eclipse.

6.2.4. Dose Calculation

The same plans developed on the uncorrected images using the uncorrected contours were applied to the corrected images and contours. The same beam arrangements, energies, field sizes, beam modulation, monitor units, calculation points, and calculation methods were used. Strictly speaking, there is no difference between the two treatment plans; differences are limited to dosimetric changes arising from distortion-related shifts in the location and shape of the body, target, and other structures with respect to the radiation fields. Therefore, four plans were calculated for each patient: (1) a 3D-CRT plan based on uncorrected image and contour geometry (*Standard_u*); (2) the same 3D-CRT plan based on corrected image and contour geometry (*Standard_c*); (3) an IMRT plan based on uncorrected image and contour geometry *(IMRT_u*); and (4) the same IMRT plan calculated on corrected geometry (*IMRT_c*). Once again, plans were calculated based on MR images using bulk electron density assignment (bone = 325 HU; all else = 0 HU). *Standard_u* and *Standard_c* plans were compared to evaluate the effects of distortion correction on 3D-CRT prostate

plans, while *IMRT_u* and *IMRT_c* plans were compared to evaluate the effects of distortion correction on IMRT prostate plans.

6.2.5. Distortion Evaluation and Plan Comparison

Pixel-by-pixel distortions due to both sequence-independent and sequence-dependent spatial distortions were calculated for each patient and were summarized in terms of maximum and mean patient distortions. Next, the centroids of relevant organs – prostate, bladder, and rectum – were calculated both before and after distortion correction to determine positional shifts. Given a 2D polygon bounded by a N contour points (x_i,y_i), the polygon area, A, can be calculated as[23]

$$A = \frac{1}{2}\sum_{i=0}^{N-1}(x_i y_{i+1} - x_{i+1} y_i) \qquad \text{Eq. 6-1}$$

and the centroid, (c_x, c_y) can be calculated as[23]

$$c_x = \frac{1}{6A}\sum_{i=0}^{N-1}(x_i + x_{i+1})(x_i y_{i+1} - x_{x+1} y_i)$$
$$c_y = \frac{1}{6A}\sum_{i=0}^{N-1}(y_i + y_{i+1})(x_i y_{i+1} - x_{x+1} y_i) \qquad \text{Eq. 6-2}$$

The 2D centroid was calculated for each slice and weighted by the area of the contour at that slice in order to find the 3D centroid (c_x, c_y, c_z). The positional shift was calculated as

$$\Delta x, \Delta y, \Delta z = (c_{x\,final} - c_{x\,initial}), (c_{y\,final} - c_{y\,initial}), (c_{z\,final} - c_{z\,initial}) \qquad \text{Eq. 6-3}$$

Treatment plans were compared based on changes to the clinical acceptance criteria employed in our institution. For the two 3D-CRT plans, *Standard_u* and *Standard_c*, the minimum, maximum and mean doses to the *PTV_standard* (as a percentage of the prescription dose, 78 Gy) were calculated. Similar values were calculated for the *PTV_IMRT* for the two IMRT plans, *IMRT_u*, and *IMRT_c*. Additionally, the percentage of the prescription dose delivered to the 95% target volume, V_{95}, was calculated. For the organs at risk, the D_{50} and D_{30} (bladder), and D_{50} and D_{20} (rectum) values were calculated in Gray for the 4 different plans: *Standard_u*, *Standard_c*, *IMRT_u, IMRT_c*. To compare the effects of distortion correction on both 3D-CRT and IMRT plans, differences in these dosimetric endpoints were calculated. For example, the difference in the maximum dose to the *PTV_standard* for *Standard_u* and *Standard_c* plans was calculated as

$$\Delta D_{\max} = \frac{D^1_{\max}}{D_{prescription}} \cdot 100\% - \frac{D^2_{\max}}{D_{prescription}} \cdot 100\% \qquad \text{Eq. 6-4}$$

where D^1_{max} and D^2_{max} are the maximum *PTV_standard* doses for the *Standard_u* and *Standard_c* plans, respectively, and $D_{prescription}$ = 78 Gy for all plans. Finally, the plans were qualitatively compared based on visual inspection of isodose lines and dose volume histograms (DVHs).

6.3. Results

All patients were able to complete the MRI exams. Of the 16 patients scanned under the protocol, 10 were selected for inclusion in the following analysis. The remaining 6 patients were either too large or were insufficiently positioned within the magnet's bore such that some portion of the pelvic region lay beyond the useful imaging volume of the Philips 3T Intera system; thus, full distortion correction could not be achieved. Unfortunately, due to the limited field of view of current closed bore MR systems, MRI – and hence MR-RTP – is not a viable option for patients with very large abdominal girth. Larger bore and/or open bore designs are better suited for imaging large patients. Maximum lateral dimensions of the patients in this study (i.e. for whom full distortion correction could be achieved) ranged from 35.5 cm to 42.1 cm.

Although Khoo *et al* recommend a 3D FLASH sequence for its ease of prostate delineation,[2] the radiation oncologist involved in this study preferred to work with the 3D BFFE images due to superior image resolution (0.88 x 0.88 mm^2 for the BFFE images versus 1.76 x 1.76 mm^2 for the FLASH images). Thus, all treatment plans were designed using the BFFE images and calculated distortions and other MR-based treatment planning results are presented for this sequence only.

Pixel-by-pixel image distortion was calculated for each of the patients based on the B_0 field mapping scan and the previously acquired gradient non-linearity data. Figure 6-1 shows peak-to-peak distortion, maximum absolute distortion, and mean absolute distortion for both sequence-dependent spatial distortions (B_0 / susceptibility / chemical shift) and sequence-independent spatial distortions (gradient non-linearity). For the sequence implementation employed in this study, frequency encoding was carried out in the left-right (x) direction and therefore sequence-dependent distortions are manifest in the x direction. Total distortion in the x direction is thus calculated by summing the x-gradient distortions with the sequence-dependent distortions. The total distortion in the x direction, along with the magnitude distortion (from all sources), are also shown in Figure 6-1. Patients 1 to 10 were sorted according to their maximum lateral dimension (as measured from within Eclipse), from smallest to largest; a general increase in the magnitude of all types of distortion in Figure 6-1 can be seen as the patient width increases.

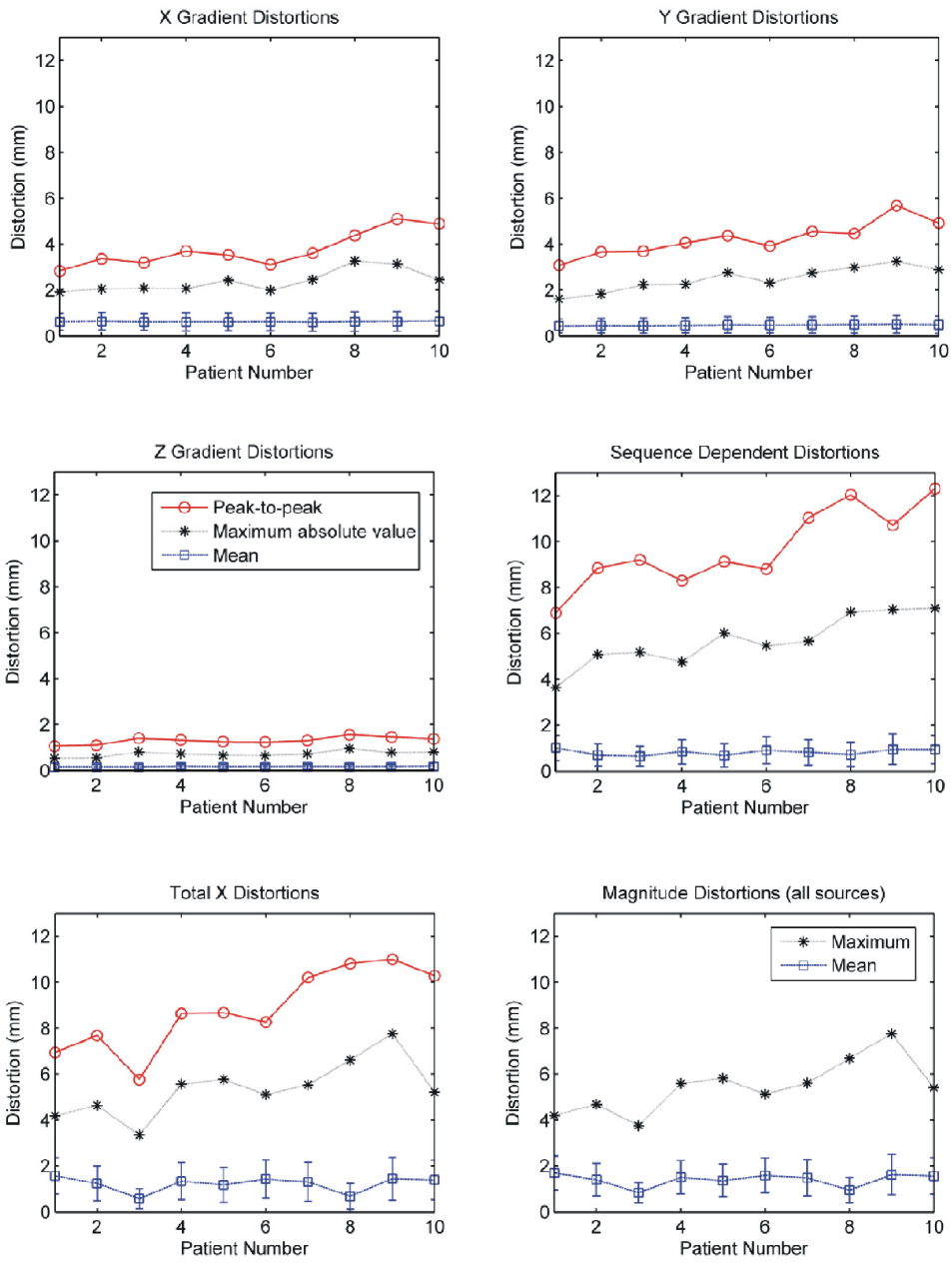

Figure 6-1

Image distortion summary. Peak-to-peak distortion, maximum absolute distortion, and mean (standard deviation) distortion is shown for 10 patients. Distortions were measured within the 3D body contour for each patient and were separated into sequence dependent distortions and gradient non-linearity (sequence-independent) distortions.

Table 6-1 shows a summary of the mean, maximum and peak-to-peak distortions for each of the distortion sources. Averaged over all patients included in the study, the maximum absolute value of sequence-independent spatial distortions was 2.4 ± 0.5 mm, 2.5 ± 0.5 mm, and 0.7 ± 0.1 mm from the *x-, y-,* and *z*-gradients respectively. Both *x*- and *y*- gradients contributed similar amounts of distortion whereas distortion in the *z* (through-plane) direction was smaller by a factor of ~3.5. The *x*- and *y*- gradient contributed similar mean distortions as well: 0.6 ± 0.4 mm and 0.5 ± 0.4 mm, respectively, while the mean distortion due to the *z*-gradient was only 0.2 ± 0.1 mm. Sequence-dependent spatial distortions were somewhat larger with a maximum and mean absolute values of 5.7 ± 1.1 mm and 1.2 ± 0.8 mm, respectively. It must be remembered, however, that sequence-dependent distortions are affected by the choice of imaging sequence. For this study, treatment planning was carried out on a 3D BFFE sequence, and distortions are therefore reflective of that sequence implementation only. By selecting a smaller or larger read gradient strength, such distortions would increase or decrease in magnitude. Furthermore, by designing the sequence such that frequency encoding is carried out in the *y*- or *z*-direction, the direction of the sequence-dependent distortions can be changed.

		Max. Absolute Distortion [mm]	Mean Distortion [mm]
Sequence-independent	x-gradient	2.4 ± 0.5	0.6 ± 0.4
	y-gradient	2.5 ± 0.5	0.5 ± 0.4
	z-gradient	0.7 ± 0.1	0.2 ±0.1
Sequence-dependent	x-direction	5.7 ± 1.1	0.8 ± 0.5
Total image distortion	Δx_{total}	5.4 ± 1.2	1.2 ± 0.8
	Δr_{total}	5.4 ± 1.2	1.4 ± 0.7

Table 6-1:

A summary of the mean and maximum absolute distortion calculated within the 3D body contour for each patient and averaged over all 10 patients included in this study.

The distortion values presented thus far reflect distortions occurring over the entire patient volume. Since distortions typically increase as the distance from isocenter increases, larger distortions are expected to occur along the body contours. However, the more clinically relevant distortions may be described by the shifts affecting both the target and organs and risk. To evaluate the effect of distortion correction on these organs, both the original and distortion-corrected structure contours were exported to Matlab and were used to calculate the organ centroids according to Eqs. 6-1 and 6-2. Finally, the centroid shifts were calculated by comparing the original and distortion-corrected centroid positions according to Eq. 6-3. These values are summarized in Table 6-2. Unsurprisingly,

the largest shifts occur in the *x*-direction where both sequence-dependent and sequence-independent distortions contribute to total organ displacement. The mean shift in prostate position due to distortion correction was 0.6 ± 0.6 mm in the *x*-direction, with a similar value of 0.5 ± 0.6 mm for both the bladder and rectum. Positional shifts in the *y*- and *z*-direction for all organs were considerably smaller at less than 0.2 mm.

Mean and Standard Deviation shifts for Various Organ Centroids [mm]				
	Δx	Δy	Δz	Δr
Prostate	0.6 ± 0.6	-0.1 ± 0.0	0.0 ± 0.0	0.7 ± 0.6
Bladder	0.5 ± 0.6	-0.2 ± 0.1	0.1 ± 0.1	0.6 ± 0.6
Rectum	0.5 ± 0.6	0.0 ± 0.1	-0.1 ± 0.2	0.6 ± 0.6

Table 6-2:

Shifts in organ centroids (mean ± standard deviation) due to distortion correction averaged over all 10 patients.

Such shifts in the organ centroids can result in changes to the target and OAR dosimetry. Figure 6-2 shows the target location and isodose contours for patient 8, for whom the largest shift in the prostate centroid was observed, (Δx, Δy, Δz) = (1.8, -0.1, 0.0) mm. The original 3D-CRT plan, *Standard_u,* was designed based on the uncorrected patient geometry as shown in Figure 6-2A; the planning constraint requiring complete target coverage by the 95% isodose contour is

achieved. However, following distortion correction, the *PTV_standard* is shifted by 1.8 mm towards patient left, and 95% isodose coverage is no longer achieved. If delivered, this treatment would not meet the original planning constraints; however, the mean positional shifts calculated (and indeed, even the maximum shift of 1.8 mm) are much less than values for inter- and intra-fraction organ motion reported in the literature. Trichter *et al* measured intra-fraction prostate potion for 16 patients (255 ultrasound measurements) and found mean prostate shifts of 0.0 ± 3.2 mm AP, 0.4 ± 4.8 mm SI, and 0.2 ± 2.8 mm RL, and maximum shifts of 8.1 mm AP, 20.4 mm SI, and 8.3 mm RL.[24] Similarly, Ten Haken *et al* investigated prostate motion as a function of bladder and rectal filling and found that the prostate centroid moved, on average, 3.5 ± 0.25 mm, with most of the motion occurring in the SI and AP directions. Evidently, the prostate positional uncertainty due to image distortion is, on average, much less than the position uncertainty due to organ motion.

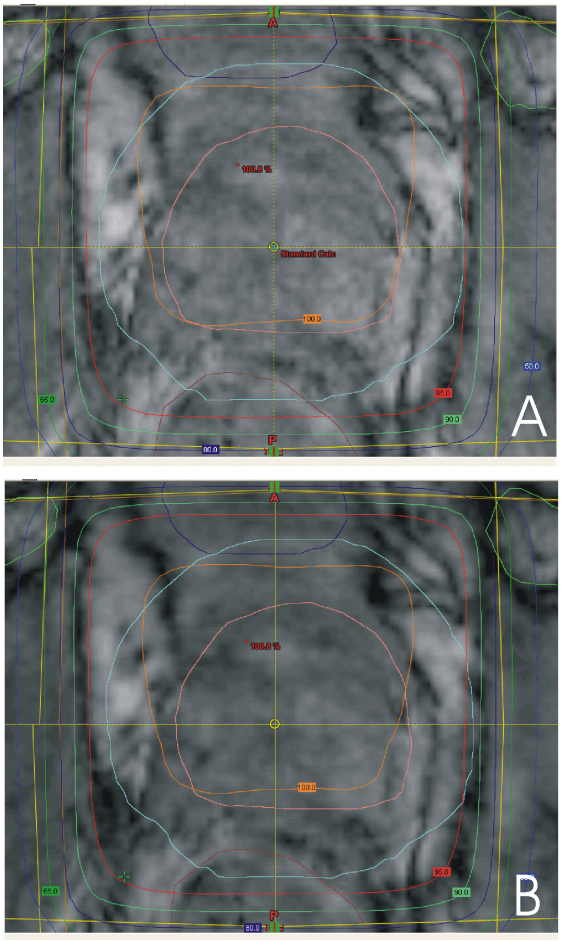

Figure 6-2

Isodose plots for plans *Standard_u* (A) and *Standard_c* (B). The *PTV_standard* is shown in light blue. Note the complete coverage of *PTV_standard* by the 95% isodose line (red) in (A), compared to incomplete coverage in (B). The shift in the prostate centroid for this patient was (Δx, Δy, Δz) = (1.8, -0.1, 0.0) mm.

To further probe the consequences of the distortion correction procedure, a variety of dosimetry endpoints were calculated for the plans based on both the original

and distortion-corrected images. Changes in the dose to the target volume were calculated according to Eq. 6-4 and are shown in Figure 6-3A. The 3D-CRT planning constraint stipulating 95% isodose coverage of the PTV was met for each patient's 3D-CRT plan calculated based on the uncorrected patient geometry (i.e. all *Standard_u* plans). However, due to distortion correction, the location of the target volume was shifted (primarily in the *x* direction) and this constraint was not met for 6/10 *Standard_c* plans. Patients 3 and 8 showed marked reduction in minimum PTV doses (-2.2% and -1.5%, respectively), while the change in minimum PTV dose averaged over all patients was (-0.6 ± 0.7)%. The change in both mean and maximum PTV % dose was (-0.1 ± 0.1)%.

With the exception of Patient 10, all stated dose constraints were met for the OARs in the *Standard_u* plans (the bladder $D_{50} \leq 70$ Gy constraint was not met for Patient 10 due to insufficient bladder filling). Following distortion correction, OAR doses for *Standard_u* and *Standard_c* were also compared; OAR dose differences ($Dose_{Standard\_c} - Dose_{Standard\_u}$) are shown in Figure 6-3B. Averaged over all patients, the dose differences at each of the constraint points were: Bladder D_{50}, (-0.1 ± 0.2) Gy; Bladder D_{30}, (-0.1 ± 0.3) Gy; Rectum D_{50}, (0.0 ± 0.1) Gy; Rectum D_{20}, (0.0 ± 0.2) Gy.

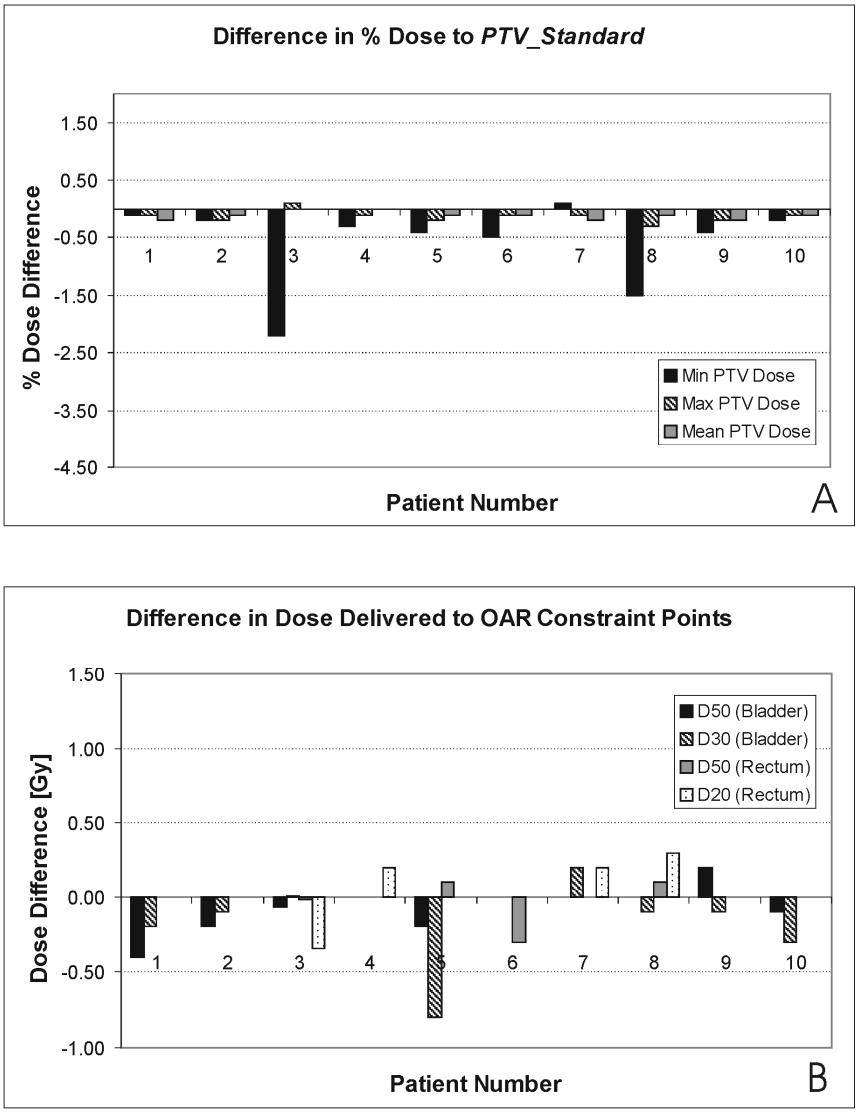

Figure 6-3

The effect of distortion correction on 3D-CRT dosimetry: a comparison of (A) the % dose delivered to the PTV, and (B) the dose delivered at the OAR constraints for the *Standard_u* and *Standard*_c treatment plans.

Figure 6-4 shows changes in dosimetric endpoints for the IMRT plans. Figure 6-4A illustrates the changes in % dose to the *PTV_IMRT*, while Figure 6-4B illustrates changes in the dose delivered to the OAR constraint points following distortion correction. The IMRT clinical acceptance criteria stipulating 95% coverage of the *PTV_IMRT* with 100% of the 78 Gy prescription dose (i.e. V_{95} = 100 %) was met for all *IMRT_u* and *IMRT_c* plans. Averaged over all patients, the *IMRT_c* V_{95} value changed by (0.0 ± 0.2)% with respect to the *IMRT_u* plans. Changes in the PTV % dose values for the IMRT plans were similar in magnitude to those seen for the 3D-CRT plans: the minimum, mean and maximum % dose values changed by (-0.3 ± 1.8)%, (0.1 ± 0.0)%, and (0.1 ± 0.1)%, respectively. Differences to the minimum PTV dose were small, with the exception of patients 3 and 8, for whom the minimum % dose changed by -4.2 % and -2.7 %, respectively, following distortion correction. Large changes in the 3D-CRT minimum PTV doses were also seen for these patients.

Concerning doses to the OAR constraint points, slightly larger differences were once again seen for the IMRT plans than for the 3D-CRT plans; these changes are illustrated in Figure 6-4B. Averaged over all patients, the dose differences at each of the constraint points for the *IMRT_u* and *IMRT_c* plans were: Bladder D_{50}, (0.4 ± 0.5) Gy; Bladder D_{30}, (0.1 ± 0.2) Gy; Rectum D_{50}, (0.0 ± 0.4) Gy; Rectum D_{20}, (0.1 ± 0.1) Gy.

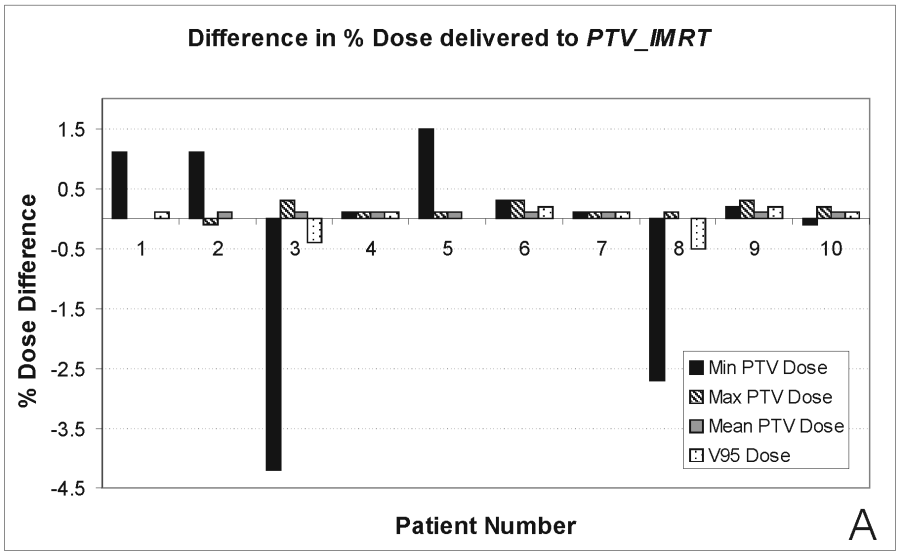

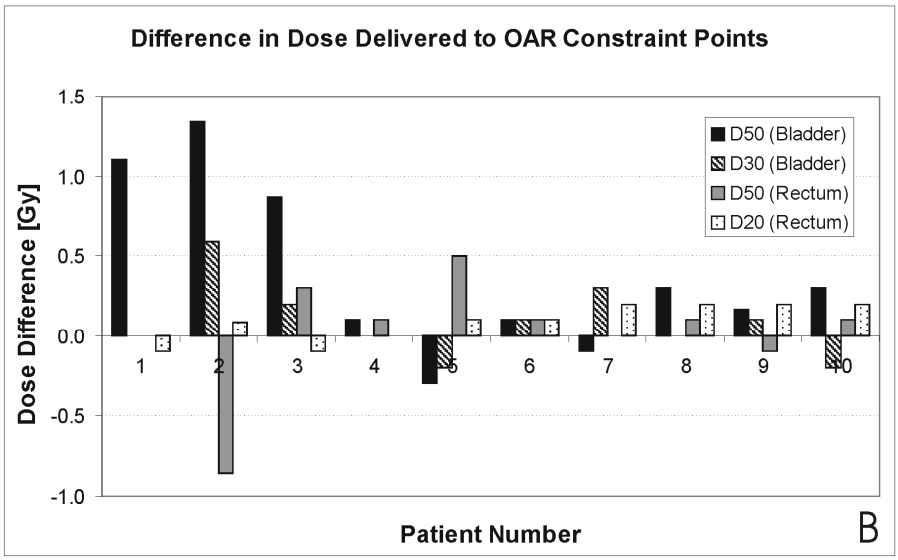

Figure 6-4

The effect of distortion correction on IMRT dosimetry: a comparison of (A) the % dose delivered to the PTV, and (B) the dose delivered at the OAR constraints for the *IMRT_u* and *IMRT*_c treatment plans.

Finally, representative dose volume histograms are shown for the two 3D-CRT

plans for patient 8, *Standard_u* and *Standard_c,* in Figure 6-5A, while Figure 6-5B shows DVH plots for the same patient for the two IMRT plans, *IMRT_u* and *IMRT_c*. Differences in DVH plots based on the uncorrected and corrected image sets are extremely minimal.

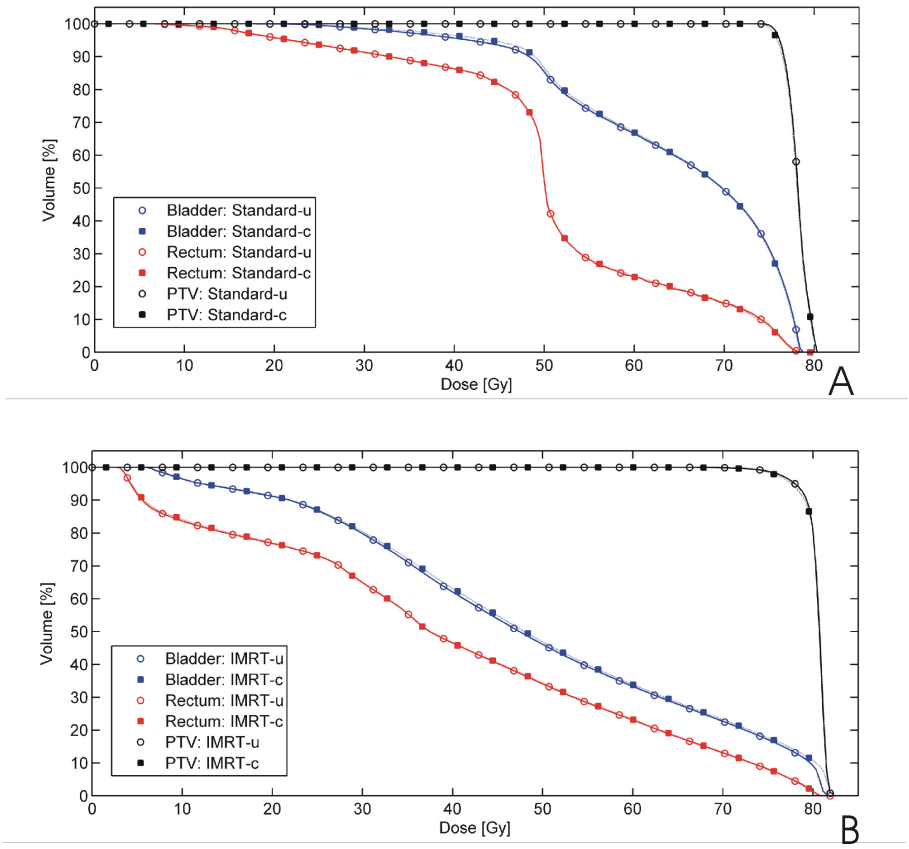

Figure 6-5

Dose Volume Histograms for (A) Standard 3D-CRT plans, *Standard_u* and *Standard_c*, and (B) IMRT plans, *IMRT_u* and *IMRT_c*.

6.4. Discussion

Figure 6-1 showed the peak-to-peak, maximum, and mean distortion for various sources of geometric distortion affecting MRIs. Patients were sorted from smallest (Patient 1) to largest (Patient 10), as determined by their maximum lateral dimension. In accordance with expectation, all types of distortion showed a general increasing trend as lateral patient dimensions increased. Distortions did not smoothly increase, however, and this may be due to the fact that the widest portion of a patient may be found at different locations. That is, the widest portion may be found in line with the prostate near the through-plane isocenter of the magnet (where distortions are smallest), or, it may be found in more superior or inferior locations (where distortions will be greater). Moreover, a smaller patient may be less well positioned with respect to the magnet's isocenter (shifted either to the left or right) and may therefore suffer greater distortions than a larger patient who is better aligned. Improvements in patient positioning could be further achieved by supplying directions for consistent patient set-up to the MR technician (i.e. alignment of patient tattoos with isocentric lasers).

Both maximum and mean *x*- and *y*-gradient non-linearity were very similar, while distortions due to *z*-gradient non-linearity were considerably smaller, in part due to the reduced FOV in that dimension. Mean distortions arising from *x*- and *y*-gradient non-linearity were similar in magnitude to the mean distortions arising

from sequence-dependent spatial distortions; however, maximal sequence-dependent spatial distortions were considerably greater than maximal gradient distortions. Total magnitude distortion from all sources averaged over all patients was 5.4 ± 1.2 mm (maximum) and 1.4 ± 0.7 mm (mean). These values are similar to the phantom-derived distortion estimates quoted by Y.K. Lee *et al* (max/average/std distortion of 3.8/1.30/1.04 mm in a transverse plane through isocenter and 6.70/0.94/1.36 mm in a transverse plane 70 mm from isocenter).[14] Compared to the phantom-derived estimates for distortions of up to 8.3 mm (220mm FOV) quoted by Wang *et al*,[25] up to 14 mm (300 mm FOV) quoted by Krempien et al,[17] and up to 16 mm over pelvic imaging volumes quoted by Tanner *et al*,[12] our distortion values are quite minimal. Image distortions are clearly dependent upon the imaging system used.

The amount of residual distortion inherent in the distortion-corrected patient images could not be measured because ground "truth" is inherently unknown. However, the phantom studies outlined in Chapter 4 showed that the distortion correction methods employed here can rectify images with up to 4.4 mm of distortion (mean original distortion = 1.8 ± 1.2 mm), resulting in maximal residual distortions of 0.6 mm (mean residual distortion = 0.2 ± 0.1 mm).[21] This is sufficiently accurate considering the distortion values shown in Table 6-1 and the approximately 0.88 x 0.88 mm^2 pixel dimensions of the BFFE sequence.

Image distortions could have a variety of effects on patient dosimetry. On the one hand, incorrect positioning of body contours would result in photon beam attenuation errors. On the other hand, incorrect placement of structure contours would result in DVH errors for structures that intersect with high dose gradient volumes. For treatment sites nearer the body surface (i.e. breast or sarcoma), body contour distortions may have the largest effect on dosimetry, while for prostate treatments where the target volume is quite distant from the body contour, beam attenuation errors are less likely to be of concern. Since incorrect placement of structure contours may be more significant for prostate RTP, shifts in the prostate, bladder and rectum centroids as a result of distortion correction were also calculated. All structures were found shifted to the left in the distortion-corrected images as compared to the original images; this is due to the polarity of the B_0 inhomogeneity combined with the polarity of read gradient strength. If the read gradient direction and/or polarity were changed, the predominant distortion direction would also change. The mean shift of $\Delta x = 0.6 \pm 0.6$ mm for the prostate would not result in incomplete inclusion of the prostate within the PTV given the PTV margins of 8 mm for the IMRT plan. However, these PTV guidelines are meant to include uncertainties in organ motion, patient set-up, etc.; they are not meant to include systematic shifts in organ location. With this in mind, provided the same BFFE imaging sequence was always used, the PTV guidelines could be altered to include a more generous margin to the left of the organ and a more scant margin to the right of the organ. If a different sequence implementation was used (i.e. if the frequency encoding gradient polarity was

reversed), the direction of these margin alterations may have to be changed. Of course, armed with distortion data, geometric image correction should be implemented to provide the best geometric accuracy and to remove the necessity for margin manipulation.

With the exception of patients 3 and 8 for whom the minimum dose to the PTV dropped by 2.2% and 1.5% in the 3D-CRT plans (Figure 6-3A) and by 4.2% and 2.7% in the IMRT plans (Figure 6-4A), changes to the minimum, mean, and maximum PTV dose were less than 0.5 %. The larger magnitude of the changes seen in the IMRT plans can be attributed to the increased conformality of the dose distribution. Although neither patient 3 nor 8 suffered from considerably greater mean or maximum distortions over the full imaging volume, both showed much larger than average shifts in the prostate centroid (1.7 mm and 1.8 mm compared to the mean Δx shift of 0.6 ± 0.6 mm). This is likely due to the fact that both patients were poorly positioned on the couch with respect to the magnet's isocenter. That is, the patient (and hence, the centrally located prostate) was shifted approximately 20 mm to the right of the magnet's isocenter, whereas all other patients were either shifted to the left or not shifted at all. This result underscores the importance of proper alignment of the patient. Slight deviations away from the homogeneous center of the magnet can result in larger image distortions and larger changes in treatment dosimetry.

Compared to minimum PTV doses, the mean and maximum PTV doses change very little as a result of distortion correction. A small shift in the PTV with respect to the beam central axis will change the dosimetry near the PTV periphery, but when averaged over the whole PTV, this change will be reduced. Moreover, since the maximum dose is likely to occur centrally, a small shift in PTV location is unlikely to move the maximum dose outside the PTV. In contrast, the minimum PTV dose is likely to occur near the PTV periphery and is therefore more sensitive to small contour changes. This is reflected in that mean and maximum PTV doses both change by (-0.1± 0.1)% in the standard plans and by (0.1± 0.0)% and (0.0± 0.2)%, respectively, for the IMRT plans whereas the minimum dose changes by (-0.6± 0.6 0.7)% (Standard) and (-0.3± 1.8)% (IMRT).

Figures 6-3B and 6-4B showed that OAR dose differences were less than 0.8 Gy for all patients. Considering that all initial plans (*Standard_u* and *IMRT_u*) met the OAR constraints (with the exception of the *Standard_u* plan for patient 8), these small changes to D_{50}, D_{30}, and D_{20} points can be considered insignificant. Indeed, there were no plans which met OAR constraints initially, but which did not meet OAR constraints following distortion correction. Thus, distortion correction did not significantly alter the dose to the organs at risk for the patients studied.

The results of this study indicate that spatial distortions in MRI are fairly minimal for the combination of the imaging system and sequence implementation used.

Accounting for the small distortion-related alterations in the position and/or volume of the body and internal organs does not greatly alter the mean and maximum doses received by the PTV for either standard 3D-CRT or IMRT treatments. Indeed, these changes are not likely to be considered clinically significant. However, two patients received lower than expected minimum PTV doses once changes in patient geometry as a result of image distortion were accounted for. The larger (and potentially clinically significant) alterations in minimum PTV dose for patients 3 and 8 were both attributed to poor set-up positioning which led to the increased distortion near the prostate. Differences in minimum target doses were larger for IMRT treatments than for 3D-CRT treatments. For properly positioned prostate patients, the target is located near the magnet's isocenter and does not appear to suffer from much distortion. Therefore, changes in target dosimetry were generally very minimal. However, treatment volumes located more peripherally, i.e. sarcomas, may show greater sensitivity to distortion correction, since distortions would be larger near the edge of the magnet bore.

As a matter of course, measures for quantifying and correcting MR-related spatial distortions must be available. If changes in target dosimetry are not deemed to adversely affect the clinical outcomes, the somewhat labor intensive process of distortion correction may not be necessary for MRI-based treatment planning. However, it must be stressed that distortions – and thus the effects on dosimetry endpoints – will vary for different systems and sequence implementations.

Regardless of whether or not distortion correction is clinically necessary, a number of complications related to implementing MR-based radiotherapy treatment planning remain. For some of the patients imaged in this study, the body contour was difficult to define on the most superior slices due to image artifacts caused by breathing motion. Incorrect definition of the body contour could have implications on the accuracy of dose calculations in the most superior, artifact-ridden slices; avoidance of this problem requires respiratory gating which is time-consuming, but effective. A further issue regarding contouring is the amount of time it requires. Bones can be automatically contoured through image thresholding on CT images; however, this is not a viable method in MR and bones must be manually contoured if they are to be segmented and assigned a bulk electron density. Bone contouring was the most time-intensive aspect of the treatment planning process in this study and it therefore represents an increase in the work load over CT- and CT/MR-based treatment planning. Automatic segmentation of the prostate and surrounding organs has been investigated by a number of groups.[26-28] Although none of these studies have looked at automatic segmentation of bone structures in MR images, Pasquier *et al* report successful use of a seeded region growing technique for high contrast structures including bladder and rectum.[27] Similar methods may be suitable for applications involving MR bone delineation and could ease the contouring burden considerably.

6.5. Conclusions

MR treatment planning images were collected for 10 patients and images were corrected for both machine- and patient-related distortions. Total image distortion was quantified in terms of mean and maximum absolute distortion over patient volumes and the effect of distortion correction on the target and OARs was evaluated by calculating the shift in organ centroids. 3D-CRT and IMRT treatment plans were developed for both distorted and corrected patient geometry; MRIs were assigned bone and water bulk electron densities and plans were calculated based on MRIs only. Finally, the dosimetric effects of distortion correction were evaluated by comparing minimum, maximum and mean target doses as well as doses to the OARs. To our knowledge, this represents the first investigation of the dosimetric effects of full distortion correction for prostate MR-RTP. Mean and maximum target doses were not significantly altered as a result of distortion correction; differences in minimum target doses were also small, with the exception of two patients for whom minimum target doses dropped by as much as 4.7%. The clinical significance of the reduction in minimum target dose for these patients remains uncertain. Distortion correction did not result in any clinically significant changes in the doses delivered to the OARs (bladder and rectum), and DVHs for plans based on distorted and corrected patient geometry did not show marked differences. Provided patients are optimally positioned within a magnet with good homogeneity and gradient

linearity, the results suggest that distortion correction may not be required for prostate MR-RTP.

6.6. References

[1] M. Debois, R. Oyen, F. Maes, G. Verswijvel, G. Gatti, H. Bosmans, M. Feron, E. Bellon, G. Kutcher, H. Van Poppel, and L. Vanuytsel, "The contribution of magnetic resonance imaging to the three-dimensional treatment planning of localized prostate cancer," Int J Radiat Oncol Biol Phys **45,** 857-865 (1999).

[2] V. S. Khoo, A. R. Padhani, S. F. Tanner, D. J. Finnigan, M. O. Leach, and D. P. Dearnaley, "Comparison of MRI with CT for the radiotherapy planning of prostate cancer: a feasibility study," Br J Radiol **72,** 590-7 (1999).

[3] M. Roach, 3rd, P. Faillace-Akazawa, C. Malfatti, J. Holland, and H. Hricak, "Prostate volumes defined by magnetic resonance imaging and computerized tomographic scans for three-dimensional conformal radiotherapy," Int J Radiat Oncol Biol Phys **35,** 1011-8 (1996).

[4] G. M. Villeirs, K. Van Vaerenbergh, L. Vakaet, S. Bral, F. Claus, W. J. De Neve, K. L. Verstraete, and G. O. De Meerleer, "Interobserver delineation variation using CT versus combined CT + MRI in intensity-modulated radiotherapy for prostate cancer," Strahlenther Onkol **181,** 424-30 (2005).

[5] A. S. Jackson, S. A. Reinsberg, S. A. Sohaib, E. M. Charles-Edwards, S. A. Mangar, C. P. South, M. O. Leach, and D. P. Dearnaley, "Distortion-corrected T2 weighted MRI: a novel approach to prostate radiotherapy planning," Br J Radiol **80,** 926-933 (2007).

[6] B. Emami, A. Sethi, and G. J. Petruzzelli, "Influence of MRI on target volume delineation and IMRT planning in nasopharyngeal carcinoma," Int. J. Radiation Oncology Biol. Phys. **57,** 481-488 (2003).

[7] R. K. Ten Haken, A. F. Thronton, H. M. Sandler, M. L. LaVigne, D. J. Quint, B. A. Fraass, M. L. Kessler, and D. L. McShan, "A quantitative assessment of the addition of MRI to CT-based, 3-D treatment planning of brain tumors," Radiotherapy and Oncology **25,** 121-133 (1992).

[8] B. H. Kristensen, F. J. Laursen, V. Logager, P. F. Geertsen, and A. Krarup-Hansen, "Dosimetric and geometric evaluation of an open low-field magnetic resonance simulator for radiotherapy treatment planning of brain tumours," Radiother Oncol **87,** 100-109 (2008).

[9] A. F. Thornton, Jr., H. M. Sandler, R. K. Ten Haken, D. L. McShan, B. A. Fraass, M. L. La Vigne, and B. R. Yanke, "The clinical utility of magnetic

resonance imaging in 3-dimensional treatment planning of brain neoplasms," Int J Radiat Oncol Biol Phys **24,** 767-75 (1992).

[10] L. Thomas, B. Chacon, M. Kind, O. Lasbareilles, P. Muyldermans, A. Chemin, A. Le Treut, J. Pigneux, and G. Kantor, "Magnetic Resonance Imaging in the Treatment Planning of Radiation Therapy in Carcinoma of the Cervix Treated with the Four-field Pelvic Technique," Int J Radiat Oncol Biol Phys **37,** 827-832 (1997).

[11] L. Chen, R. A. Price, Jr., L. Wang, J. Li, L. Qin, S. McNeeley, C. M. Ma, G. M. Freedman, and A. Pollack, "MRI-based treatment planning for radiotherapy: dosimetric verification for prostate IMRT," Int J Radiat Oncol Biol Phys **60,** 636-647 (2004).

[12] S. F. Tanner, D. J. Finnigan, V. S. Khoos, P. Mayles, D. P. Dearnaley, and M. O. Leach, "Radiotherapy planning of the pelvis using distortion corrected MR images: the removal of system distortions," Phys. Med. Biol **45,** 2117-2132 (2000).

[13] L. Chen, R. A. Price, Jr., T. B. Nguyen, L. Wang, J. S. Li, L. Qin, M. Ding, E. Palacio, C. M. Ma, and A. Pollack, "Dosimetric evaluation of MRI-based treatment planning for prostate cancer," Phys Med Biol **49,** 5157-5170 (2004).

[14] Y. K. Lee, M. Bollet, G. Charles-Edwards, M. A. Flower, M. O. Leach, H. McNair, E. Moore, C. Rowbottom, and S. Webb, "Radiotherapy treatment planning of prostate cancer using magnetic resonance imaging alone," Radiotherapy and Oncology **66,** 203-216 (2003).

[15] ICRU, "ICRU Report 42: Use of computers in external beam radiotherpy procedures with high-energy photons and electrons," (1987).

[16] A. Fransson, P. Andreo, and R. Potter, "Aspects of MR Image Distortions in Radiotherapy Treatment Planning," Strahlentherapie und Onkologie **177,** 59-73 (2001).

[17] R. C. Krempien, K. Schubert, D. Zierhut, M. C. Steckner, M. Treiber, W. Harms, U. Mende, D. Latz, M. Wannenmacher, and F. Wenz, "Open low-field magnetic resonance imaging in radiation therapy treatment planning," Int J Radiat Oncol Biol Phys **53,** 1350-1360 (2002).

[18] K. Kagawa, W. R. Lee, T. E. Schultheiss, M. A. Hunt, A. H. Shaer, and G. E. Hanks, "Initial clinical assessment of CT-MRI image fusion software in localization of the prostate for 3D conformal radiation therapy," Int J Radiat Oncol Biol Phys **38,** 319-25 (1997).

[19] C. Rasch, I. Barillot, P. Remeijer, A. Touw, M. Van Herk, and J. V. Lebesque, "Definition of the Prostate in CT and MRI: a Multi-observer Study," Int J Radiat Oncol Biol Phys **43,** 57-66 (1999).

[20] C. A. Lawton, J. Michalski, I. El-Naqa, M. K. Buyyounouski, W. R. Lee, C. Menard, E. O'Meara, S. A. Rosenthal, M. Ritter, and M. Seider, "RTOG GU Radiation oncology specialists reach consensus on pelvic lymph node volumes for high-risk prostate cancer," Int J Radiat Oncol Biol Phys **74,** 383-7 (2009).

[21] L. N. Baldwin, K. Wachowicz, and B. G. Fallone, "A two-step scheme for distortion rectification of magnetic resonance images," Med Phys **36,** 3917-26 (2009).

[22] L. N. Baldwin, K. Wachowicz, S. D. Thomas, R. Rivest, and B. G. Fallone, "Characterization, predication, and correction of geometric distortion in 3T MR images," Med Phys **34,** 388-399 (2007).

[23] M. J. De Smith, M. F. Goodchild, and P. A. Longley, *Geospatial analysis: a comprehensive guide to principles, techniques, and software tools* (Troubador, Leicester, UK, 2007).

[24] F. Trichter and R. E. Ennis, "Prostate localization using transabdominal ultrasound imaging " Int J Radiat Oncol Biol Phys **56,** 1225-1233 (2003).

[25] D. Wang and D. M. Doddrell, "A proposed scheme for comprehensive characterization of the measured geometric distortion in magnetic resonance imaging using a three-dimensional phantom," Medical Physics **31,** 2212-2218 (2004).

[26] M. Mazonakis, J. Damilakis, H. Varveris, P. Prassopoulos, and N. Gourtsoyiannis, "Image segmentation in treatment planning for prostate cancer using the region growing technique," Br J Radiol **74,** 243-8 (2001).

[27] D. Pasquier, T. Lacornerie, M. Vermandel, J. Rousseau, E. Lartigau, and N. Betrouni, "Automatic segmentation of pelvic structures from magnetic resonance images for prostate cancer radiotherapy," Int J Radiat Oncol Biol Phys **68,** 592-600 (2007).

[28] V. Pekar, T. R. McNutt, and M. R. Kaus, "Automated model-based organ delineation for radiotherapy planning in prostatic region," Int J Radiat Oncol Biol Phys **60,** 973-80 (2004).

7. Chapter 7: Conclusions

This thesis addressed image distortions in MRI, one of the main issues preventing MR-based radiotherapy treatment planning from being incorporated into mainstream clinical practice. Namely, the following concerns were covered: 1) measurement of system-related distortions, 2) measurement of patient-related distortions, 3) methods to correct both types of distortion in a variety of clinical images, 4) implementation of MR-RT using distortion rectified images, and 5) evaluation of the clinical benefits of distortion correction for prostate MR-RTP.

In order to provide context for MR-RTP, Chapter 1 reviewed various issues concerning the use of medical images in radiotherapy. Chapter 2 followed with background on the fundamental principles of both NMR and MRI. The initial research efforts were included in Chapter 3 where the development of the materials and methods required to perform a basic assessment of image distortions generated by an MR scanner were described. Distortions were measured by analyzing images of a large, oil-filled 3D grid phantom, which was designed and built in-house. These efforts were undertaken in an effort to evaluate the suitability of the imaging system for MR-based radiotherapy treatment planning applications; therefore, it was important to not only evaluate image distortion, but also develop methods that could be applied to correct images of arbitrary objects (i.e. patients) as well. Machine-related sources of image distortion were separated from phantom-related sources of distortions through the use of both the reverse gradient method and simulation of the phantom's susceptibility distortion field. Measurements of

the machine-related distortions can be used to correct images of any object. The reproducibility of the results was tested and distortion measurements were found to be stable over several months. The maximum magnitude of machine-related distortions over the entire 266 x 266 x 205 mm^3 phantom volume was found to be 6.4 mm, with mean and standard deviation values of 1.3 mm and 0.5 mm, respectively. This was the first study to comprehensively analyse image distortions at 3 T; image distortions arising from the Philips 3T Intera system were found to be considerably less than those from other, lower field systems reported on in the literature. Mean distortions in a single 2D transverse image slice located 94 mm from isocenter were reduced from 2.53 ± 0.94 mm to 0.28 ± 0.15 mm following distortion correction; this was calculated by measuring the distorted and corrected positions of the phantom grid points relative to the true positions. Finally, a preliminary distortion prediction scheme was tested; the phantom was imaged using different sequence parameters and the distorted image was corrected based on the predicted distorted locations of the grid points. Using this method, the corrected image showed a similar mean residual distortion value of 0.29 ± 0.22 mm.

Unfortunately, phantom-derived corrections cannot adequately compensate for image distortions in-vivo. Thus, once the basic methods and materials for measuring and correcting image distortion were in place, the methodology grew to incorporate assessment of object- or patient-related distortions. This was covered in Chapter 4. Although the reverse gradient method used to measure machine-related distortions on the phantom can be adapted for in-vivo (i.e. patient-related) distortion correction, this method is time-consuming and ultimately limited in the amount and type of distortions it can

correct. As an alternative, a phase mapping scheme was implemented and was used to measure the field distortions generated by the imaged object. Furthermore, the 3D grid phantom was retro-fitted to allow measurement of the gradient non-linearity distortions over a full imaging volume of the scanner. Maximum system-related distortions were much larger when measured over the increased field of view. Peak-to-peak distortions due to *x, y,* and *z* gradient non-linearities over this volume (440 x 266 x 87 mm^3) were 10.6, 9.8 and 3.1 mm respectively, while B_0 inhomogeneities were approximately 20 ppm near the bore's edge. Measurement and correction of object-related distortions was validated on phantoms and a more comprehensive distortion prediction and correction scheme (i.e. accounting for machine- and object-related distortions) was validated on a separate cylindrical grid phantom using a variety of imaging sequences. For a moderately distorted gradient echo image, maximum and mean distortion were reduced from 4.4 mm and 1.8 ± 1.2 mm to 0.6 mm and 0.2 ± 0.1 mm. For a more severely distorted EPI image, maximum and mean distortion were reduced from 23.7 mm and 9.9 ± 6.3 mm to 3.4 mm and 1.2 ± 0.7 mm. In all cases, mean residual distortions were less than the pixel dimensions. Finally, the technique was applied to correct in-vivo pelvic images for both machine- and patient-related distortions.

The methods of Chapter 4 were used to correct images for all types of distortion – gradient non-linearity, B_0 inhomogeneities, susceptibility and chemical shift effects. However, a residual artifact related to chemical shift was sometimes observed and a potential solution to this problem was investigated in Chapter 5. The method involved pre-processing the original image before applying the distortion correction scheme

outlined above; success was qualitatively demonstrated on phantom images. In its current state, however, the method is limited in terms of in-vivo applicability due to patient motion which prevents accurate image pre-processing.

Chapter 6 covered a clinical protocol in which the methods of Chapter 4 were applied for MR-based prostate RTP. This was the first known study to compare the dosimetric consequences of distortion correction. Images of larger patients typically suffered slightly larger distortion; maximum and mean distortion averaged over all patients were 5. 4 ± 1.2 mm and 1.4 ± 0.7 mm. Mean distortions due to sequence independent sources (gradient non-linearity) were comparable to those due to sequence-dependent sources. These distortions were corrected for using the methods of Chapter 4 and both 3D-CRT and IMRT treatment plans were developed based on the contours derived from the MR data sets. The effect of distortion on the prostate target (positioned as closely as possible to the magnet's isocenter) was considerably less than the effect of distortions near the body contours: following distortion correction, the prostate centroid underwent an average shift of 0.7 ± 0.6 mm. Changes in target and OAR dosimetry were insignificant in most cases, with the notable exception of two patients for whom the minimum PTV doses dropped by 2.2% and 1.5% (3D-CRT plans) and 4.2% and 2.7 % (IMRT plans). This was due to poor patient positioning, which resulted in larger than average distortions affecting the target region. Provided patients were well-positioned, distortion correction did not appear to have a large impact on dosimetry for MR-RTP in the prostate region. Dose differences between plans prepared on uncorrected and corrected MR images in other, more peripheral regions (i.e. sarcomas) are expected to be larger.

Future projects related to the work presented in this thesis include: (1) in-vivo implementation of the residual fat-shift artifact correction. This may involve studying anatomical regions which are not subject to internal motion and which can be effectively immobilized during imaging and/or integration of the phase difference mapping and treatment planning image acquisitions. (2) Auto-segmentation of MR structures – especially bone – for ease of integration with bulk electron density assignment and dose calculation purposes. (3) Determination of the level of image distortion below which dosimetric differences in treatment planning do not warrant the extra effort of distortion correction. Our prostate MR-RTP study showed that distortion correction was unnecessary for most patients since target and OAR dosimetry on uncorrected and corrected plans differed very minimally; however, other systems and/or anatomic regions may generate larger distortions where dose differences would be greater.

Upon the implementation of the CCI MR-Linac system, there will be additional projects required to incorporate MR-RTP into the radiotherapy process. It will be important to implement MR-based verification procedures whereby the treatment planning MR images (i.e. acquired using a particular imaging sequence at 3T) would be compared against and registered with verification images (i.e. acquired using an alternate sequence at 0.2T) performed before each treatment fraction. This would require evaluation of local image intensities and determination of relevant reference structures that could be used to re-align the patient in the treatment reference frame. Finally, real-time tumour tracking may be incorporated to allow not only image guidance for inter-fraction motion, but also

adaptive measures to compensate for intra-fraction motion. Imaging at all of these stages will be subject to distortions of lesser or greater degree; thus, comprehensive knowledge regarding distortion measurement and correction will continue to be required in order to combine the powerful soft-tissue information that MRI can provide with the geometric accuracy demanded by modern, image-guided adaptive radiation therapy programs.